PATTERNED THIN-FILM TRIBOELECTRIC GENERATOR FOR HARVESTING MICRO-MESO SCALE AMBIENT ENERGY FOR KINEMATIC SENSING

A Dissertation
Presented to
the Academic Faculty

by

Qingshen Jing

In Partial Fulfillment
of the Requirements for the Joint Degree
Doctor of Philosophy in

School of Materials Science and Engineering
(Georgia Institute of Technology)
&
Department of Materials Science and Engineering
College of Engineering
(Peking University)

Georgia Institute of Technology & Peking University

August, 2015

PATTERNED THIN-FILM TRIBOELECTRIC GENERATOR FOR HARVESTING MICRO-MESO SCALE AMBIENT ENERGY FOR KINEMATIC SENSING

Approved by:

Dr. Zhong Lin Wang, Co-Advisor
School of Materials Science and Engineering
Georgia Institute of Technology

Dr. Ching-Ping Wong
School of Materials Science and Engineering
Georgia Institute of Technology

Dr. Meilin Liu
School of Materials Science and Engineering
Georgia Institute of Technology

Dr. Pingchou Han, Co-Advisor
Department of Materials Science and Engineering, College of Engineering
Peking University

Dr. Ruqiang Zou
Department of Materials Science and Engineering, College of Engineering
Peking University

Dr. Anyuan Cao
Department of Materials Science and Engineering, College of Engineering
Peking University

Dr. Shulin Bai
Department of Materials Science and Engineering, College of Engineering
Peking University

Date Approved: June 15th, 2015

To my beloved family and friends

ACKNOWLEDGEMENTS

This PhD thesis is accomplished under the great help, guidance, support and care from a lot of people who are extremely important and precious in my life. I would like to extend my most sincere gratitude to and share my accomplishment with all of them.

Being favored to conduct my PhD study in Joint PhD Program held by Peking University and Georgia Institute of Technology, I sincerely denote the deepest thanks to my two PhD advisors — Prof. Pingchou Han and Prof. Zhong Lin Wang, under whose superb guidance I was able to receive PhD training with first-class quality. Not only was my academic capability shaped by learning from their outstanding research perspectives, skills and determinations, but my attitude toward career and life is strongly affected by their great personalities. As their student, I received significant support and care from them, helping me out from frustrations and obstructions in both academic life and personal life.

Moreover, I would like to present my thanks to all the professors in my thesis committee. It is my great honor to have these prestigious professors to evaluate my efforts and achievements as a PhD student. They have shared a lot of their precious time to provide suggestions to my research.

During years of my PhD study, I received support from a tremendous amount of people. They were my lab-mates in research, friends in life. I deliver my thanks to Dr. Senbin Ye, Dr. Guang Zhu, who provided and guided me with plenty of research skills. Thanks to mates in my research groups, they are, Zhewen Tang, Prof. Ying Wu, Dr. Caofeng Pan, Dr. Youfan Hu, Dr. Yong Ding, Dr. Wenzhuo Wu, Mr. Tiejun Zhang, Dr. Chen Xu, Dr. Sihong Wang, Dr. Ya Yang, Dr. Yannan Xie, Peng Bai, Dr. Ying Liu, Dr.

Yusheng Zhou, Xiaonan Wen, Long Lin, Ruomeng Yu, Simiao Niu, Jun Chen, Dr. Zonghong Lin, Dr. Fang Zhang, Fang Yi, Dr. Hulin Zhang, Dr. Yuanjie Su. Prof. Xiaohong Yang, Prog. Jin Yang, Prof. Weiqing Yang, Anqi Chen, Yukun Sun, Ms. Zhengnian Zhou, etc. Thanks to my friends for their accompanying, Dr. Ce Yang, Dr. Lining Ju, Yupeng Zheng, etc.

More importantly, I would like to express my deepest love and thank to my parents. I am who I am because of their continuous education and guidance. They have unconditionally supported my choice in study and life both financially and mentally. They are my strongest back up in my life that I have to value all the time.

Here I would like to provide special thanks to my beloved girlfriend, Zhen Wei. We met in Georgia Tech, where we started our blessed story filled with sweetness and happiness. It is also in this period of time that I achieved my best research productivity, which was largely benefited from her accompanying and inspiration.

Last but not least, I would like give my acknowledgement to all the people that have contributed to Joint PhD Program, these people are mainly from College of Engineering (Peking University), Office of International Relations (Peking University) and Department of Material Science and Technology (Georgia Institute of Technology), as well as China Scholarship Council. They are, Ms. Teresa Nelson, Ms. Susan Bowman, Prof. David Bucknall, Prof. Naresh Thadhani, Ms. Lixia Men, and Mr. Feng He, etc.

Table of Contents

List of Tables

List of Figures

LIST OF ABBREVIATIONS

M^2SAE	Micro-meso scale ambient energy
SMD	Small mobile device
TEG	Triboelectric generator
TENG	Triboelectric nanogenerator
cTENG	Case-encapsulated triboelectric nanogenerator
vsTEG	Velocity-sensing triboelectric generator
dsTENG	Direction-sensing triboelectric nanogenerator
QS-TES	Quasi-static triboelectric sensor
1-D	One dimensional
2-D	Two dimensional
3-D	Three dimensional
SEM	Scanning Electron Microscope
PTFE	Polytetrafluoroethylene
PDMS	Polydimethylsiloxane
PET	Polyethylene terephthalate
FEM	Finite element method
FEP	Fluorinated ethylene propylene

PVD	Physical vapor deposition
MCU	Microcontroller unit
TTL	Transistor-transistor logic
LED	Light emitting diode
AC	Alternating current
IE	Inner electrode
OE	Outer electrode
TE	Top electrode
BE	Bottom electrode
BC	Base channel
RC	References channel

SUMMARY

Harnessing random micro-meso scale ambient energy (M^2SAE), which is widely available in human motions, wind driven vibrations, water surface fluctuations, etc., is not only clean and sustainable, but it also enables self-powered sensors and devices to be realized. In my research, I have fabricated a case-encapsulated triboelectric generator (cTENG) based on the principles of sliding electrification for harvesting M^2SAE from reciprocating motions. Patterned with multiple sets of grating electrodes and lubricated with polytetrafluoroethylene (PTFE) nanoparticles, cTENG generated an average effective output power of 12.2 mW over a 140 kΩ external load and a power density of 1.36 W/m^2 at a sliding speed of 1 m/s. The cTENG can also be triggered by direct-applied forces, as well as, inertia forces to effectively capture ambient energy from vibrations of large amplitudes and low frequencies such as those arising in human motions and water surface fluctuations.

Based on the success of the patterned cTENG, I have built a self-powered velocity sensor for either rectified linear or rotary motion by sourcing the energy from the triboelectric generator. Employing alternating Kapton-copper strips arranged in a spiral configuration wrapped on the inner and outer surfaces of two concentric cylinders, voltage assays for linear and rotary motions can be measured without the need for an external power source. The triboelectric generated output signals when integrated with a digital circuit and a microcontroller unit can be directly processed into remarkably stable, macro-scale output signals for measurements of (0.1–0.6) $ms^{-1} \pm 0.5\%$ for linear velocities and (300–700) rpm ± 0.9% for rotary velocities.

I have also fabricated a self-powered, thin-film motion direction sensor by harvesting the operational energy from a close-proximity triboelectrification of two surfaces in relative reciprocation. The mover made by coating a thin polytetrafluoroethylene film with a 2-column, specially arranged array of copper electrodes and the stator is made by coating the top and bottom surfaces of a thin polyimide film with a 2-column aligned array of copper electrodes placed in an alternating pattern. As the mover traverses over the stator, the electrodes in the mover actively generate electric signals of ±5 V to attain a peak power density of ≥ 65 mW/m^2 at speeds of 0.3 ms^{-1}. The prototype can be extend for 2-D motion direction sensing. The highly pliable sensor can be easily bent to spread over curved and uneven surfaces.

Finally, I have demonstrated a quasi-static angular positioning sensor based on 4-channel encoded pattern on the electrification surface. The sensor consists of a rotator designed with 4-channel coding Cu foil material and a stator including electrodes covered with FEP (fluorinated ethylene propylene) film. Due to coupling effect of triboelectrification and electrostatic induction, the sensor generates electric output signals in response to mechanical rotating motion of an object mounted with the sensor. The sensor can read and remember the absolute angular position regardless being continuously monitored or segmented monitored. Velocity and acceleration can be calculated as well. Under a rotation speed of 100 rad min^{-1}, the output voltage of the sensor reaches as high as 60 V. Angular resolution of 22.5° is achieved and can be further improved by increasing the number of channels. Triggered by the output voltage signal, the rotating characteristics of the steering wheel can be real-time monitored and mapped by being mounted to the sensor.

My work represents the first successful attempt in harvesting M^2SAE using a patterned triboelectric generator and then, using the harvested ambient energy to drive a

kinematic sensor that is integrated with a commercial digital circuit for a dual-mode speed and direction sensing. I believe my pioneering demonstration of the applied triboelectric technology will have a huge impact in the industrial commercialization of self-powered devices and sensors.

TITLE AND SUMMARY (CHINESE)

基于纹饰薄膜摩擦发电机的微介尺度环境能量转化研究及运动传感器设计

利用摩擦发电机收集环境中的微介尺度随机能量（micro-meso scale ambient enegy， M^2SAE， 例如人体运动，风引起的振动，水面波动等等）并用于发电不仅环保和可持续，而且为自驱动传感器和设备的实现提供了方案。在我的研究中，我设计制造了一种基于滑动摩擦起电的高度整合的栅格式套筒摩擦纳米发电机，用来收集环境能量中存在的往复运动的机械能并转化为电能。该设计由若干平行排列的栅格电极组成栅格状摩擦面，并施以聚四氟乙烯（polytetrafluoroethylene）纳米颗粒与摩擦面以提高转化能力。在外部电路电阻为 140 kΩ，滑动速率为 1 m/s 时发电机的平均输出可达到 12.2 mW，表面发电密度可以达到 1.36 W/m^2。 发电机可以被环境中存在的往复运动直接驱动而发电，也可以使用自身的惯性收集振动能量，包括各种振幅或低频率难以利用的振动能量。这种发电机在针对微介尺度随机运动机械能的应用中，如收集人体的运动能量和转化水面起伏产生的机械能中的表现均得到了实验的验证。

在栅格式套筒摩擦纳米发电机的成功设计基础上，我进一步设计了基于摩擦发电机工作原理的自驱动线性/转动速度传感器。系统由圆柱体和外套筒组成，圆柱体外壁和外套筒内壁均由 Kapton 薄膜和沉积在薄膜两侧的螺旋栅格排列的铜电极组成，通过相对运动的摩擦可直接将运动的机械能转化为速度相关的电信号，而不需要外部供电。这一信号与普通商用电子电路连接，可被微处理器识别并计算出稳定的运动速度，实验测量范围和误差可达 0.1-0.6 ms-1 ± 0.5% （直线运动）和 300-700 rpm ± 0.9% （转动运动）。

进一步，我设计了薄膜自驱动运动矢量传感器。传感器工作原理基于两种材料接触并相对滑动产生的摩擦起电原理，通过在动子上制作有错位的双栏栅格式金属条纹摩擦面、在定子上制作双栏栅格式电极，进而测量双栏输出信号的差异判断运动方向。这一自驱动传感器的输出信号在滑动速度为 0.3 ms^{-1} 时可以达到±5 V，相应的最大输出功率密度可达到 65 mW/m^2。这一模型可扩展并测量二维（平面）运动矢量。柔性材料作为基底让传感器可以适应一部分曲面，并应用在非平面的场合。

此外，通过在摩擦面上进行四通道编码图案设计，我们还设计了准静态角度位置传感器。这是一个由转子和定子组成的结构，转子表面镀有薄片金属铜编码图案，构成四通道。定子则由被氟化乙烯丙烯共聚物（FEP）薄膜覆盖的扇形感应输出电极组成。由于摩擦起电和静电感应的耦合作用，电极输出信号与驱动该传感器的转动位置相关。无论信号是否被持续监测，摩擦编码角度传感器都可以测量记录转动运动的绝对角度。在此基础上传感器亦可以计算角速度和角加速度。在转速 100 rad min^{-1} 的情况下，电极相对于地（零势面）可达到 60 V 的输出。四通道编码角度传感器的角度分辨率为 22.5°，可以进一步提高通道数量以提高分辨率。这一传感器被证明可以与方向盘相连，受传感器输出信号的触发，实时的监控方向盘的角度并显示在电脑中进行后处理。

我的工作巧妙地将表面结构图案引入摩擦发电机制造运动传感器并创造性地将摩擦传感器与商用数字电路相结合，制作出了利用微介尺度环境能量的发电机和自驱动速度，运动矢量和准静态角度传感器。我相信这些设计会对自驱动设备和传感器的工业化产生巨大的影响。

CHAPTER 1

INTRODUCTION

The rapidly developing trend in new electronic devices encompasses some if not most of the following attributes: mobility, wearability, connectivity, wireless enability, transformability, long-duration usability, unattended usability and energy sustainability.[1-4] These products are becoming increasingly pervasive in our everyday life in devices such as smartphones, tablets, wireless monitors, remote sensors, watchphones, health monitors, wearable or implantable medical devices, etc.[1,5,6] For all these electronic devices, sensors are the essential components needed for their normal operations. Various kinds of sensors are available and the popular ones include touch sensors, temperature sensors, vibration sensors, position and velocity sensors, acoustic sensors, chemical sensors etc.[7,8] Sensors are usually being continuously powered by the device they are embedded in. Some sensors have to be supplied with electricity even when they are in the static standby mode in order not to miss-out any changes during the continuous sensing and monitoring. A sensor functions by capturing ambient changes and converting them into electric signals for processing. That is, a sensor operates by converting the changes in the ambient energy (mechanical energy, heat, light, etc.) into electrical energy. Unlike conventional sensors that draw power from an external power source such as a battery, the sensors developed here are all self-powered in the sense that they get their power from a triboelectric generator that harvest the clean and sustainable energy from the ambient.

1.1 Generate Electricity From Micro-Meso Scale Ambient Energy (M^2SAE)

Motion is one of the most common phenomena in the ambience, which contains an abundance of energy sources that ranges from nanoscale to the micro-meso scale and to the macro-scale (Figure 1.1). At the macro-scale end, we have large mechanical energy harvested from hydropower, wind power, tidal power, etc.[9-13] At the nano-scale end, we have energy sources from viral and cellular motions that are still largely untapped. In between, the micro-meso scale range, we have energy sources from random human motions, minute mechanical motions, etc. that are largely ignored or wasted due to their limited energy capacity and the spatial and temporal randomness of their availability. However, the random micro-meso scale ambient energy (M^2SAE) is an ideal energy source for supplying continuous power to self-powered sensors in particular, and self-powered electronics in general. The piezoelectric nanogenerator[14-23] and triboelectric (nano)generator[24-30] are rapidly being developed to harvest M^2SAE and acting as a power supply [30-32] or self-powered sensors.[33-35] In this research, we focused on the triboelectric generator due to its higher output power density. Employing patterned grating electrodes, we developed an improved triboelectric generator to harvest M^2SAE. It can also acts as a sensor by detecting the small changes in the ambient energy.

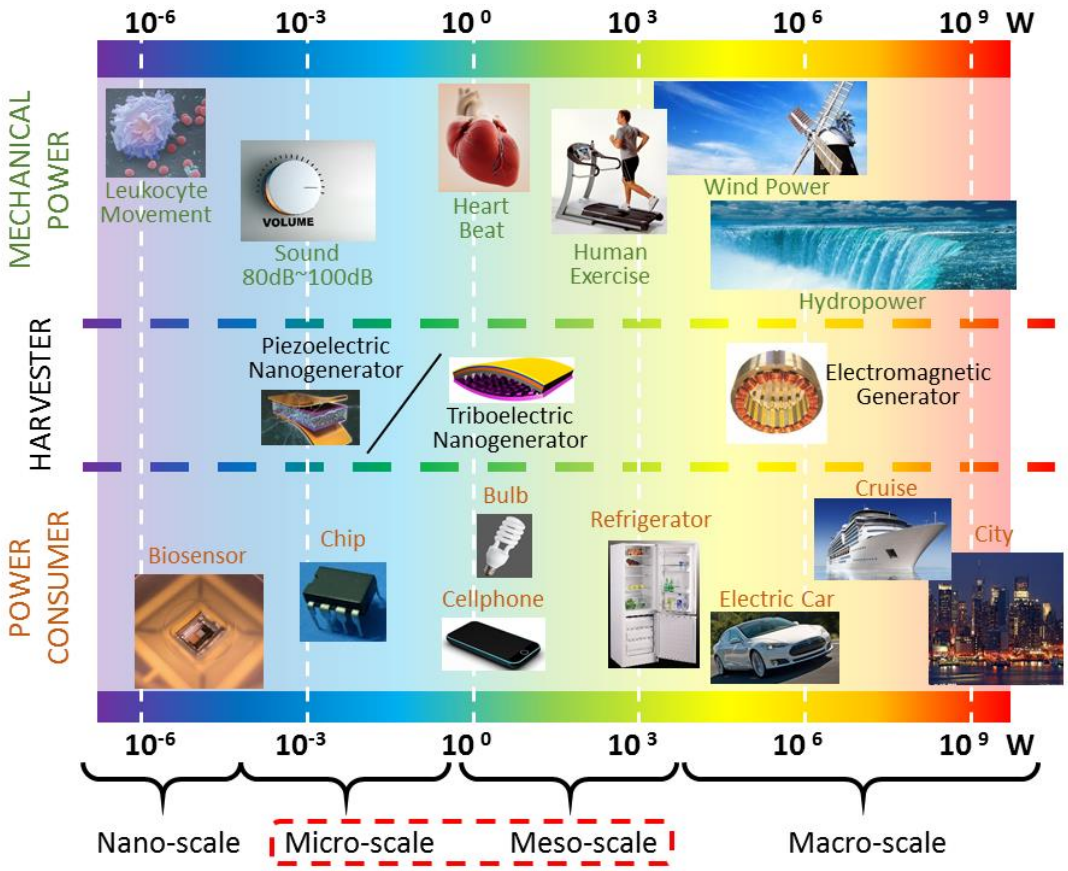

Figure 1. 1 Power spectrum spanning the different forms of energy from mechanical power generations to micro-meso scale energy harvesters to power users of varying magnitudes.

1.1.1 Electromagnetic Approach

The electromagnetic effects are one of the most well-known phenomena used for energy generation. The basic principle involves a change of the magnetic field flux in a closed looped conductor, which is usually comes in a coil shape.[36] The change can be caused by either the conductor moving relative to the magnetic field, or the magnetic field is mutative itself. For hundreds of years the phenomenon has been developed as one of the most indispensable technique for electricity generation. Very large scale electromagnetic generators are installed in hydropower stations, wind power stations, thermal power plants or even nuclear stations.

The smaller scale versions have been developed for harvesting energy from rotating motions in our daily life in products such as handheld self-powered flashlight, dynamo in bicycles, etc. At the micro scale range, researchers apply this mechanism on cantilevers for generating vibration to create a relative motion between the coils and the magnetic fields.[37-42] Two examples are presented here.[42] Prototype A is composited with static magnetic field and mobile coils. The structure has either wire-wound or electroplated coils on a silicon paddle, and a pair of oppositely polarized NdFeB magnets between which the coils are placed (Figure 1.2a). According to the author, the total volume of the devices is around 106 mm^3. The device shows a power output as high as 148 nW at a resonant frequency of around 8 KHz. Prototype B, on the other hand, is composited with static coils and mobile magnetic field. The structure is composited with a static coil fabricated on silicon located at the side, and a pair of oppositely polarized NdFeB magnets that stick to a beryllium-copper beam (Figure 1.2b). The total volume is announced at 150 mm^3. The output can reach 584 nW at its resonant frequency of 60 Hz.

Attempts to harvest random mechanical energy using electromagnetic method is successful in terms of the high efficiency with low cost. However, the presence of magnet adds a large mass to the device and this reduces the performance in terms of power density per weight unit.

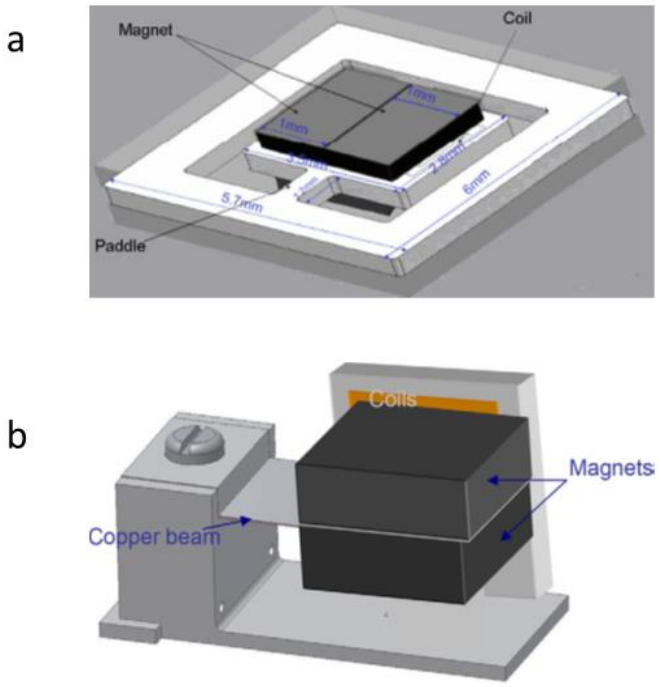

Figure 1. 2 Schematic figure for micro electromagnetic nanogenerator – (a) prototype A and (b) prototype B. (From Ref. 42)

1.1.2 Piezoelectric Approach

Piezoelectric effect is the charge accumulation caused by strain placed on material. It exists in some ceramic and crystals. Piezoelectric materials have been applied in energy harvesting in the form of bulk or thin film, to convert compressed force caused either by vertical beating or by deformation such as bending.[43]

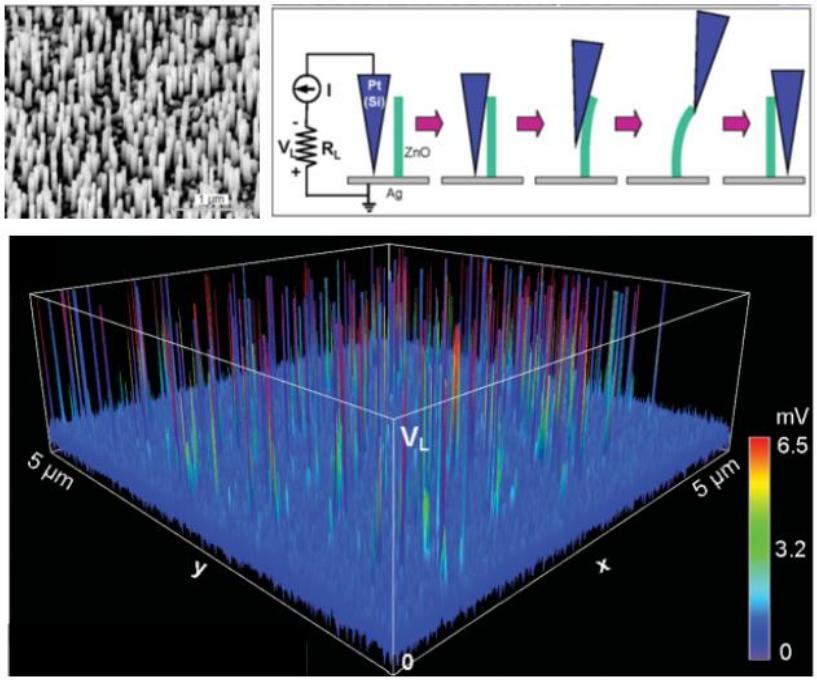

Figure 1. 3 The first ZnO nanogenerator. Left top: the SEM image of the vertical grown ZnO nanowire. Right top: the schematic drawings showing the steps of AFM tip sliding over the ZnO nanowire. Bottom: The 3-D graph showing the voltage output distribution from ZnO nanowire array. (From Ref. 20)

In 2006, a "nanogenerator" was brought into the world by fabricating arrays of vertically grown ZnO nanowires, which has piezoelectric effect mostly along the grown direction, on conductive substrates.[20] The ZnO nanowires were swapped to bent and released by AFM tip during which electron flow was generated between tip and substrate, explained by the coupling effect of both piezoelectric effect and semi-conducting properties of ZnO nanowire (Figure 1.3). It was the smallest generator reported at that time, with an output voltage of 9 mV and a power density estimated up to 10 pW/μm^2. Following works[17,21,31,44-47] based on ZnO nanogenerators not only broadened the response to different type of mechanical energy such as stretching, compressing or bending, but also largely increased its output open circuit voltage to 57 V (Figure 1.4).[31,47]

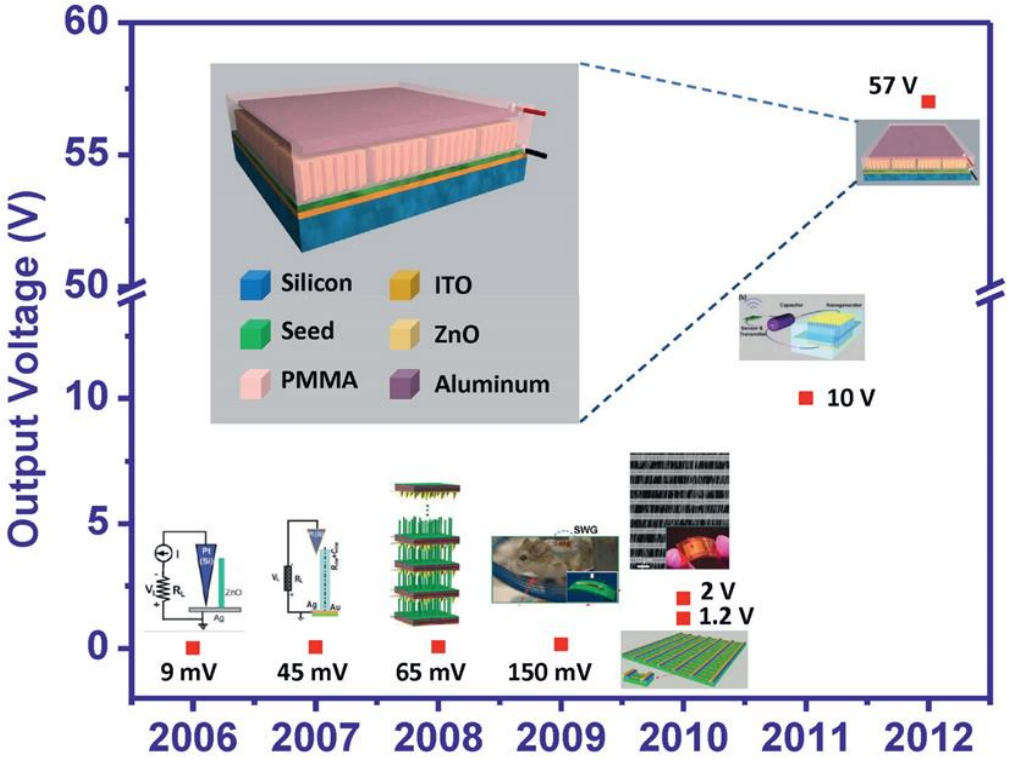

Figure 1. 4 The development of piezoelectric nanogenerators. (From Ref. 31)

1.1.3 Triboelectric Approach

Triboelectric effect, which is the behavior of charge transfer across the interface of two different materials when brought into contact in the form such as vertical touching or parallel friction, caused by chemical potential difference of the two surfaces.[48] The phenomenon has been observed long time ago and was mostly treated as harmful effect to electronic devices. Until recently in 2012, the first triboelectric nanogenerator has made the electricity generating from triboelectric effect possible.[26] The working principle of the TENG was based on the coupling effect of triboelectric and electrostatic, fulfilled on a multi-layered structure made of Au electrodes, PET film and Kapton film (Figure 1.5a). At the stage of bending, PET and Kapton were firmly contacted, resulting the electrons from

surface of PET ejected into Kapton. When released, the separation of the positive and negative charge caused by mechanical motion will produce unbalanced potential, driving electrons flow from Au electrode on the back side of the PET film to the one on Kapton. Electrification charges are neutralized when the two surfaces are brought together during following bent, causing a flowing back of the electrons between electrodes (Figure 1.5b).

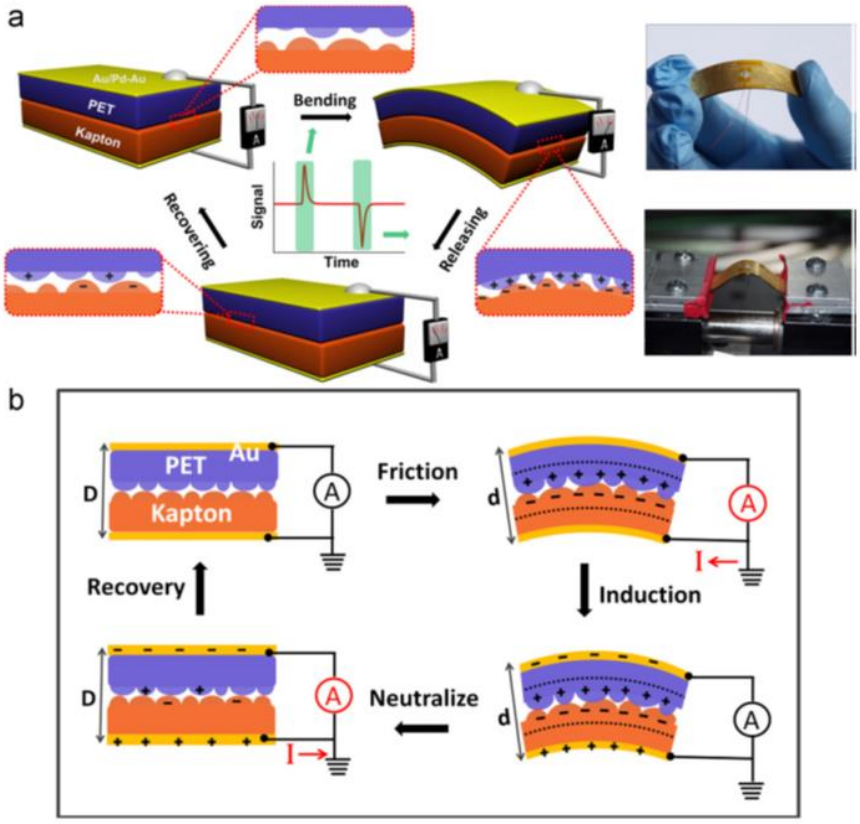

Figure 1. 5 The first Triboelectric nanogenerator. (a) The schematics of the triboelectric nanogenerator. (b) Its working mechanism in details. (From Ref. 26)

The direction of electron transfer during contact is determined by the order of electrification property of the material listed in Table 1.1,[49] which is made from the tendency of gaining or losing electrons of the material. One from the negative end in the list is likely to gain electrons when contacted with any of the other material toward the positive end. The longer the span is in the order, the larger the amount of charge transfer density is likely to occur.

Table 1. 1 Triboelectric series for common materials (From Ref. 49).

Positive			Negative
	Polyformaldehyde 1.3-1.4	(continued)	
	Etylcellulose	Polyester (Dacron)	
	Polyamide 11	Polyisobutylene	
	Polyamide 6-6	Polyuretane flexible sponge	
	Melanime formol	Polyethylene Terephthalate	
	Wool, knitted	Polyvinyl butyral	
	Silk, woven	Polychlorobutadiene	
	Aluminum	Natural rubber	
	paper	Polyacrilonitrile	
	Cotton, woven	Acrylonitrile-vinyl chloride	
	Steel	Polybisphenol carbonate	
	Wood	Polychloroether	
	Hard rubber	Polyvinylidine chloride (Saran)	
	Nickel, copper	Polystyrene	
	Sulfur	Polyethylene	
	Brass, silver	Polypropylene	
	Acetate, Rayon	Polyimide (Kapton)	
	Polymethyl methacrylate (Lucite)	Polyvinyl Chloride (PVC)	
	Polyvinyl alcohol	Polydimethylsiloxane (PDMS)	
	(continued)	Polytetrafluoroethylene (Teflon)	

Improvement of the triboelectric nanogenerator has never stopped since the first invention. Nanoparticles and nanostructures are introduced to enhance the output.[27,28] Mainly based on contacting mode[50] and sliding mode,[51,52] or a combination of the two,[53] the working principle is broadened to be applied in single electrode mode[54] or freestanding mode[55] TENG. Various designs of TENG come out to adapt different situations, which can harvest energy from a wide range of mechanical energy forms including not only bending, but also compacting, sliding or rotating, etc. TENGs are fabricated with multiple layered structure to increase output.[56] Segments are applied to the contacting surface to improve the efficiency of the electricity producing process.[57,58] Output of the generators is typically several to several hundred Volts in voltage and the output density could reach as high as 313 W/m^2 (Figure 1.6).[30] Such generators were successfully applied in charging portable devices like cellphone.[28,59]

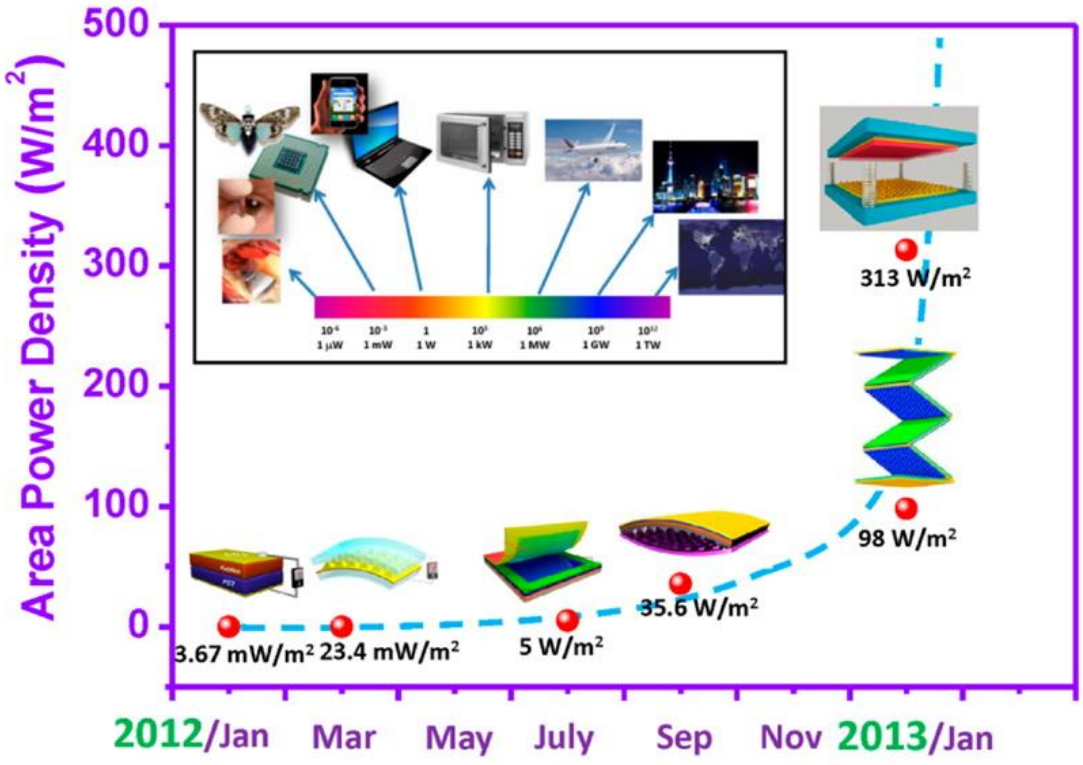

Figure 1. 6 Development of triboelectric nanogenerators. (From Ref. 30)

Triboelectric nanogenerator is a promising mean of energy harvester for surrounding random mechanical energy however calls for further optimization. Part of my work in this document includes the optimized design based on grating structured electrification surface on a sliding mode TENG.

1.2 Kinematic Sensors

Kinematic sensing is considered one of the most significant technology in modern society. They are crucial to industries such as automation, transportation and robotics, etc. People mostly concern about the position (or angle) and the velocity of a moving body, sometimes not only the quantity but also the direction. The effort of automatically

measuring the kinematic parameters takes years and a lot of prototypes based on various principles are established, including approaches based on potentiometers,[60,61] magneto resistive sensing,[62,63] magnetic field sensors,[64] optical encoders,[65-67] capacitive sensing,[68,69] piezoelectric sensors,[70,71] and triboelectric technology.[35,72-74] Some of the examples are introduced in this chapter.

1.2.1 Potentiometer Position Sensor

The potentiometer position sensor is usually composited with a linear or arc shaped resistive material and a conductive wiper sliding along the material (Figure 1.7),[61] for linear position or angle sensing, respectively. Measuring resistance between the wiper and one of the terminals of the resistive material tells the current position of the wiper. It is simple and costless, however, the smoothness and linearity problem bring disadvantages to the application. Moreover, to endure long life time use, the supplying current should be limited to a low level, which brings in challenge in separating noise from real signal.

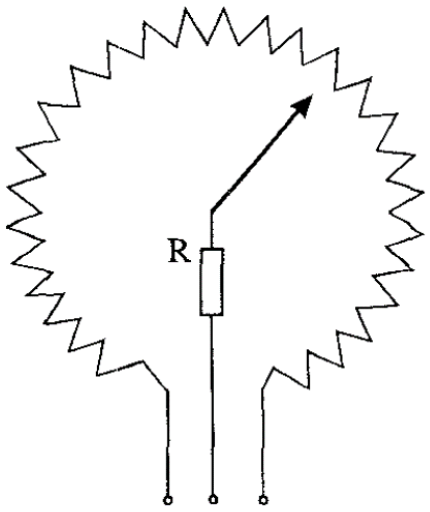

Figure 1. 7 Schematic for a potentiometer angular position sensor. (From Ref. 61)

1.2.2 Optical Encoder

Optical encoder as position sensor is usually composited with an engraved coded plate or disk, light emitting diodes on one side and photodetectors on the other side (Figure 1.8).[61] Different codes read by the detector reflect the position or moving speed of the plate or disk. The technique has been well developed and was applied in mechanical mouse. The advantage of the optical encoder is the non-contacting working mode with high accuracy. However, the resolution is limited by the coding capacity of the plate and disk.

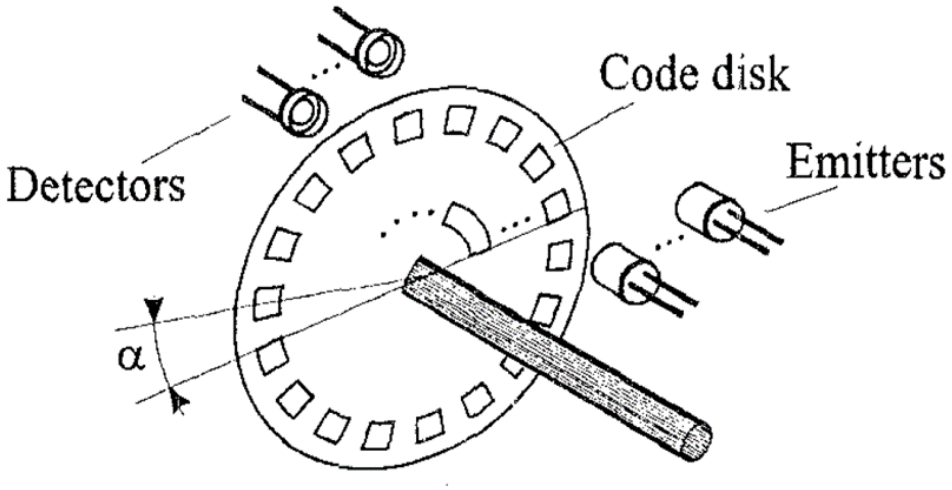

Figure 1. 8 Schematic for an angular position sensor based on optical encoder. (From Ref. 61)

1.2.3 Capacitive Position Sensor

Capacitance between two conductive bodies is about to vary when the topologic of the conductive bodies changes. Based on this property, touch sensor, pressure sensor and position sensor are developed. For example, the design of capacitive angular sensor is built on a differential capacitor shown in Figure 1.9.[61] The structure is composited with a rotator blade and two stationary blade separated with spiral space. The spiral design guarantees the linear property of capacitance between blades toward the measured angle.

Capacitive position sensors enjoy high accuracy and resolution with non-contact working mode. However, the monitored value could be affected by dust, electro-magnetic interference or tilted axis factors.

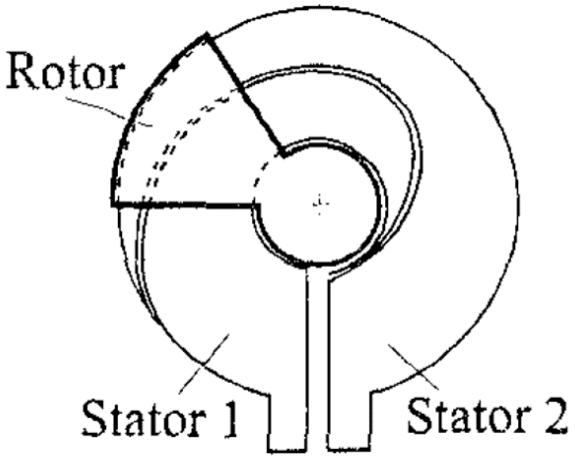

Figure 1. 9 Schematic for a capacitive position sensor. (From Ref. 61)

1.2.4 Piezoelectric Velocity Sensor

Sensors mentioned above are passive sensors, which need external power supply in order to continuously monitor the kinematic parameters. Sensors based on piezoelectric effect, on the other hand, are active sensors due to its property of response to the ambient energy change by positively output electric singles, which mostly a pulse. If arranged smartly, the pulse can be used as a triggering signal for speed calculation. Example based on a ZnO nanowire piezoelectric sensors installed with interval on the ground waiting for being pressed from passing tires demonstrated the application of speed sensing.[71] The recoded time between successively pulse signals produced by 2 piezoelectric sensors reflects the moving speed of the tire between the 2 monitoring sets (Figure 1.10).[71]

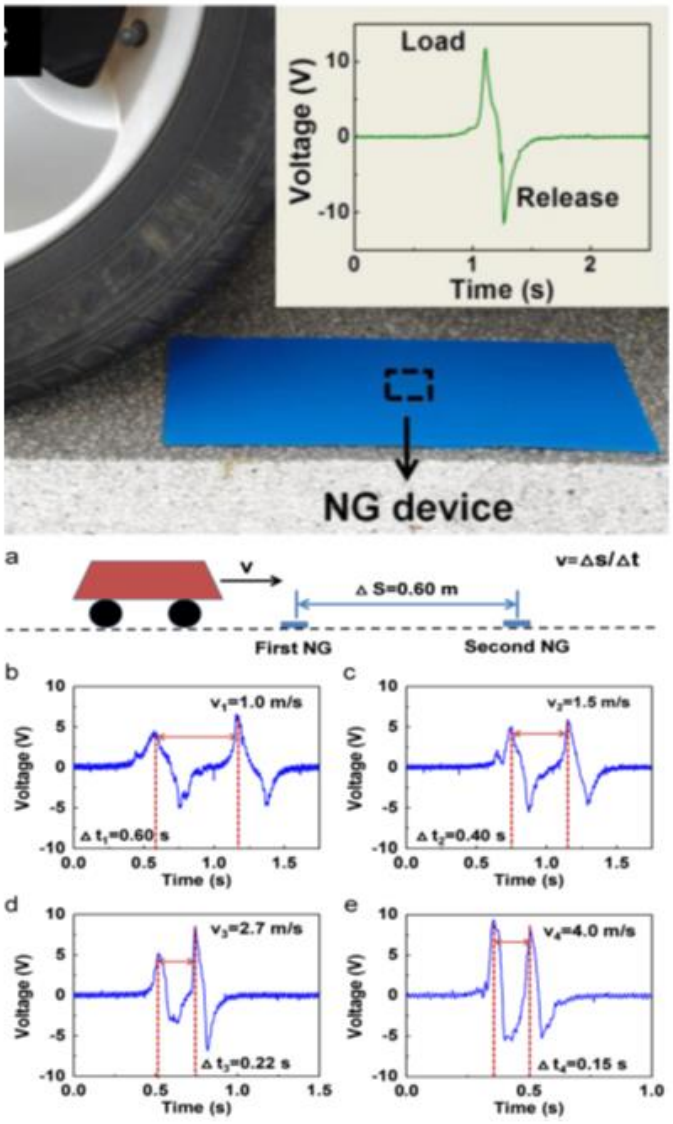

Figure 1. 10 ZnO nanowire piezoelectric sensors act as a speed monitor. The devices are triggered by pressure from the tire. Two as-fabricated devices located with a certain distance form a pair of speed monitor by recording the time span between the successively peaks they produce. (From Ref. 71)

Moreover, another demo attaching a piezoelectric sensor onto the inner surface of a tire also successfully measured velocity indirectly from the various degree of tire deformation when contacted to the ground during different rotating speeds (Figure 1.11).[70]

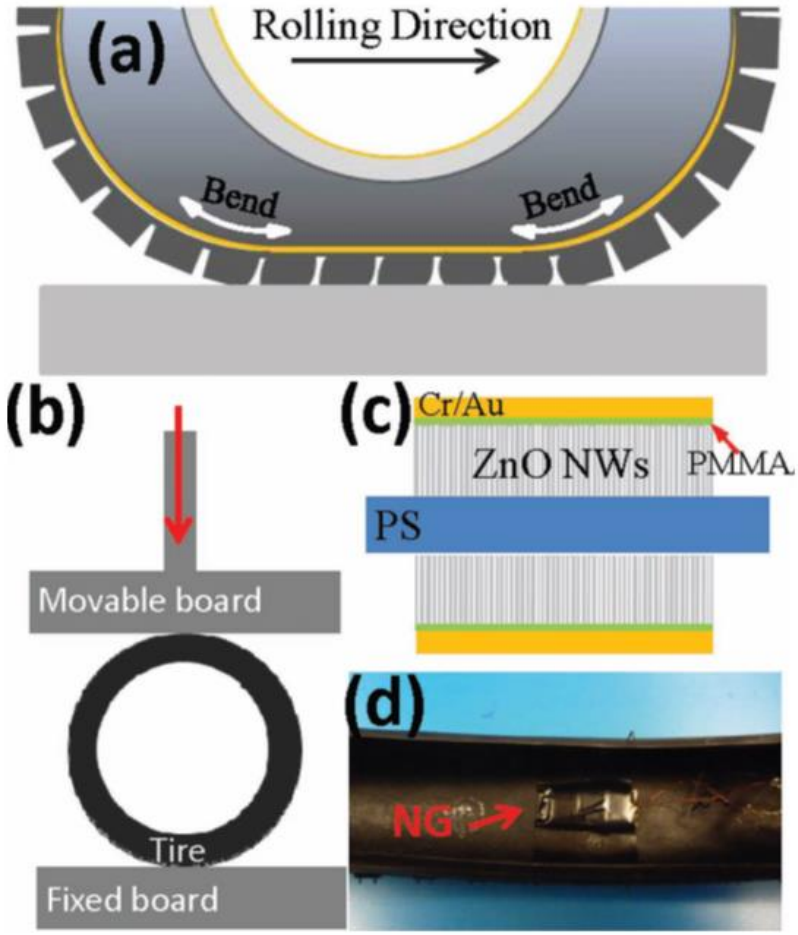

Figure 1. 11 The Piezoelectric nanogenerator as speed sensor in a tire. (a) Tire deforms when rotating on the ground. (b) The set up for in-lab experiment. (c) The intersection of the device. (d) The sensor was stick to the inner side of the tire. (From Ref. 70)

The effort using piezoelectric effect as an active sensing approach is encouraging. However, the low output and the high expense in fabricating piezoelectric sensor limited its application toward large scale. Besides, there is so far not much information about the durability of as-fabricated sensors in normal application.

1.2.5 Triboelectric Velocity Sensor

Not long after the first triboelectric nanogenerator was developed,[26] the triboelectric effect was introduced to building active sensors, due to its natural working mechanism which positively produces signal during mechanical motion. Simulation study on triboelectric nanogenerator shows that the open-circuit voltage is well corresponded to the topologic position of the two triboelectric material relative to each other (Figure 1.12).[75] As a result, the amplitude of the open-circuit voltage can be used as a reference value in presenting the displacement.

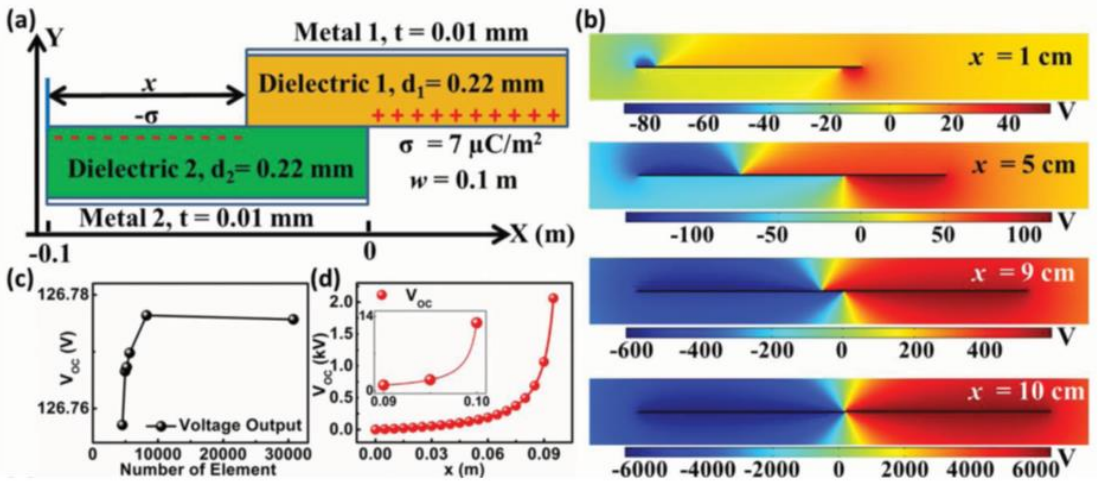

Figure 1. 12 Simulation results on output voltage for a sliding mode triboelectric nanogenerator. (a) The schematic showing the parameters during sliding. (b) Potential distribution during the sliding at different displacements. (c) Effect from number of elements in the simulation. (d) Relationship between the voltage output and displacement. (From Ref. 75)

Later on, the amplitude of the short-circuit current was discovered related to the sliding velocity of the sliding-mode triboelectric nanogenerator, due to the faster exchange of the electrons driven between the electrodes. The segmentally designed disk triboelectric nanogenerator (Figure 1.13 a) is one of the example that was successfully

used in rotary velocity sensing.[58] From the result we can see the output current shows almost linear relationship with the rotating speed (Figure 1.13 b).

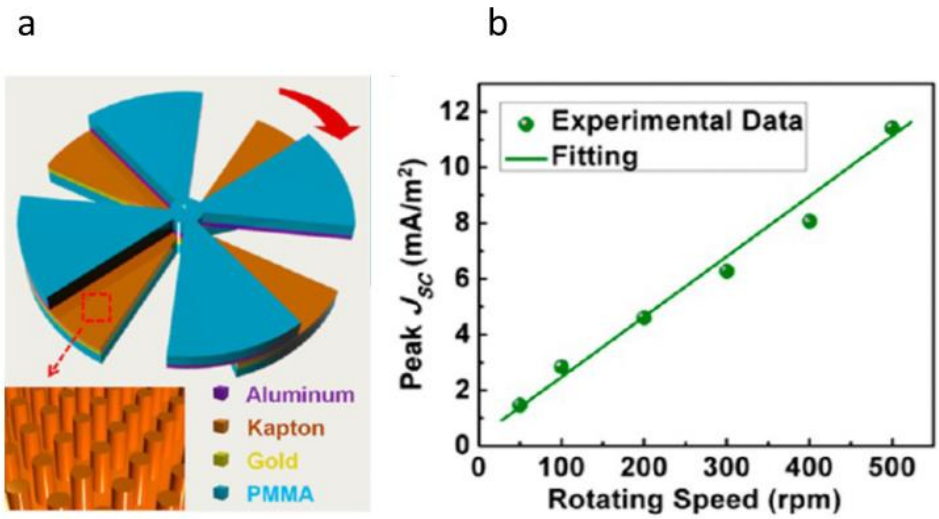

Figure 1. 13 Rotary triboelectric nanogenerator as speed sensor. (a) The schematic showing the structure of the device. (b) The relationship between maximum current output and rotating speed. (From Ref. 58)

As the contact mode triboelectric nanogenerator produce pulses when endured with vertical compact, the behavior is very like that of a piezoelectric nanogenerator but in much larger magnitude. Therefore the triboelectric sensor could also be used as positioning monitor by arranging individual devices into an array.[73] Benefited from the considerable output by the sensor, the position monitoring can be directly imaged by lighting up LEDs at corresponding position (Figure. 14).

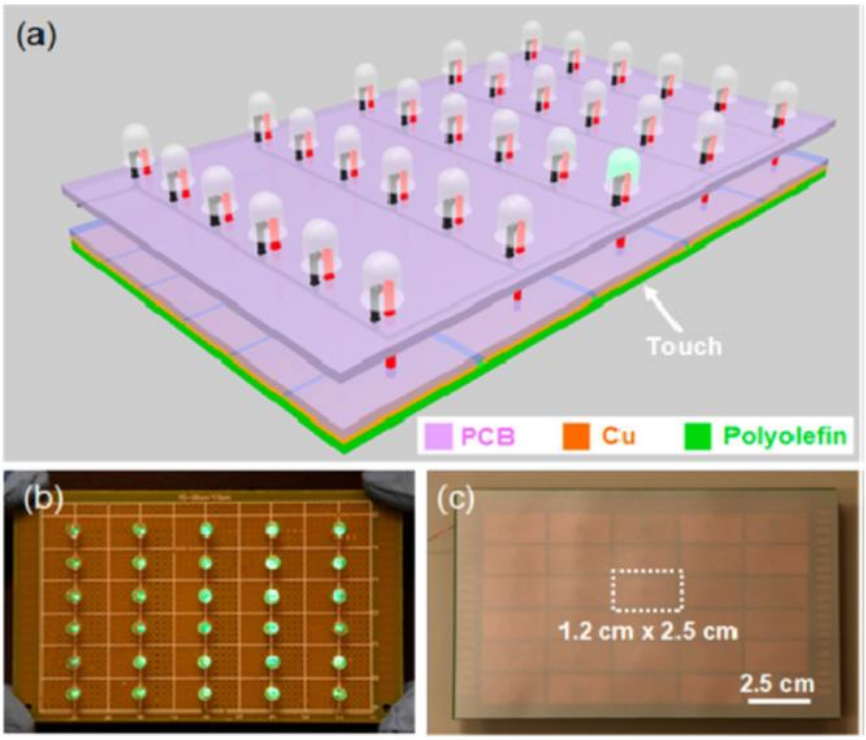

Figure 1. 14 Direct imaging of position sensor based on triboelectric effect. (a) The schematic of the device array. (b) The front side of the device is LED array for imaging. (c) The back side of the device is the triboelectric array for detecting. (From Ref. 73)

Moreover, it has been reported that triboelectric (nano)generators can be applied in vibration sensor,[72] acoustic sensor,[76,77] biosensor,[78] acceleration sensor,[79] tactile sensor,[80,81] chemical sensor,[82,83] and so on, making triboelectric technology an attractive topic in various sensing fields.

Triboelectric technology is a promising approach in building active kinematic sensors not only because it produce reasonable output, but also due to its simple structure, wide range of material selection and cheap fabrication process. However, current kinematic sensing are based on the main reference of output magnitude, which is not quite reliable and stable under different testing condition or among different individual sensors.

The disadvantage limited the set-up of uniform standard in qualifying the sensors. Besides, current designs such as the positioning monitor sensor is complicated in wire connection, which significantly drags the large-scale application of the triboelectric kinematic sensor. As a result, from both the structure design and the signal recognition, there is a lot of room for the triboelectric sensor needs to be optimized.

1.3 Dissertation Layout

In my work, stable, reliable yet robust kinematic triboelectric sensors are demonstrated by modifying the electrification surface with patterning design. In Chapter 2, we firstly come with a case-encapsulated grating structural designed sliding mode triboelectric nanogenerator, in the purpose of demonstrating the grating pattern is efficient and working well with packaged designed structure. In Chapter 3, such structure with improvement is then contributed to a dual-mode active velocity sensor that can be installed to either rotary or linear velocity sensing situations. Further in Chapter 4, we demonstrated a 1-D vector sensor that is able to measure displacement and velocity as well as their direction, based on dual channel measurement technology. The structure is easy to expend into 2-D with demonstration included this document as well. Later in Chapter 5, an encoded triboelectric angular sensor is presented showing the absolute positioning measuring and quasi-static positioning monitor. Finally, a conclusion is provided in Chapter 6 to integrally summarize my research.

CHAPTER 2

CASE-ENCAPSULATED TRIBOELECTRIC NANOGENERATOR FOR HARVESTING RECIPROCATING KINETIC ENERGY; A "PATTERNED CONTACT SURFACE" APPROACH

2.1 Triboelectric Nanogenerator as Energy Converter for Harvesting Reciprocating Kinetic Energy

Reciprocating motion is an extremely common mechanical motion and it is commonly encountered in the environment, e.g. vibration of objects, oscillation of piston, motion of waves, swing of human limbs, and mechanical piston movements, etc. Energy stored in these motions are typical M^2SAE. The features of these motions are back-and-forth with long distance, mostly low frequencies with large amplitude, and frequency fluctuations. Previously developed vibration-harvesters[37,72,74,84,85] are good for low-amplitude and high-frequency excitations, which may not be efficient for capturing the energy of a back-and-forth motion with characters mentioned above. On the other hand, the sliding mode of TENG, which derives its energy from sliding motion, is developed specifically to harvest the energy contained in a reciprocating motion. In the original design,[51] sliding mode TENG operates with a low efficiency and the work here reports on a significant improvement of its energy capture efficiency.

2.1.1 Triboelectric Nanogenerator in Sliding Mode

As mentioned in Chapter 1.1.3, TENG with sliding mode was developed soon after the very first TENG was invented.[51] As shown in Figure 2.1, the sliding mode TENG is consisted with two contacting pieces of different layered materials that has distinctive

triboelectric properties according to the triboelectric series (Table 1.1), with metal deposited at the back side of each layers as electrodes. Opposite charges are transferred to contacting surface of each material caused by triboelectrification. The charges then conduct laterally relative motion along with the material when the TENG operates with reciprocating slides (Figure 2.1), resulting in alternating electric potential in surrounding area, driving electrons flow back and forth between metal electrodes.

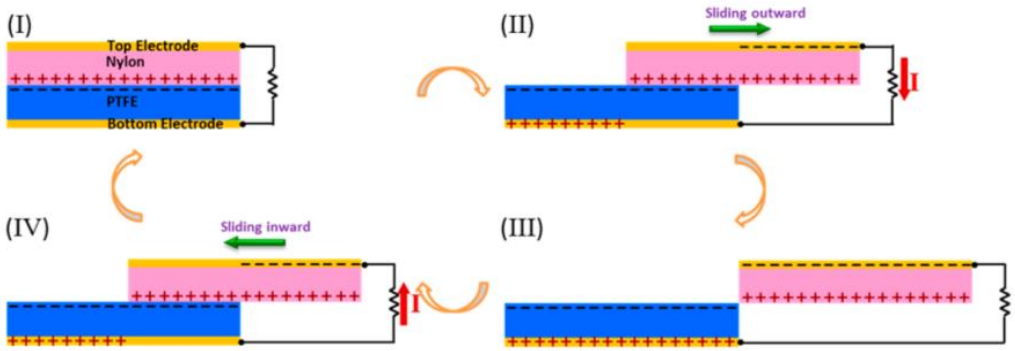

Figure 2. 1 Working principle for sliding mode TENG. (From Ref. 51)

Original sliding mode TENG generates one positive and one negative current signal during a complete cycle of sliding behavior,[52] which is shown in Figure (2.2). The output signal depends significantly on the sliding speed,[51,58] which correlates with the flow rate of the charges from one electrode to another.

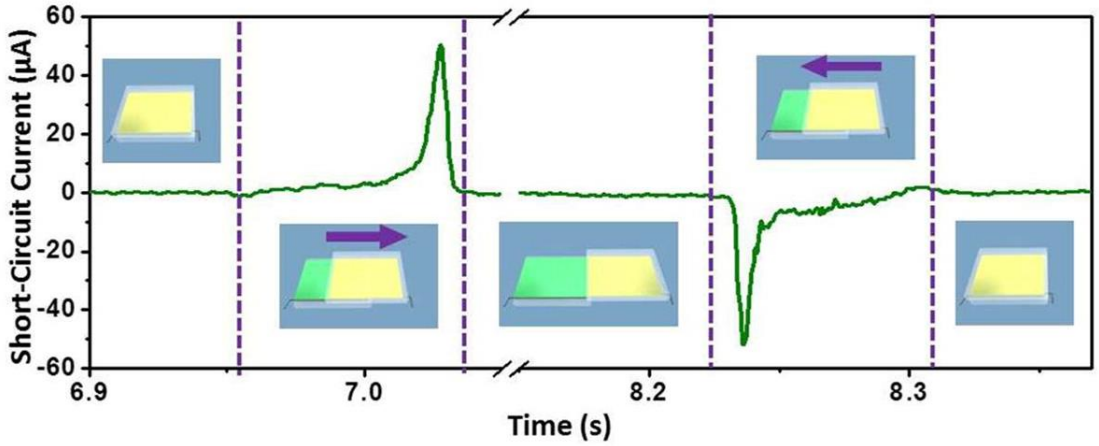

Figure 2. 2 TENG generates one positive and one negative current signal during a complete sliding cycle. (From Ref. 52)

2.1.2 Modifying the Electrification Surface with a Grating Pattern

To maximize the energy capture of the sliding energy, one solution is to increase the flow rate of the charges. Attempts was conducted by separating the integral piece of contacting surface as well as the electrodes into grating aligned strips with uniform width to multiply the cycles of charge flow during one slide.[52] The current signal was then improved by number of positive and negative peaks that are consistent with the number of grating strips (Figure 2.3a to c). Compared with the original design with same contact surface area, the total charge movement is increased by $n/2$ where n is the number of strips and the denominator of 2 is due to the 50% decrease of the electrification area as a result of the grating pattern.

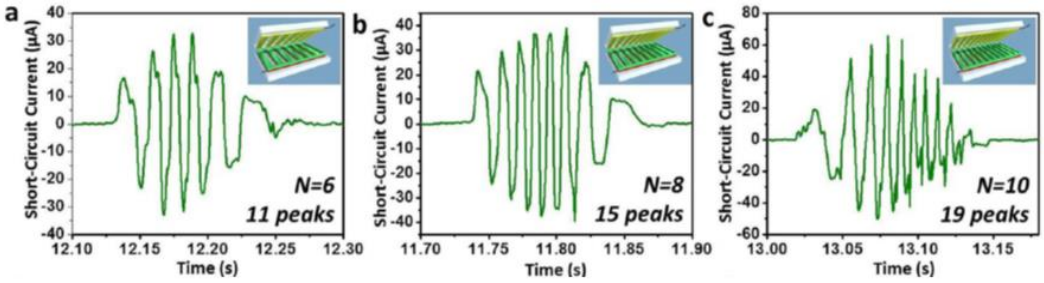

Figure 2. 3 Output performance of a TENG with grating pattern at the contact surface. (From Ref. 52)

2.1.3 Improving the Output by Multiple Electrification Layers

A sliding TENG is more like a two-dimensional object with all its motion happening in the plane. Therefore, it is possible to increase its performance by using multiple functional layers. As all the layers are operated simultaneously, the electrodes from each individual layer can be either joined in a parallel connection to enlarge the current output, or in a series connection to amplify the voltage output. Attempts to double or higher the number of layers to achieve a bigger output have been successfully reported in several papers (Figure 2.4a).[86,87] The output had a positive proportional relationship with the number of functional layers (Figure 2.4b). However, the strategy of increasing layers may sometimes add thickness to the device.

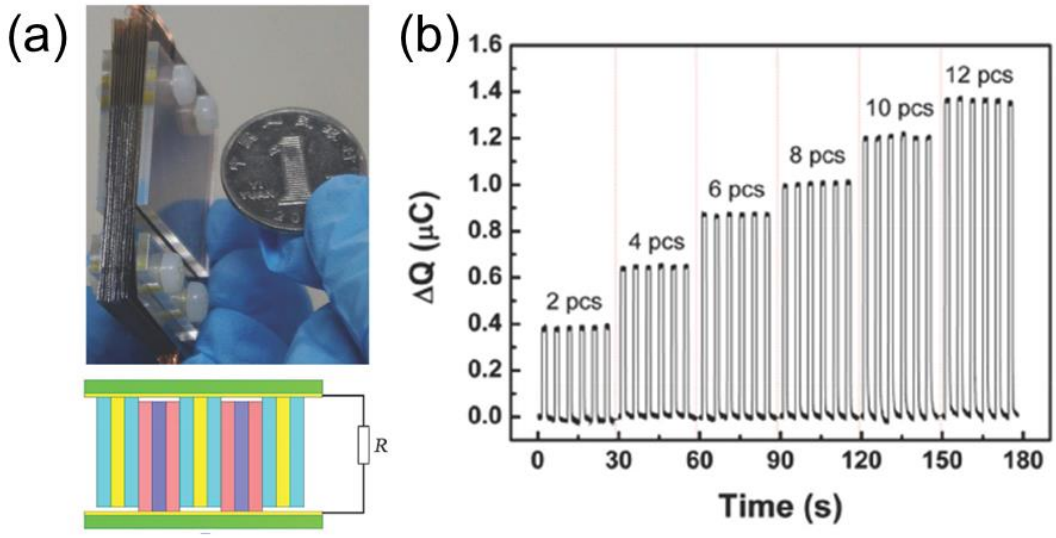

Figure 2. 4 Sliding TENG with multiple friction layers. (a) Actual and schematic picture of multi-layered sliding TENG. (b) The measured transferred charge quantity ($\triangle Q$) with different number of friction layers. (From Ref. 86)

In this work,[88] we integrate a grating-patterned design with a double-layered design without contributing to the thickness dimension of the layer. By selecting metal as both the electrification material and the electrode, the TENG was successfully fabricated to harvest energy from reciprocating motions driven by both direct and inertia forces. The TENG was proven to effectively harvest energy from human body motions and wave motion of the water surface. Further, the grating pattern contains information about the motion and this makes it viable to monitor kinematic parameters of positions and velocities.

2.2 Design and Fabrication of the Case-Encapsulated TENG

2.2.1 Design of the Case-Encapsulated TENG

The structural configuration of the cTENG is shown in Figure 2.5a. The main body is fabricated by using two concentric cylinders that allows them to move in a coaxial 1-D motion relative to each other. The basic principle of the cTENG relies on sliding triboelectrification at the interface and on electrostatics during movement. The outer case was wrapped tightly around the inner cylinder allowing the two cylindrical structures to conduct a reciprocating motion against each other. According to the triboelectric serials for common materials (Table 1.1), two different materials with a maximized opposing triboelectric behavior were chosen for achieving maximum charge transfer density or contact triboelectrification. Polyimide film (Kapton®) was selected as one of the electrification materials for generating the triboelectric charges and copper is the other to function as an electrode and to provide a supporting substrate for the Kapton. The Kapton film was chosen as it exhibits good electrification performance and possesses a high tensile strength for improved durability. On both sides of the Kapton film, copper strips with width of 2 mm were deposited with a linear pitch of 4 mm. The electrode patterns on different sides of the film exhibited a linear shift of half pitch so that they are complementary to each other (Figures 2.5b). Electrodes on the same side were electrical connected by bus electrodes (Figure 2.7a).

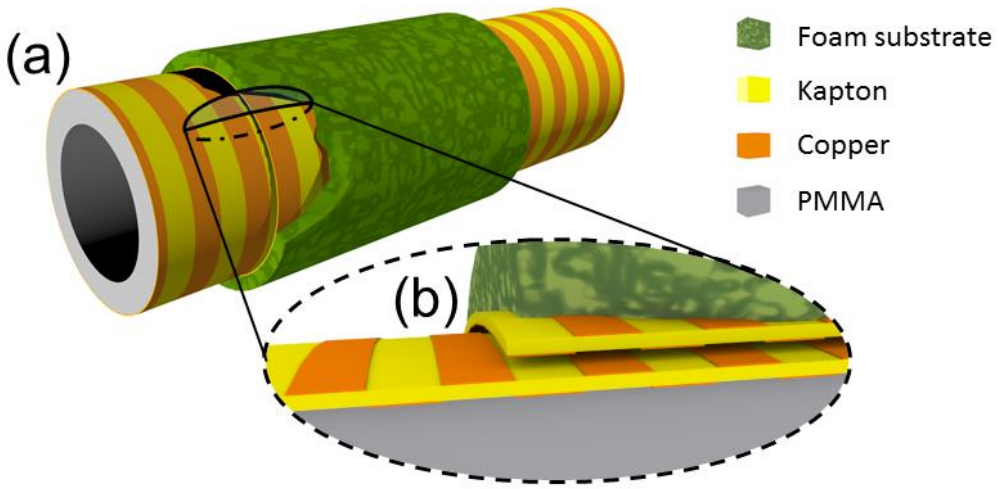

Figure 2. 5 Case-encapsulated triboelectric nanogenerator (cTENG). (a) 3D model of cTENG and (b) cross section view.

Two Kapton films having the same as-fabricated electrode patterns were applied on the outer surface of an acrylic tube and the inner surface of a foam tube, respectively, to form the contact surfaces (Figure 2.5b). Copper stripes from the contact side of one Kapton film and from the backside of the other film constitute a pair of single-layered grating patterned triboelectric generator. A total of 2 sets of individual generators were fabricated onto the 2 Kapton films, and the increase in thickness is insignificant compared to the thickness of the original sliding TENG design (Figure 2.6).

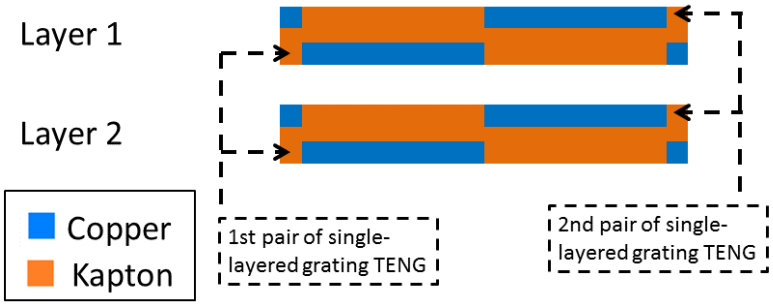

Figure 2. 6 Schematic figure shows the 2 pairs of TENG mounted in one design without adding device thickness.

To parallel connect the two layers of generator together, all copper strips on the two contact surfaces were connected by electric wires to form a common inner electrode (IE), while those on back surfaces of the Kapton films constituted an outer electrode (OE) (connections can be seen in the schematic sketch of the working mechanism in Figure 2.9). Spherical polytetrafluoroethylene (PTFE) nanoparticles were spread between the contact surfaces (Figure 2.7b) to reduce the inter-layer friction and to further improve the energy conversion efficiency (see Chapter 2.5). The actual decomposed and fully assembled cTENG is respectively shown in Figure 2.8.

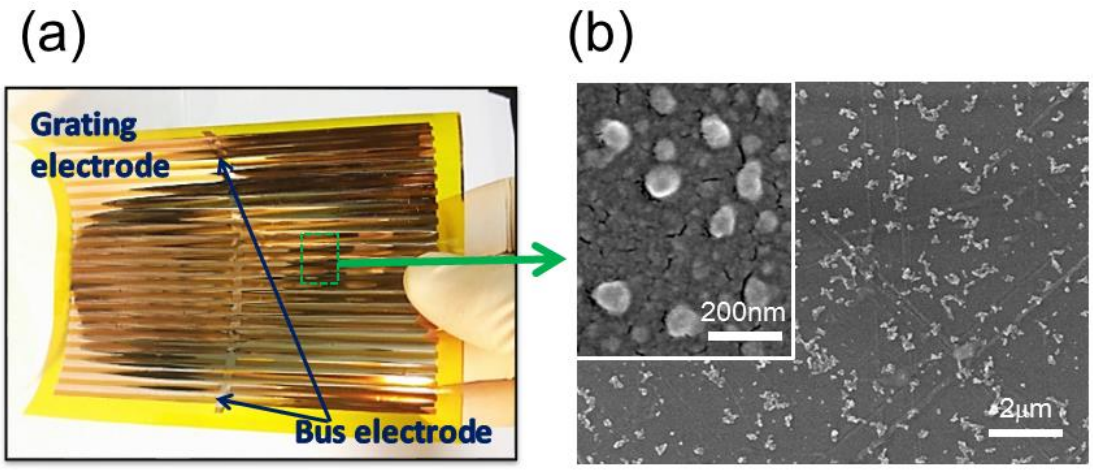

Figure 2. 7 Kapton film with grating electrode on both side of the surface. (a) Bus electrodes connect all the grating electrodes together. (b) SEM image presenting PTFE nanoparticles were spread on the triboelectrification surfaces.

2.2.2 Fabrication Process of the Case-Encapsulated TENG

The fabrication process and relative parameters are presented in this paragraph. Two pieces of Kapton film (25μm thick) with size 12 cm × 15 cm (longer one) and 12 cm × 7.5 cm (shorter one) were prepared and cleaned with isopropyl alcohol. Two pieces of acrylic board (1.5 mm thick) with size 12 cm × 15 cm (longer one) and 12 cm × 7.5 cm (shorter one) were prepared by laser cutter. Hollow strips with individual size 0.2 cm × 12

cm were brought on such acrylic boards by laser cutter, arranged parallel in a linear pitch of 4mm, spread over the available area of two boards. A perpendicular column across all the strips at their middle point was also engraved. These pierced boards were used as masks for electrode deposition. Kapton films were covered with corresponding-sized acrylic mask on one side and were conducted with copper electrode deposition by physical vapor deposition facilities for the first time. Then same masks were used for the other surface of pre-treated Kapton film with a linear shift of 2 mm before conducted with copper deposition. Acrylic cylinder rod with length 15 cm and diameter 3.81 cm was coated with thin layer of Polydimethylsiloxane (PDMS) on the surface, and was then wrapped with pre-treated Kapton film (longer one) as inner part. PTFE particles (DuPont Teflon® Non-Stick Dry-Film Lubricant) were spread onto the surface of this Kapton film (Figure 2.5b). The other pre-treat Kapton film (shorter one) was then wrapped over (but not stuck to) the inner part, followed by another layer of 0.3 cm thickness foam tape with double side sticky. Polyethylene terephthalate (PET) film with 75 μm thickness was finally applied onto the outer surface of foam tape as a support material to complete the casing structure (Figure 2.8). Outer part was able to move smoothly along the inner part in the manner of piston form. Metal wires were connected to electrode from each surface of the two Kapton films, with electrodes located between contacting surface set as inner electrode (*IE*), on the back sides of Kapton films set as outer electrode (*OE*).

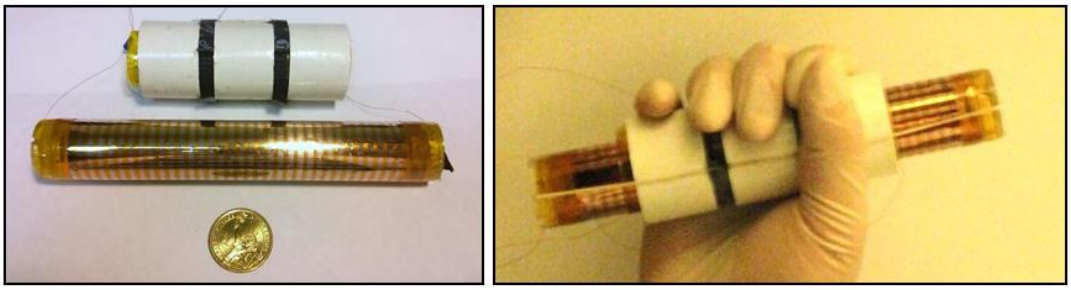

Figure 2. 8 Actual decomposed and fully assembled cTENG. Reference coin used in the photo was a common US quarter.

2.3 Simulation of the Working Mechanism of a Case-Encapsulated TENG

2.3.1 Working Mechanism Analysis

The electricity generation mechanism of the cTENG is illustrated in Figure 2.9. The outer tube slides relative to the inner tube, forming a reciprocating movement. As working mechanism of the cTENG, when Kapton and copper are brought into contact, the difference in triboelectric polarities (Table 1.1) determines that electrons are injected from copper into Kapton (Figure 2.9a).[30,89,90] The triboelectric charges are equivalent in amount but opposite in polarities.

At the state shown in Figure 2.9a, all triboelectric charges are balanced, producing no electric field in surrounding space provided that edge effect is ignored. Once sliding motion take place, the mismatch of the previous-aligned strips begins. As a result, negative triboelectric charges on the surface of Kapton films become uncompensated, producing a dipole polarization along the direction of the displacement and thus a potential difference between the *IE* and the *OE*. If the two electrodes are electrically connected through an external circuit with resistance (Presented by *R* in Figures 2.9), such a potential difference results in a flow of electrons from the *OE* to the *IE*, which screens the potential difference induced by the triboelectric charges (Figure 2.9b). Consequently, a current from the *IE* to the *OE* is simultaneously generated. As the mismatch continues to expand due to sliding, more positive charges are transferred from the *IE* to the *OE* until the state shown in Figure 2.9c is reached. Further sliding motion beyond this state leads to a reverse flow of electrons between electrodes, which corresponds to a current with an opposite direction (Figure 2.9d). Therefore, a sliding distance for a pitch period can generate a complete cycle of alternating current (Figure 2.9e).

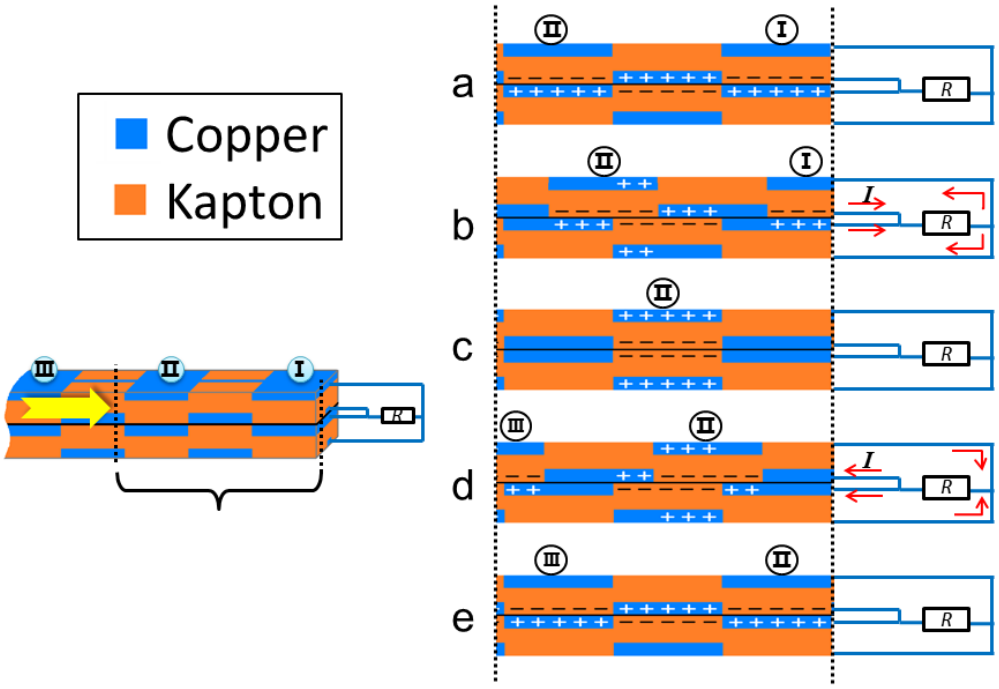

Figure 2. 9 Working mechanism for cTENG. Part area of the cross section is schematically shown, with inner electrodes (IE) and outer electrodes (OE) connected together respectively. The two electrode is connected over external resistance *R*. Certain electrodes are flagged with Roman numerals to mark its relative movement in (a)-(e). Red arrows indicate the direction of current.

2.3.2 Software Simulation Parameters

The Comsol Multiphysics® 4.2 software was used to simulate the open circuit voltage of cTENG. The physical model "Electrostatics" was selected for simulating both open-circuit voltage and short-circuit charge transfer. An estimated charge density of -20 μC/m^2 was pre-applied on the Kapton surface[29] as an equivalent result of electrification. To reduce the computing complexity, a local representative including one unit of strip sliding over 3 units of strips was simulated (Figure 2.10). The simulation is focused on the cross-sectional direction and was conducted in a 2-Dimesion model. To calculate the charge, the depth of the 2D model was set large enough to meet the actual working area. The width of the electrodes and the thickness of the Kapton were assigned with actual value

given in Chapter 2.2.2. The relative permittivity of Kapton was set equal to 3.4. The surrounding space was set as air with a relative permittivity of 1.0. The outer boundary of the air was set large enough to be treated as infinity and was set as 0 (ground) in the electric potential.

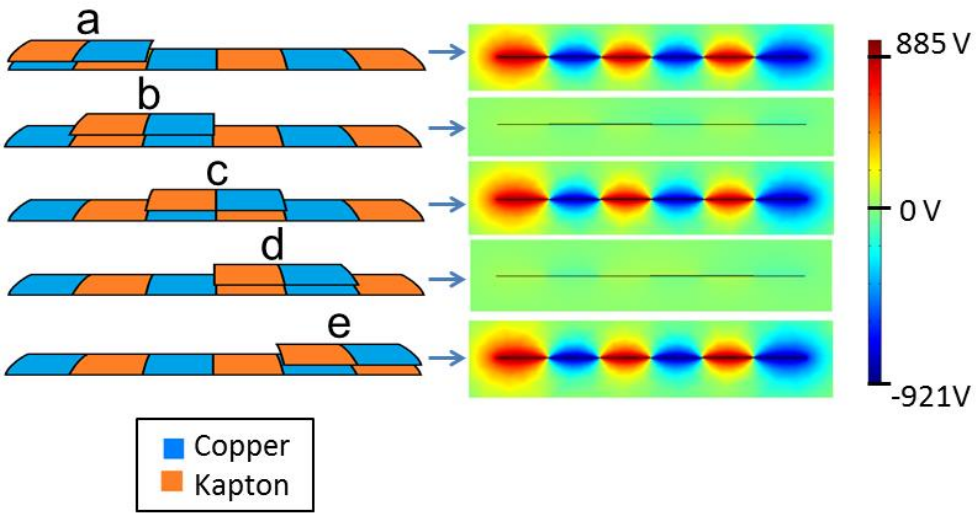

Figure 2. 10 Simulation results show a simplified model with 1 unit of strip sliding over 3 units of strip. (a)-(e) show critical positions inducing potential distributions..

2.3.3 Simulation Results on Open-Circuit Voltage

Employing a finite-element method (FEM) technique conducted by COMSOL, a computer simulation of the open-circuit voltage (V_{OC}) as a function of displacement was received and shown in Figure 2.10, 2.11. The largest voltage between the IE and the OE appears when copper strips on contact surfaces are in complete alignment (Figures 2.10a, c & e). Due to the mobility of electrons on copper, a small mismatch from aligned position would result in severe charge redistribution, resulting in a sharp shaped V_{OC} curve. The signal shows cycles with consistent amplitude as a result of the periodic displayed charges presented on grating patterns.

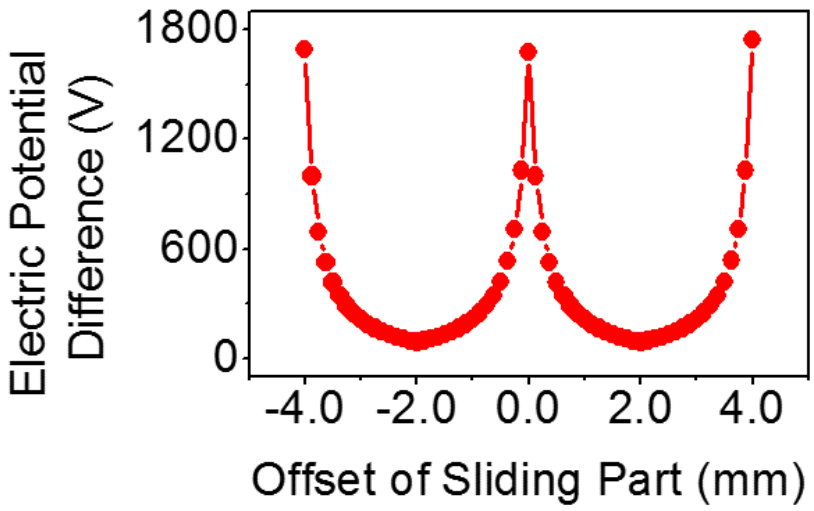

Figure 2. 11 Simulation results show electric potential difference between the IE and the OE during sliding under open circuit condition.

2.3.4 Simulation Study on Influence Caused by Fabrication Mismatch

Even though the FEM simulation was using dimensions from real model, it showed a voltage output significantly higher than the actual output (see chapter 2.4.2). FEM simulation was based on the assumption that each Kapton layer had the front and back grating electrodes aligned sharply with the 1/2 space phase difference, and had the exact 2 mm width on each strip. However, errors exist possibly in every step of fabrication that may results in certain overlap between electrode strips on the two sides of Kapton films (Figure 2.12). This section presents that even a 10% width overlap may significantly drop the output to more than 50%.

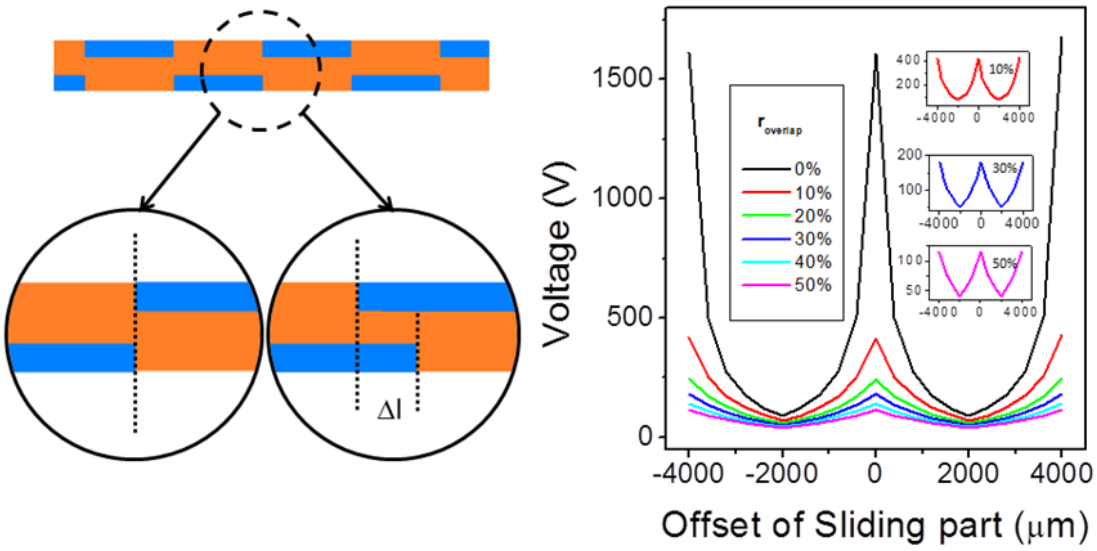

Figure 2. 12 Electrode overlap and its influence on open-circuit voltage

Studies of the influence on open circuit voltage by alignment errors are shown in Figure 2.12. If for fabrication limitation the outer electrode has a wider area, which means there will be an overlap Δl between outer and inner electrode, we define a rate $r_{overlap}$.

$$r_{overlap} = \frac{\Delta l}{Electrode\ Width} \tag{2.1}$$

By keeping all other parameters the same, the simulation for $r_{overlap}$ ranges from 0 to 50% was conducted, showing a significant reduce of output voltage from 1600 V to 115 V. The overlap leads to an accumulation of mobile charges in these areas to form a lowest potential instead of transferring between electrodes. Accordingly, shape of the output curve gradually changes toward linearly up and down (when $r_{overlap} = 50\%$) instead of the needle-like peaks caused by sharp increasing (when $r_{overlap} = 0$).

2.3.5 Simulation Results on Charge Transfer

By directly connecting the IE and the OE, the FEM simulation also reveals the charge-transferring process between electrodes, as presented in Figure 2.13. Given the assumption that during motion, all the induced charges coming out from one set of electrodes will transfer to the other set without missing, to monitor either set of electrodes with amount of net charge will provide the overall flowing situation of induced charges. The amount of net charges on one electrode exhibit a fluctuant curve with respect to displacement, composited by individual triangle-shaped patterns.

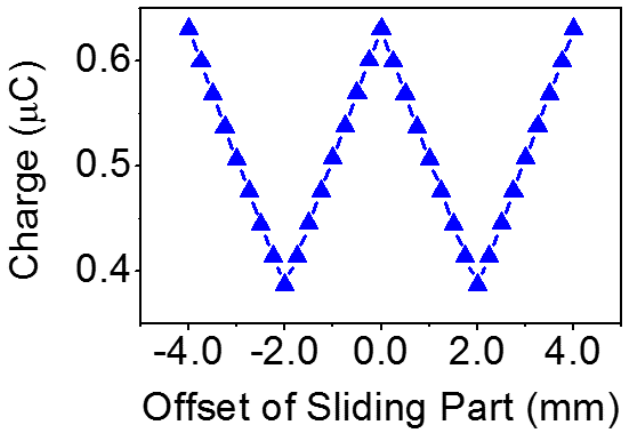

Figure 2. 13 Simulation results show charge from one electrode transferred out and in during sliding under short circuit condition.

2.4 Electric Output of the Case-Encapsulated TENG

2.4.1 Electric Measurement Setup

To characterize the Electric output of the cTENG, the as-fabricated device was connected with linear motor system and electric measurement equipment. The inner tube was connected to a programmable linear motor that was able to conduct velocity-controlled reciprocating motion. During the test, the linear motor was set to drive the inner tube sliding back and forth at various constant velocity. The outer tube, on the other hand,

was fixed, so that the two tubes could move relatively. The IE and the OE were then connected to measurement systems for voltage and current monitor. Data was transmitted to computer and collected by Labview® software.

2.4.2 Experimental Open-Circuit Voltage and Short-Circuit Charge Transfer

The experimentally open-circuit voltage V_{OC} was measured under constant driving velocity toward one direction producing a typical curve presented in Figure 2.14. The signal clearly reflect the electrification surface and the electrodes having a periodic pattern. As sliding velocity $v_{sliding}$ is constant, the *x*-axis which is time could be changed into displacement by multiplying factor $v_{sliding}$ without modifying the shape of the curve. Therefore, the experimental curve in Figure 2.14 can be directly abstracted to compare with the one in Figure 2.11. The experimental signal has a resembling but slightly different pattern compared to the simulated value. This is probably due to minor off-alignment during fabrication and measurement, which is discussed in chapter 2.3.4.

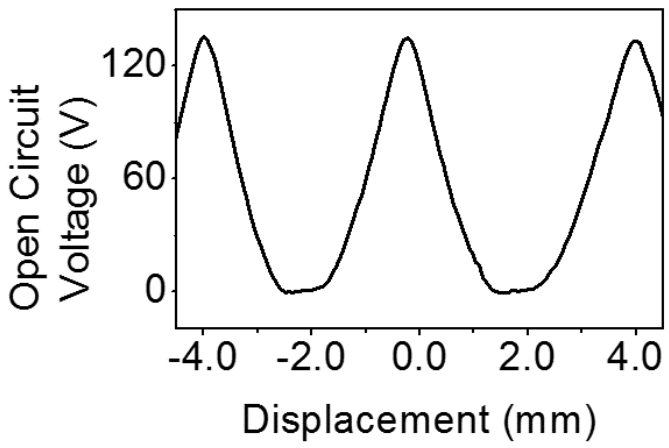

Figure 2. 14 Measured electric potential difference between IE and OE over time under open-circuit condition.

To measure the charge transfer, the short-circuit current (I_{SC}) over time was first measured during one slide (Figure 2.15). By integrating the current over a certain period of time ($t_1 \sim t_2$) in the middle, we receive the charge (Q) transfer behaviour over time. Again, the $v_{sliding}$ is introduced to transmit the *x*-axis from time (t) to displacement.

$$\mathrm{Q}(t) = \int_{t_1}^{t_2} I_{sc} dt \tag{2.2}$$

$$ds = vdt \tag{2.3}$$

As a result, the experimental charge curve based on time-integration shown in Figure 2.15 is in good agreement with the simulation graph (Figure 2.13).

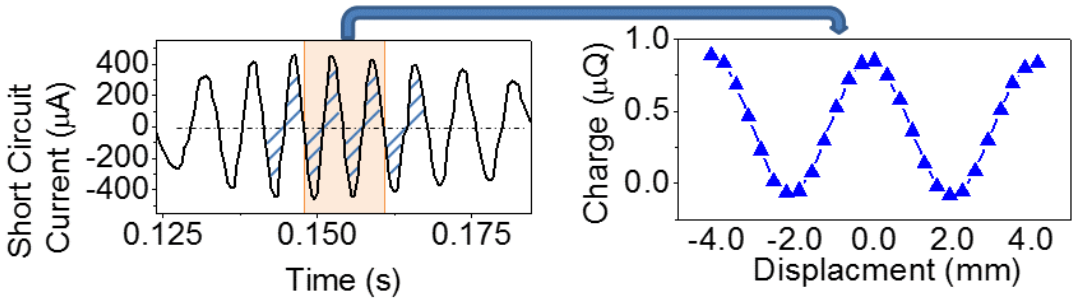

Figure 2. 15 Measured current curve between electrodes under short-circuit condition and partial charge curve integrated from measured current data.

2.4.3 Characteristics of the Electric Output

To characterize the electric output of the cTENG, I_{SC} and V_{OC} were measured at different sliding velocities. Reciprocating motions were continuously introduced by linear motor, which operated at a stroke of 35 mm. Velocities were programed from 0.3 m/s to 1.0 m/s, with an increment of 0.1 m/s. Accelerations were set at relatively high values to ensure sliding at a uniform velocity within most of the stroke. As shown in Figure 2.16a,

the amplitude of the I_{SC} rises with increasing sliding velocities. Statistical values plotted in Figure 2.16b exhibit a linear relationship between the current amplitude and the sliding velocities. The maximum value of 668 μA is achieved at a sliding velocity of 1.0 m/s. Such linearity is anticipated because the larger velocity shortens the time (time = l/v, where l refers to the sliding distance and v the velocity) of a single charge-transport process given that the amount of the transferrable induced charges between electrodes is constant. At the same time, the frequency of the output current is also linearly enhanced.

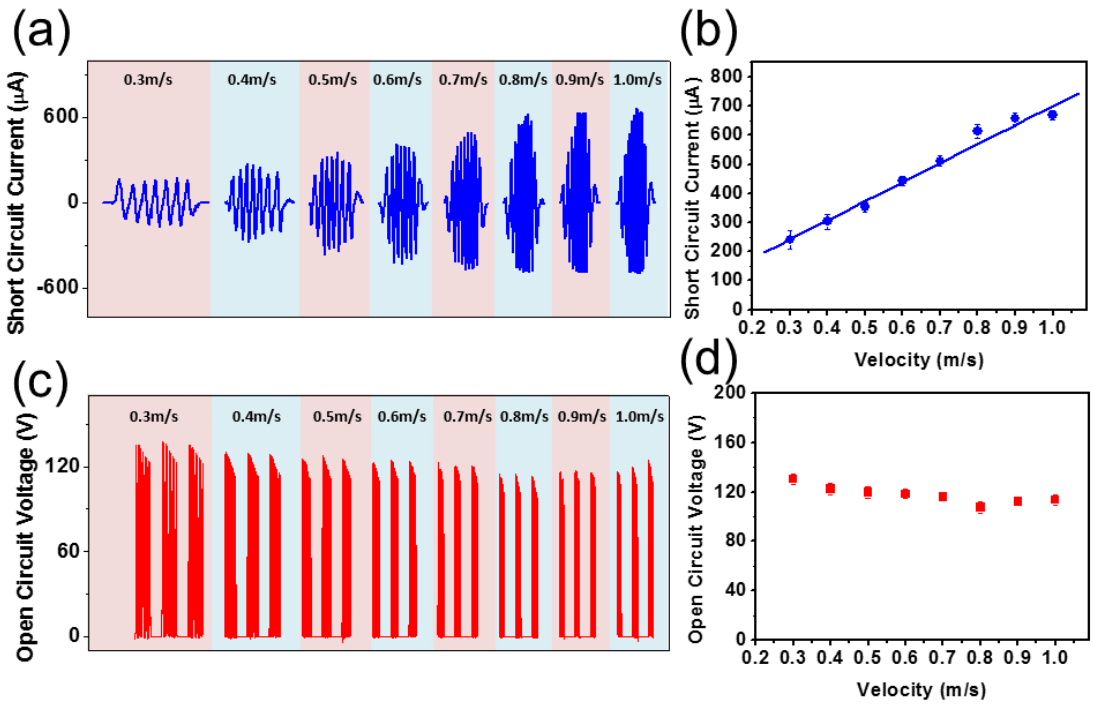

Figure 2. 16 Current and voltage output characters. (a) Short circuit current over different sliding velocities. (b) Current peak values show linear relationship over sliding velocity. (c) Open circuit voltage over different sliding velocities. (d) Voltage peak values do not change much over sliding velocity.

On the other hand, the V_{OC} does not have an apparent dependence on the sliding velocity, as shown in Figures 2.16c, d. In Figure 2.16c, the V_{OC} densely switched between zero and maximum values, which corresponds to fully aligned and fully displaced positions,

staggered. The maximum values (Figure 2.16d) only show a minor fluctuation of 110 – 130 V with a deviation of less than ±8.3%. This is because the V_{OC} is a function of displacement/position instead of the sliding velocity, which is revealed in the simulation results given in Figure 2.10 and 2.11.

For further characterization, accumulative induced charges delivered by the cTENG were measured using a bridge rectifier (inset in Figure 2.17). A series of load resistors were utilized for output power measurement. A typical curve of the accumulated charges at a load resistance of 200 kΩ is presented in Figure 2.17. Each step represents the total amount of output charges generated within a single stroke of sliding at a 1.0 m/s velocity. Consequently, the equivalent current (I_{eq}) in each stroke can be derived by fitting out the slope of a corresponding rising step (see red lines in Figure 2.17).

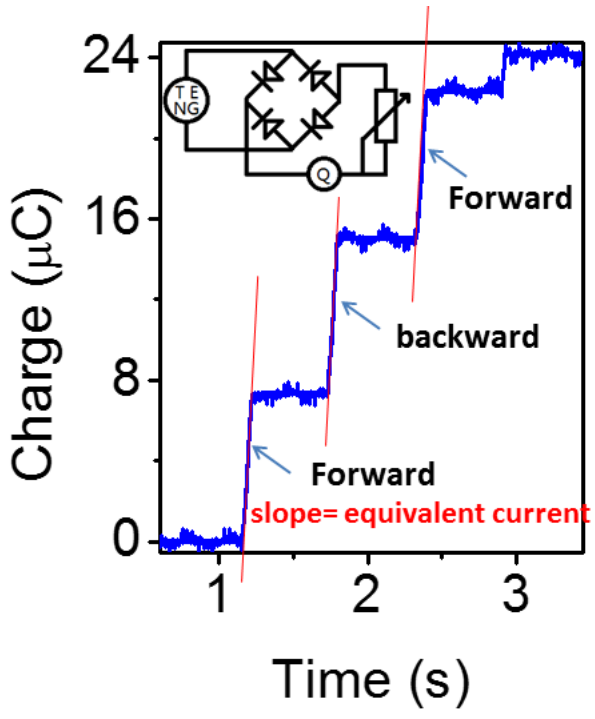

Figure 2. 17 Measured charge transferred between IE and OE over external load 200 kΩ after rectification at sliding velocity 1 m/s. Slopes of the curve indicate equivalent current. Inset diagram shows the cTENG connected with rectifying circuit.

With different values of load resistance, the equivalent current varies as shown in Figure 2.18a, in which larger load corresponds to lower equivalent current. The obtained equivalent current can be further used to calculate average output power (P_{eq}), which is equivalent to the Joule heating of the external load and thus, is defined as,

$$P_{eq} = I_{eq}^2 \times R_{load} \tag{2.4}$$

Figure 2.18b reveals the output power as a function of the external load, which reaches a maximum value of 12.2 mW at a load of 140 kΩ, in corresponding to a power density of 1.36 W/m^2.

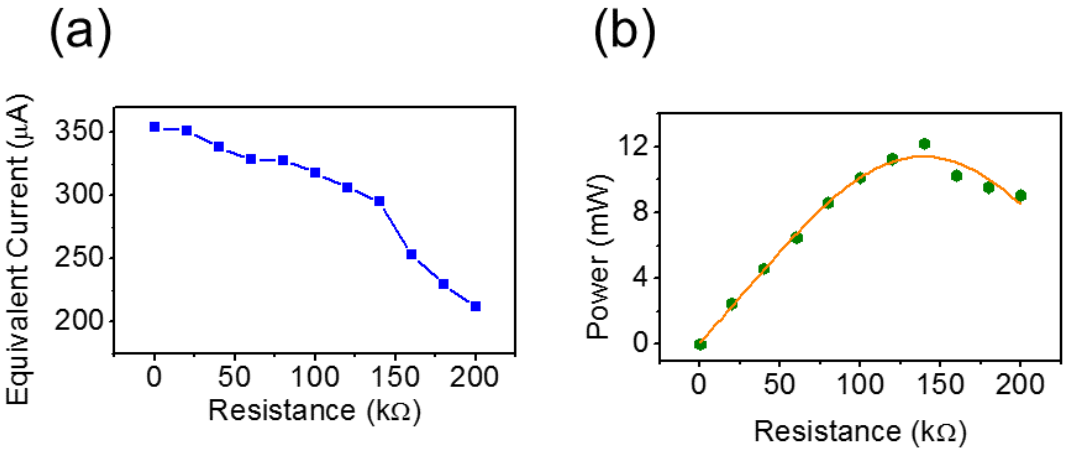

Figure 2. 18 Calculate equivalent current and average power from measured current curves. (a) Calculated equivalent current over different external load. (b) Calculated average power over different external load. Peak value of 12.2mW appears at 140 kΩ.

Detailed shape of accumulated charge curve in one complete sliding via external load with span from 0-200 kΩ was organized into Figure 2.19, in which several distinctive features can be observed. The curves are composed with steps one after one, showing consistency with the grating patterned triboelectrification surface and electrodes. With larger external load, the curves end at lower charge levels. For each individual curve, the

starting few steps and ending few steps show a smaller slope than the middle ones, meaning they are at lower instantaneous velocity because of the acceleration and deceleration of the linear motor. (One of the signs is the levelled part of the steps from the first and last are longer than the others.) As the slope reflects equivalent current, it is optimal to apply the cTENG on long stroke and large acceleration motions.

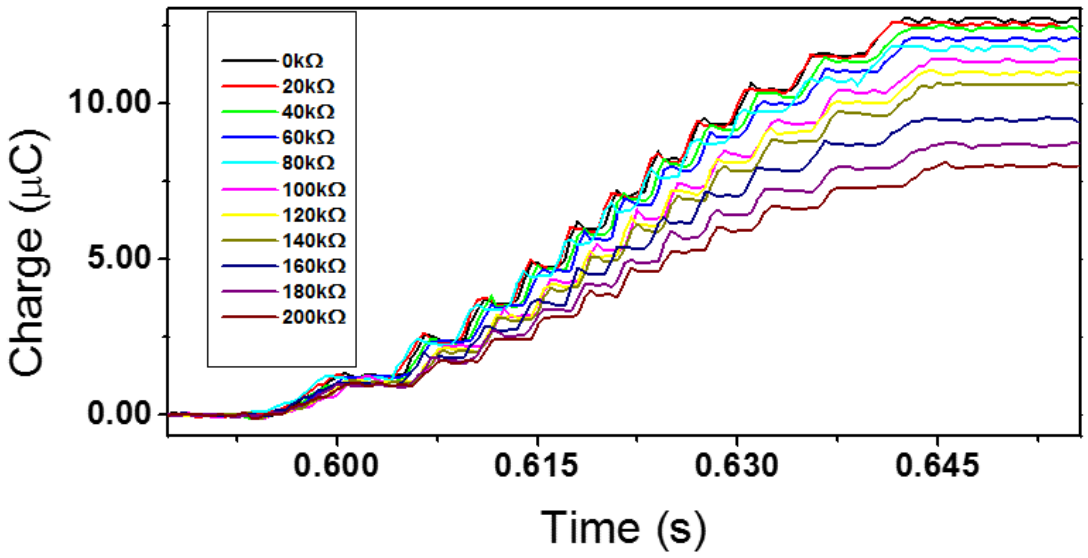

Figure 2. 19 Comparison of charge transfer over different external load. Curves are step-shaped due to grating electrode.

2.5 Effect of PTFE Nanoparticles

The PTFE nanoparticle was spread between the contact surfaces, to enhance the performance of cTENG (Figure 2.20). One of the most important purpose of inducing PTFE nanoparticle onto the surface of Kapton was to reduce friction, therefore increasing the energy transfer efficiency. A test on a plane platform using the as-fabricated layers was conducted. Driven by linear motor, one layer linearly slides over the other with a certain mass on the top to provide contacting force. Friction force was recorded both

before and after PTFE was applied (Figure 2.21a). Under pull condition, friction dropped approximately from 2.4 N to 1.9 N (dropped by 21%). For push condition, it dropped from 3 N to 2.1 N (dropped by 30%). Friction reduction ratio of nearly 1/3 was achieved, with the output of both voltage and current being influenced by less than 20% (Figure 2.21b). Especially the current output was very little influenced when the sliding velocity is small, meaning less work needed for the same amount of electricity produced at lower velocities.

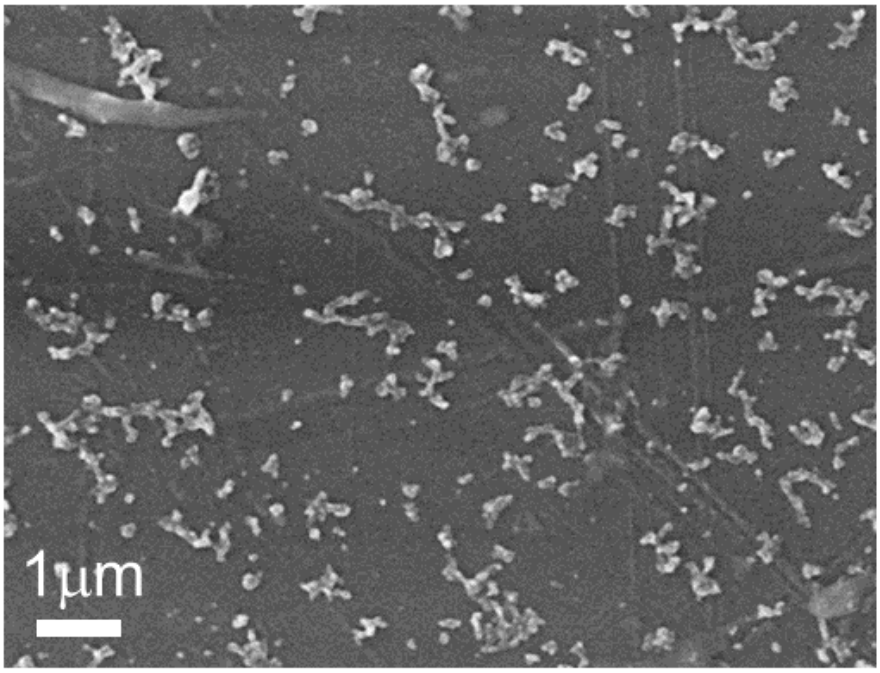

Figure 2. 20 An SEM image showing the PTFE nanoparticles being spread uniformly on the surface of Kapton film. Size of the particle is around 50-100 nm.

One may confused about the reduction of friction contributing to a reduction in the triboelectric output. At given contacting force, the friction force between two materials is mainly determined by surface roughness. However, the main reasons for triboelectrification are the properties of contact potential between two materials, as well as the contacting area during motion. Since the two are influenced by different surface condition, it is possible to reduce friction with the triboelectrification being hardly affected.

The PTFE on the surface of Kapton had both positive and negative influence on the output behavior of cTENG. For one hand, as PTFE is more negative in triboelectric series (Table 1.1), the presence of the particles on the Kapton is enhancing the triboelectrification process. On the other hand, overspread particles may occupy the surface of copper electrodes; consequently decreasing the effective working area of cTENG.

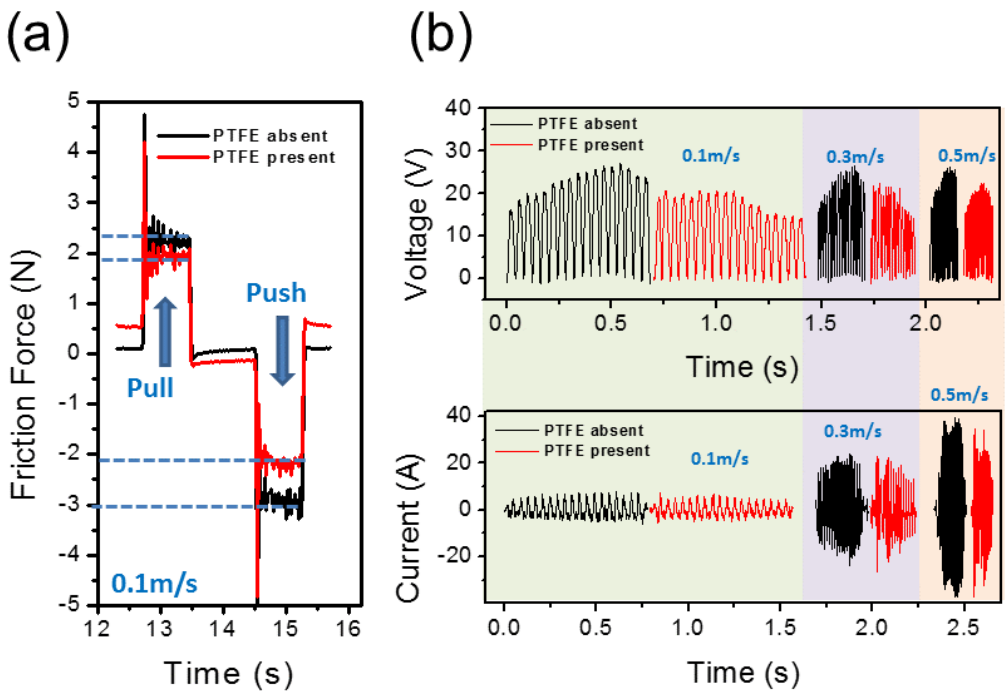

Figure 2. 21 Friction and output influenced by the presence of the PTFE nanoparticles. (a) Friction force measured with/without the presence of PTFE nanoparticles. (b) Voltage and current measured with/without the presence of PTFE nanoparticles at different sliding speeds.

The outputs presented in Figure 2.19b were smaller compared to those from cTENG because the scale and the contact force between surface were different, which may result a significant difference in electrical output.

2.6 Case-Encapsulated TENG as Working Models

To demonstrate the power-generating ability of cTENG, we apply the device to harvest energy from the wave motion of water and human motions. Reciprocating motions, including both periodical (vibration) and non-periodical forms, widely exist in daily life. Examples include but are not limited to engine cylinders, damping systems, human body motions, and water waves caused by wind, etc.

2.6.1 Case-Encapsulated TENG for Harvesting Wave Energy

In the first demonstration, cTENG was connected to a float and held vertically over the water surface (Figure 2.22a, b). When wave fronts passed over the float, the fluctuation of the water surface caused float to move up and down, triggering cTENG. Tens of green LEDs powered by the cTENG were lighted up (Figure 2.22c). Such a demonstration shows potential applications of the cTENG in water (lake/river/marine) navigation fields for self-powered buoy lights, channel lights, underwater obstructions warning lights, etc.

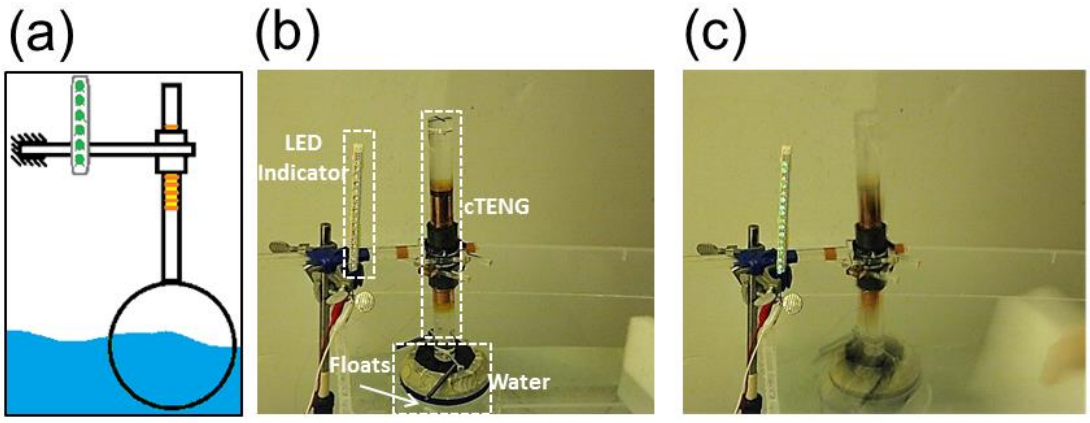

Figure 2. 22 cTENG in application of harvesting wave energy. (a) Schematic figure showing the setup of cTENG harvesting wave energy. (b) cTENG was connected to a float to harvest wave energy. (c) Green LEDs were lighted when artificial wave passed by the float which drove the cTENG conduct reciprocating motion.

2.6.2 Case-Encapsulated TENG for Harvesting Human Body Motion Energy.

The human body motion is another rich source of energy that can be harvested. By simply shaking cTENG, a series of parallel connected white bulbs were lighted up (Figures 2.23a-c). The cTENG can be further attached to certain parts of the human body, such as hand, forearm, leg or even the torso with its encapsulated casing designed in such a way to permit relative motion in order to generate electricity during human movements due to jogging, jumping, etc.

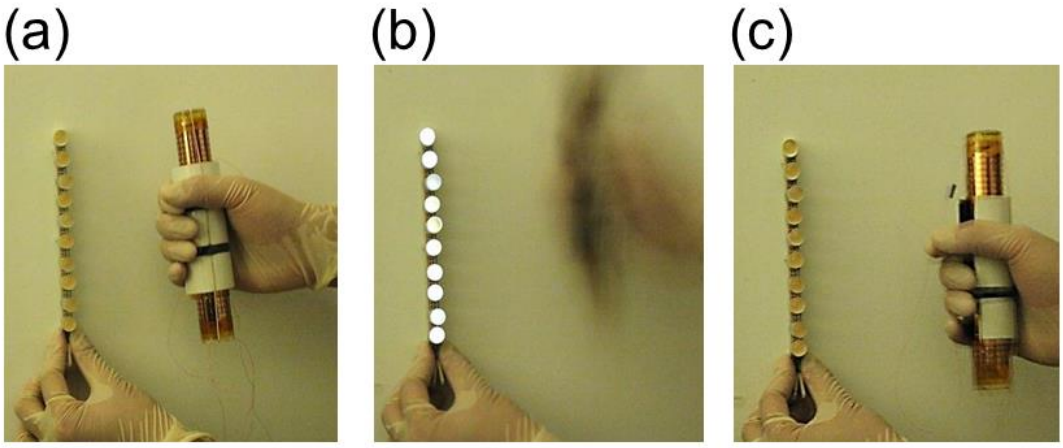

Figure 2. 23 cTENG tested in human body motion. White bulbs were driven off-on-off (a) before, (b) during and (c) after cTENG was shaken by hand.

2.7 Chapter Summary

As a summary for Chapter 2, we demonstrated a novel style of TENG with an encapsulated cylindrical case that not only delivers a high output but also, has several unique features. Grating designed Kapton/copper surface with PTFE particle lubricant ensures a high efficient output. An output current equivalent to a DC source of as high as 0.35 mA and an equivalent power 12.2 mW (corresponding power density 1.36 W/m2)

were achieved during a sliding velocity of 1.0 m/s. The output increases with increasing velocities. Simulations to explain the working mechanism were offered and detailed features of the charge transfer were studied using FEM. For demonstration, a float-connected cTENG generated enough power to light up multiple LED bulbs driven by energy of water waves. The cTENG was also applied to harvest energy from human body motion. Furthermore, the active signals measured in this experimental promise a further application as an active kinematic sensor that can operate without an external power supply. This topic will be addressed in the next chapter.

CHAPTER 3

SELF-POWERED TRIBOELECTRIC VELOCITY SENSOR FOR DUAL-MODE SENSING OF RECTIFIED LINEAR AND ROTARY MOTIONS

In Chapter 2 we demonstrated the use of the sliding TENG with patterned contact surface as an energy harvester for reciprocating motions. The output signal is distinctive with its characters reflecting the grating structure and thus, the grating pattern contains kinematic information about the motion and this makes it viable to monitor positions and velocities. That is, in addition to being employed as an energy harvester, cTENG can be used as an active velocity sensor.

3.1 Current Methods in Velocity Sensing

Velocity measurements are essential in many modern industrial applications in automation, transportation, robotics, etc. The well-developed methods for velocity measurements include technologies based on potentiometers,[60] magneto resistive sensing,[62,63] magnetic field sensors,[64] optical encoders,[65,67] capacitive sensing,[66] piezoelectric sensors,[70,71,91] etc. Most of these sensing technologies suffer from a shortcoming: they require a power supply to sense the mechanical motion. Such sensors can be classified as passive sensors because they cannot actively detect a change in the environment without being driven by electricity. Even for some active sensors that are designed to initially generate electrical signals,[70,71,91] the outputs are rather small and they need a sophisticated equipment for measurement, which may prohibit their applications to some extent.

Inspired by cTENG, we demonstrated a practical self-powered sensor for velocity measurements for either linear or rotary motion, called velocity-sensing triboelectric

generator (vsTEG).[92] Patterned with alternating Kapton-copper strips arranged in a 45° helix on both sides of the contact surface and packed in a case-encapsulated structure, the generator produced remarkably stable, macro-scale output signals for velocity measurements. What was further conducted was to successfully integrate the velocity sensor with a comparator-microcontroller unit (MCU) into a commercial digital circuit for the dual mode velocity sensing. The effort represents the first successful attempt in integrating a triboelectric with commercial MCU thus presenting a huge practical potential in the industrial commercialization of self-powered devices and sensors.

3.2 Design and Fabrication of a Linear/Rotary Dual-Mode Triboelectric Velocity Sensor

3.2.1 Structural Design of the Triboelectric Velocity Sensor

The schematic and actual structures of the vsTEG are shown respectively, in Figure 3.1a and b as consisting of a pair of coaxially-placed cylindrical tubes. The two tubes move relative to each other either in a rotational (Figure 3.1c) or sliding (Figure 3.1d) motion. To fabricate the interfaces, a polyimide film (Kapton®) was chosen not only as a durable supporting substrate but even more importantly, as a high-performance electrification material (the reason is described in chapter 2) for generating the triboelectric charges during the sliding motion with the electrodes. On either side of the Kapton film, copper strips are deposited with a linear pitch of 8 mm as electrodes as well as the other layer of electrification material. Hence, the electrode strips on the 2 sides form a linear shift of half a pitch giving rise to an alternating pattern with one another (Figure 3.3). The Kapton film wrapped over the acrylic cylinder possess its strip direction at a 45° screw-angle with the cylinder axis (Figure 3.1 and 3.3). A second Kapton film with the same electrode pattern is encased in the foam sleeve. The cylinder is then set in the foam case so that the two

layers of such fabricated Kapton film are brought into contact, forming a contact surface. The structure is then ready for producing the relative motion.

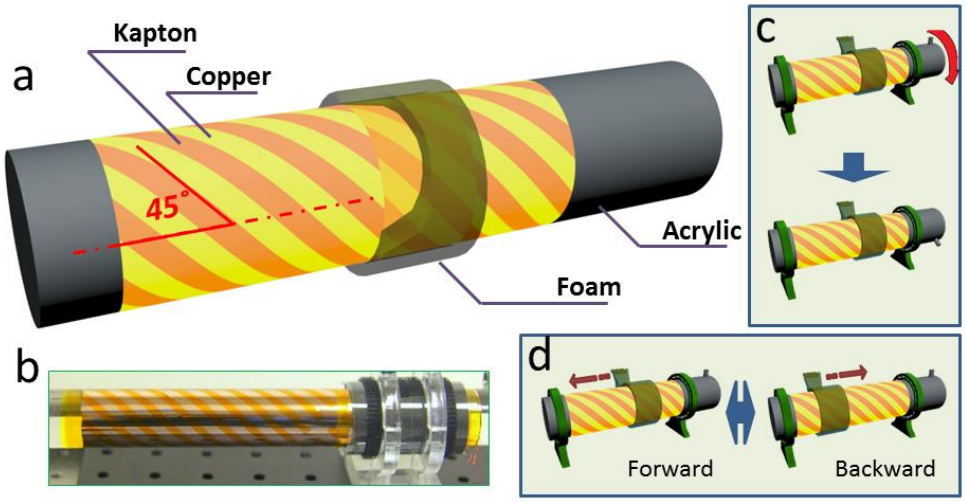

Figure 3. 1 Rotary and linear operations of the vsTEG. Schematic (a) and actual (b) structure of the vsTEG for rotary (c) or linear reciprocating (d) motion.

Electrodes located on each individual surface of the film are connected together via bus electrodes (Figure 3.3). To composite the electrode sets, an inner electrode (*IE*) is formed by stringing together the copper strips at the 2 contact surfaces via electrical wires (Figure 3.2); likewise, an outer electrode (*OE*) is formed by those on the other side of the Kapton film. The output signal is read from the voltage over load R in the connected *IE* and *OE*.

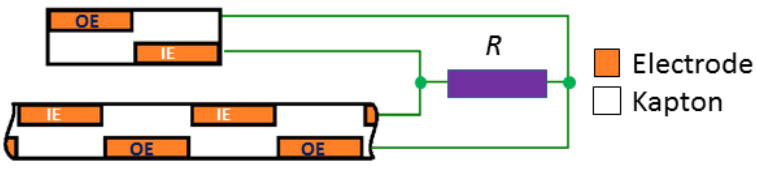

Figure 3. 2 Electrodes between contacting surfaces are linked as inner electrodes (IE), while the rest as outer electrodes (OE).

3.2.2 Fabrication Method of the Triboelectric Velocity Sensor

Two rectangular pieces of Kapton film (25 μm thick) were prepared with size 12 cm × 15 cm and 12 cm × 5 cm, with surface cleaned with isopropyl alcohol. Two firm Acrylic boards (1.5 mm thick) with corresponding sizes were laser-cut with hollow strips. These pierced boards were used as masks for the electrode deposition. Hollow strips with individual width of 4 mm and arranged at 45° to the edge in a linear pitch of 8 mm and spread over the available area of two boards but with the un-hollow areas kept connected. The column across all the strips was also engraved to ensure a deposition of the bus electrode that is connected to all strip electrodes on one surface. Kapton films were covered with corresponding-sized acrylic mask on one side and were conducted with copper electrode deposition by physical vapor deposition (PVD). Then, the same masks were used for the other surface of the pre-treated Kapton film with a linear shift of 4 mm before being conducted with a second copper deposition. The sample film after treatment is shown in Figure 3.3.

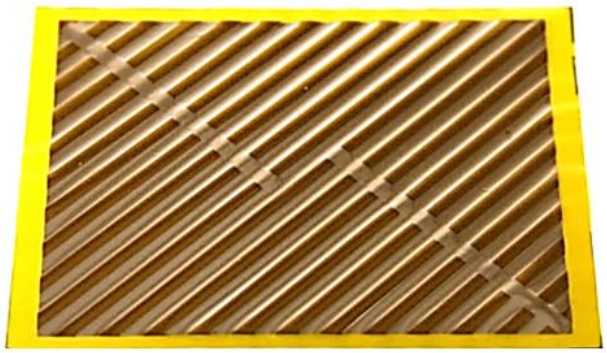

Figure 3. 3 Sample film after treated and ready to use. Electrodes deposited on one surface of the Kapton film are linked.

Coated with thin layer of Polydimethylsiloxane (PDMS) on the surface, acrylic cylinder rod with length 30 cm and diameter 2.54 cm was then wrapped with pre-treated Kapton film (larger one) as inner part. The other pre-treated Kapton film (smaller one) was then wrapped over and followed by another layer of 0.3 cm thickness foam tape. Polyethylene terephthalate (PET) film with 75μm thickness was finally applied onto the outer surface of foam tape as a support material. In the manner of either reciprocating form or rotating form, the outer part was able to move smoothly along the inner part.

3.3 Mechanism and Simulation of the Triboelectric Velocity Sensor

We suppose the similar mechanism happens here in this model compared to the structure mentioned in Chapter 2. However, the simulation has to be expanded from 2-D to 3-D in order to fully prove the functionality of dual-directional velocity sensing. As a result, the displacement to different directions over the contacting surface were simulated.

3.3.1 Working Mechanism

The mechanism of the velocity sensing capability can be explained as coming from the induced triboelectric charge transfer between the interfaces and its subsequent lateral polarization as driven by the relative motion. The vsTEG begins to actively generate output signals for velocity sensing when relative linear or rotary motion between the two interfaces occurs. The electricity generation mechanism of the vsTEG is illustrated in Figure 3.4. The triboelectric charge transfer due to the Kapton and copper being brought into contact causes the electrons to be injected between the two dissimilar metals generating current flow between the *IE* and *OE* (see Figure 3.4a to e).

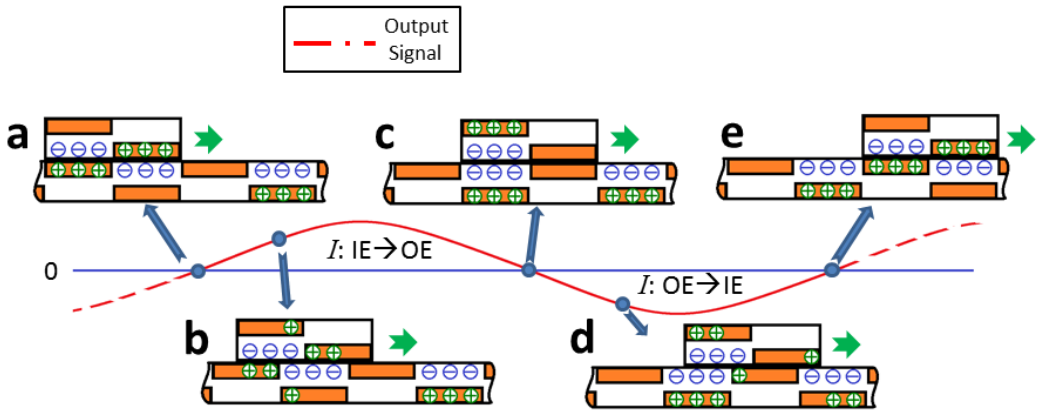

Figure 3. 4 Working mechanism of the vsTEG and simulation of its potential/charge distribution.

When the strip electrodes on the interface are in contact with the Kapton between the two layers (Figure 3.4a), all triboelectric charges are balanced and yielding no electric field. Once the sliding motion begins, charges on the mismatch area need to be compensated and therefore, induce a current flow from the *IE* to the *OE* (Figure 3.4b) until they reaching a fully-mismatched state shown in (Figure 3.4c). As the motion keeps moving on beyond this point, the back-flow of current occurs from the *OE* to the *IE* due to the requirement of the reversed charge compensation (Figure 3.4d). Both the motion and electric signal complete their cycles at the state shown in Figure 3.4e and return back to the starting cycle state in Figure 3.4a. Since the generated electric signal cycle stays consistently in sync with the driving mechanical (or motion) cycle, the retrieved velocity information is both stable and reliable.

3.3.2 Simulation Analysis for Velocity Measurement

The electric signals generated by the triboelectric charge transfer due to the dynamic mismatch between the strips exist as long as there is a component of the relative velocity

that is perpendicular to the strip direction. To further understand this mechanism, open-circuit voltages (V_{oc}), as well as, charge accumulations (Q_{ac}) under the short-circuit condition between the IE and the OE are studied via finite element simulations in a 2-dimentional space.

The Comsol Multiphysics® 4.2 and Matlab® 2009 software were used to simulate and present the finite element analysis results. An estimated charge density of -20 μC/m^2 was pre-applied on to the surface of Kapton interface[29] for the triboelectrification charges. The relative permittivity of Kapton was set equal to 3.4. The potential charge values were first simulated using "Comsol" at 289 (17×17) different spots and then, extended to a 3-dimentional surface using interpolation method provided in Matlab.

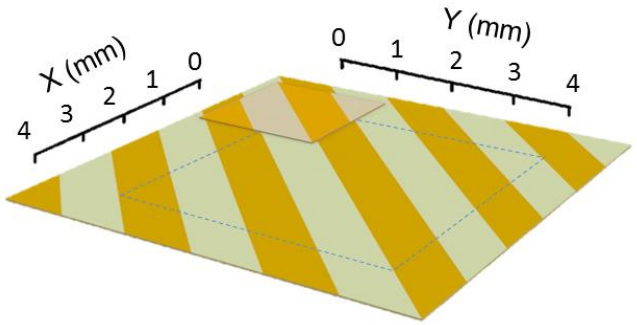

Figure 3. 5 Simulation model simplified as a piece of film sliding over a larger piece of film within an active 4 mm × 4 mm area.

The V_{oc} and Q_{ac} are assumed to be functions of spatial positions and are calculated by placing a smaller layer of the treated Kapton film over a larger layer at different positions (Figure 3.5) with the strip direction forming a 45° angle to both the *x*- and *y*-axes.

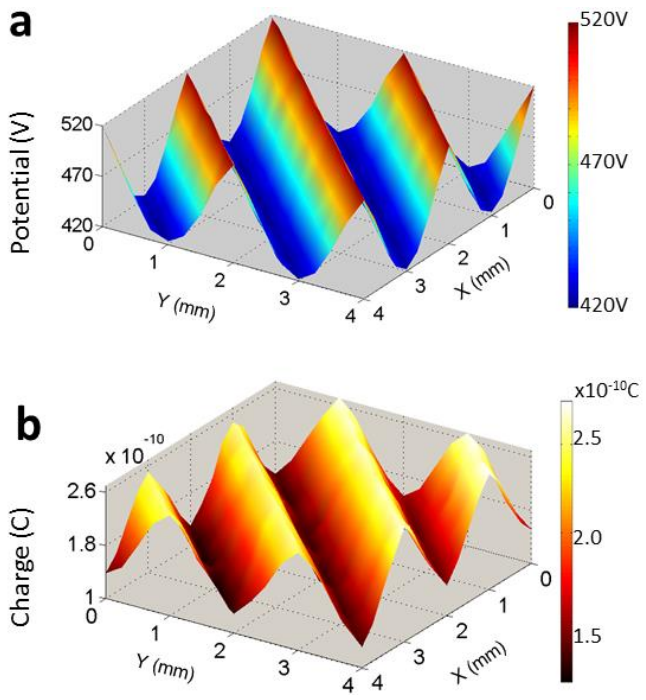

Figure 3. 6 Simulation result presented in plane. (a) Simulated potential difference (V_{oc}) between IE and OE for varying positions of the smaller film. (b) Simulated charge transfer between IE and OE.

Both V_{oc} and Q_{ac} showed a "wavy" shape distribution that is consistent with the structural variation of the strips (Figure 3.6a and b). FEM simulations confirmed that a relative motion with a velocity component that is perpendicular to the 45° direction generates a periodic output. Denoting θ as the angle between the direction of motion and the *x*-axis (Fig. 3.7a), the cycle time of V_{oc}, T can be obtained from:

$$T = \frac{w_{pitch}}{v_{sliding} \cdot \cos(45° - \theta)} \tag{3.1}$$

where w_{pitch} refers to the pitch distance and $v_{sliding}$ to the sliding velocity along the given θ direction. Output signal variations that correspond to θ ($0 \leq \theta \leq 90°$) for our dual-functional vsTEG design with the inner cylinder moving either linearly with $\theta = 90°$ or in a rotary motion with $\theta = 0°$, as well as, values in-between were studied. Among the serials of figures shown with θ from $0°$ to $90°$, V_{oc} contains 2 complete cycles at $\theta = 0°$

(Figure 3.7b) and $90°$ (Figure 3.7h), respectively. As θ increases from $0°$ to $45°$, V_{oc} enlarges its cycle until it reaches almost a constant value at $\theta = 45°$ (Figure 3.7e). The status of $\theta = 45°$ demonstrated that motion merely contains vector component along the strip direction will not generate alternative signal. As θ increases continuously, the cycle is shortened and restores identically to $\theta = 0°$ when θ reaches $90°$.

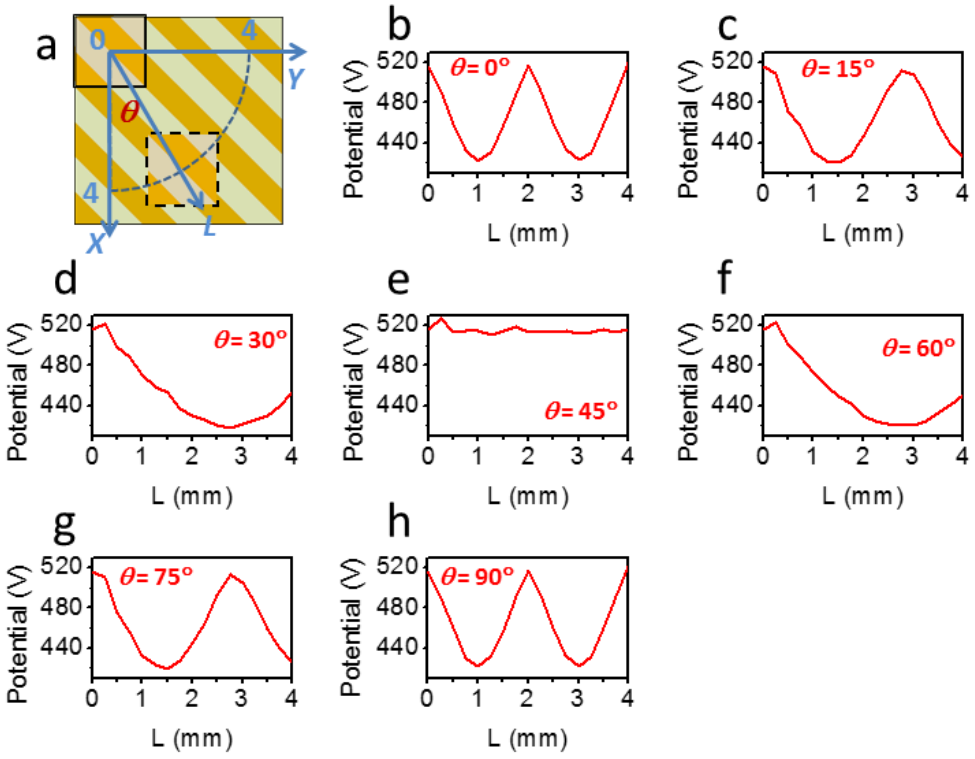

Figure 3. 7 Output signal simulation under different sliding directions. (a) Sliding angle ϑ is denoted as the angle between the direction of motion and the *x*-axis. (b-h) Output signal simulated under serial values of ϑ.

3.4 Electric Output of a Triboelectric Velocity Sensor

Given the signal behavior on rotatory ($\theta = 0°$) and linear ($\theta = 90°$) motion are similar, the electric output characterization can be conducted from either of these two situations.

As linear reciprocating motion was described in chapter 2, herein the electric output was measured under rotatory condition.

Two metal bearings were mounted at each end of the cylinder to permit the necessary rotating motion to occur. They also performed as a channel for conducting signals generated by the moving electrodes. The cylindrical and foam tape parts were then separately fixed to different supporters so that they can generate relative motions. To let the cylinder rotate, a transition kit using timing belt and belt pulleys was installed between the cylinder and a rotary motor with foam tape part being static (Figure 3.8a, b). Also, with this setup the cylindrical part could also generate linear motions relative to the foam part by removing the timing belt and attaching the cylinder to a linear motor.

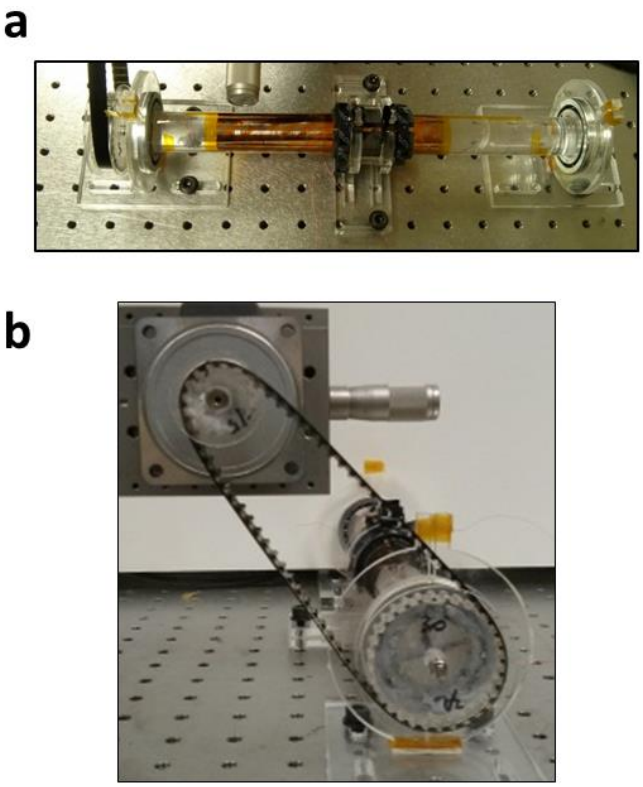

Figure 3. 8 Set up for rotation measurement. (a) The cylinder is mounted with bearing on the two ends. (b) Rotation is driven by timing belt at reduction ratio 1:2.

3.4.1 Output Voltage over Different Velocities and External Circuit Loads

To characterize the performance of the vsTEG, the relationships among velocity, output voltage and external circuit load are studied (Figure 3.9). As mentioned above, a rotary vsTEG is installed by having the two ends of the inner cylinder firmly collared with bearings and rotationally driven by a motor with a 1:2 reduction ratio (Figure 3.8b). The outer foam tape cylinder is firmly clamped to ensure there is relative motion between the 2 coaxial cylinders. The external circuit load is adjusted by suitably tuning the load resistance. Voltage signals (V_r) are measured for varying velocities from 100 - 500 rpm and representative curves are plotted and categorized in Figure 3.9.

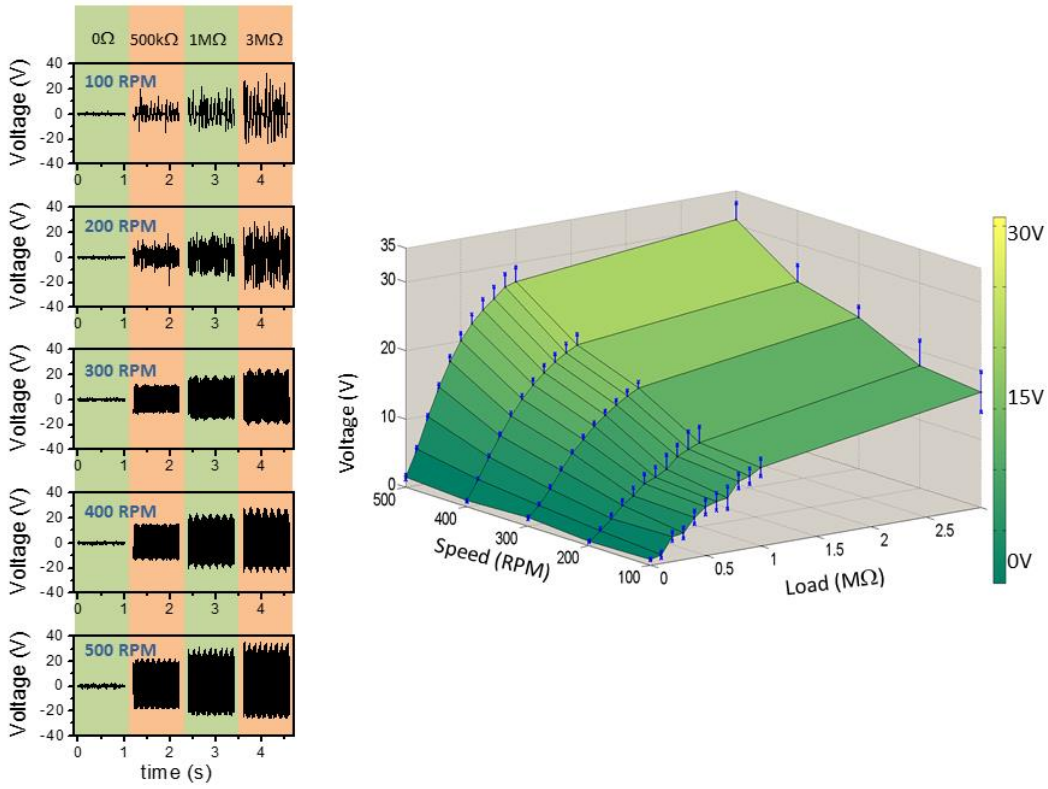

Figure 3. 9 Output characteristics for changing velocities and external loads. The vsTEG output voltage as a function of varying rotational velocity from 100–500 RPM and varying external load from 0–3 MΩ. 3D plot categorized the result by presenting relationship among the maximum output (with error bar), velocity and load.

As shown, for a given rotational velocity, the V_r peak value increases with increasing load resistance. Similarly, for a given load resistance, the V_r peak value and intensity increase with increasing rotational velocity. For better clarity, a 3-D V_r peak value plot is sketched in Figure. 3.9, with the velocity and load forming the 2 horizontal axes. At lower velocities and smaller loads, the V_r peaks are relatively small and difficult to distinguish from the background noise. As the load (or velocity) increases, the surface of V_r peaks approaches a relatively flat area, which is approaching an open circuit condition.

3.4.2 Signal Cycles Reflecting the Speed

To further examine the shape of the output signal, different V_r graphs obtained at the 3 MΩ load are partially plotted together for different rotational velocities in Figure 3.10. As shown, V_r peak values vary from 17-31 V and they become more intense with increasing rotational velocities. Cycle differences are clearly reflected and well corresponded to rotating speeds.

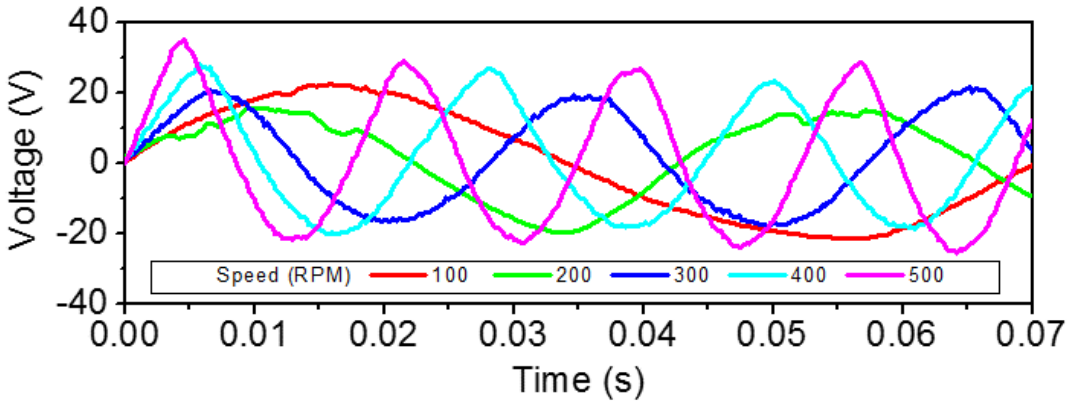

Figure 3. 10 Varying velocities generate varying signal cycle length (measured at the 3 MΩ load).

3.5 Signal Conversion and Processing

3.5.1 Signal Conversion

To extract the cycle information, a signal conversion technology is a prerequisite. Taking advantage from vsTEG's positive output signal, there is no need to power the velocity sensor itself in order to acquire the alternative voltage. The solution is then to convert the alternative signal into a transistor-transistor logic (TTL) signal which is a standard signal recognized by most of current commercial circuit and processors.

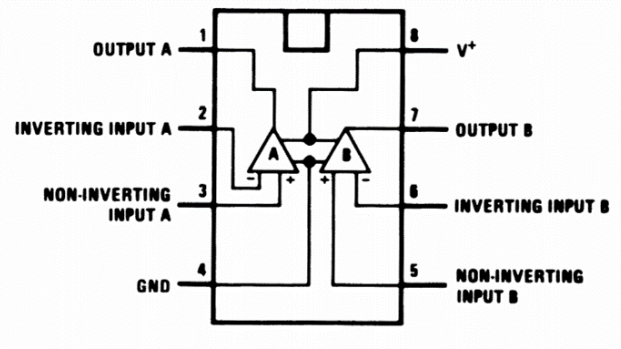

Figure 3. 11 Schematic diagram of LM393N. (http://www.ti.com/product/lm393-n)

A comparator (LM393N, Texas Instruments®, Figure 3.11) is applied to convert the output analog signal into the TTL signal. The LM393N has 2 sets of comparator integrated in a chip with each comparator containing 2 input pins (inverting and non-inverting input) and one output pin. The comparator provides the function of shifting its output level from logic high to logic low once the voltage level in inverting input exceeds the one in non-inverting input (details about LM393N are provided in table 3.1).

Table 3. 1 Features of LM393N. (http://www.ti.com/product/lm393-n)

Supply voltage (Min) (V)	**2**
Supply voltage (Max) (V)	36
Response time Low - to - High (us)	0.7
Offset Voltage @ 25˚C (Max) (mV)	5
Supply current per channel (Max) (mA)	0.5
Output Type	Open Collector Open Drain
Input Bias Current (+/-) (Max) (nA)	250
Number of Channels (#)	2
Operating Temperature Range (°C)	0 to 70

When it comes to converting the vsTEG's signal, several concerns on the reference voltage must be considered and they include the reference level should be lower than the V_r peaks, the reference level should overcome the noise when the vsTEG is in the static state, and the converted TTL signal should be consistent with the original signal even if fluctuations at varying cycles are present. Once the reference level is higher than any of the V_r peaks that needed to be included for calculation, certain peaks will not be converted into TTL signal shift which will result in information missing. The reference level should be higher than the noise so that the comparator will not be triggered to shift its

output level when there is actually no effective V_r signal. Each time the vsTEG's signal cutting cross the zero voltage line, or reaches its positive/negative peaks, it reflects certain relative positions of the two film presented in Figure 3.4a, c, or e. Due to fabrication errors, the peak values may present fluctuation among each other, thus is difficult to cut out accurately by fixed reference voltage level. On the other hand, different velocity will also influence the V_r peaks, make it even impossible to pick out peak information by only applying comparator. As the last choice, the reference voltage level should be as near to zero as possible, so that TTL signal shifts its level every time the vsTEG's signal goes from negative to positive.

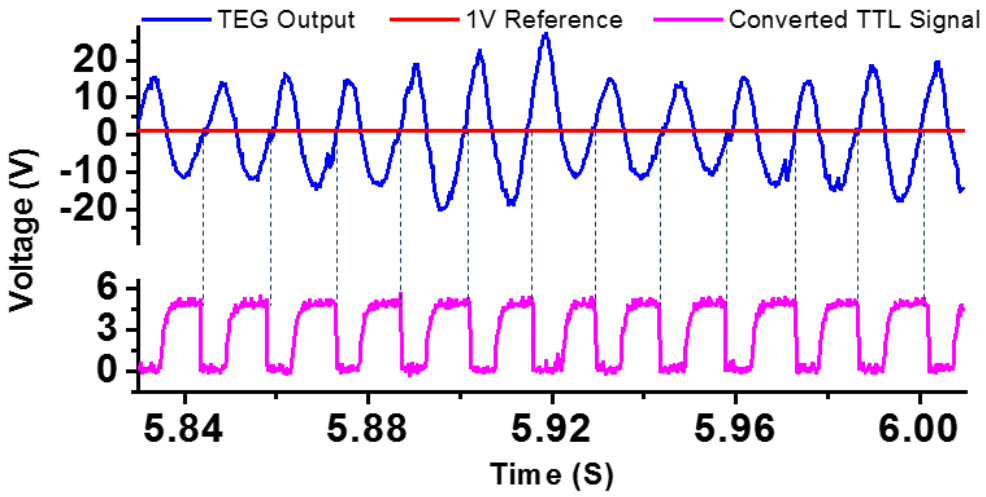

Figure 3. 12 The vsTEG rotating signal is converted into TTL signals.

A reference level of +1 V is chosen to meet all of the considerations for later tests. By applying reference voltage level on the non-inverting input pin, the vsTEG output signal is able to be instantaneously converted to TTL square wave with consistent timeline characters (Figure 3.12). By reading out each falling edge from the TTL signal while

maintaining the timing, the cycles are acquired and the velocities are calculated using Equation 3.1 by the MCU.

3.5.2 Circuit Diagram and Date Processing

A simplified circuit diagram is shown in Figure 3.13, in which the whole system is composed by a vsTEG as active signal generator, a comparator (LM393N) as signal converter, a microcontroller unit (STC®89C52RC) as computing/commend unit and a light-emitting diode (LED) digital displayer for result presenting.

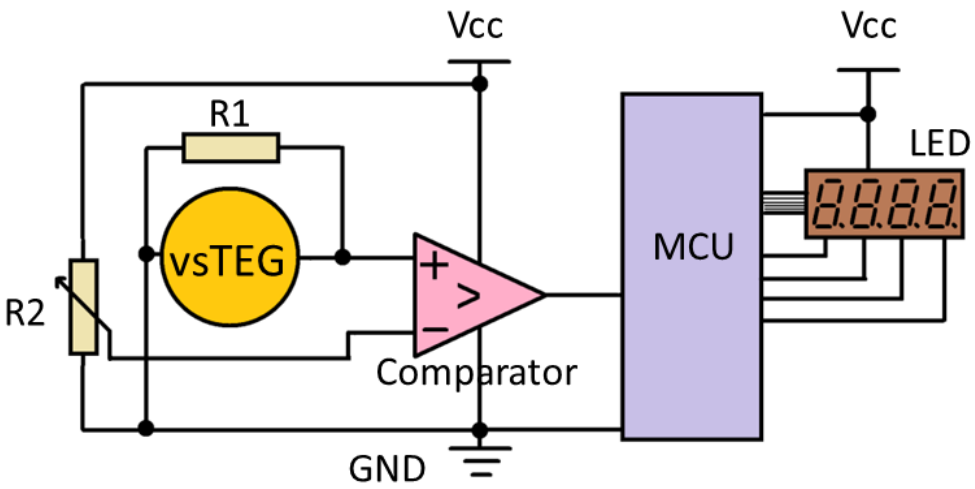

Figure 3. 13 Circuit diagram.

Raw signal is first generated by vsTEG which is carrying the important cycle information. One of the two output terminals of vsTEG is then connected to inverting input pin of comparator, with the other connected to the common ground. The comparator enjoys a reference level of +1 V provided by adjustable resistance R2. The output pin of the comparator is joined with common input/output pin of a microcontroller unit. The

microcontroller unit then conducts all the calculation and finally displays the results on LED digital displayer.

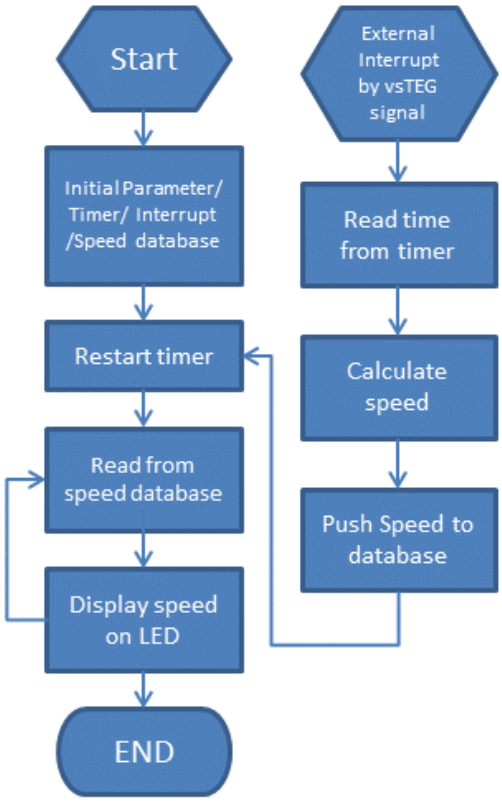

Figure 3. 14 Flow diagram.

Figure 3.14 is the flow diagram briefly illustrating MCU working principle. An interruption function is applied in the process to independently response to the falling edges from TTL signal while timer and result-display function are running parallel. Each time an interruption is triggered with interrupt-subroutine being called, local velocity is calculated utilizing values from timer and is later on pushed into velocity database for display. The main program starts with initiation of parameters, timers, interruptions and

velocity database, followed by start/restart timer process and then a loop for displaying velocity results. All steps can be fulfilled by a program using C language.

3.6 Dual-Mode Triboelectric Velocity Sensor in Measuring Rotatory and Linear Velocities

3.6.1 Rotatory Velocity Measurements

Rotatory velocities were then successfully measured based on the signal converting and processing solution described in Section 3.5, with the same set up mentioned in Chapter 3.4. A series of velocities are tested for the rotary motion connections (Figure 3.8) with the velocity varying from 125 - 700 rpm (corresponding to the driving motor velocity of 250 - 1400 rpm). The performance of the rotary vsTEG is recorded both in image sequences and in electrical data form (Figure 3.15). The right-side LED displays the motor speed and the left-side depicts the vsTEG speed. The data obtained and given in Figure 3.16 displayed a remarkable stability and accuracy with little divergence at each test point.

Table 3.2 summarizes the key results that include the “measured reduction ratio” calculated from the LED-read data, and errors for each of the tested point. Errors are defined as the deviation of reduction ratio to average of reduction ratio. They are described as the following expression.

$$r_n = \frac{v_n^{vsTEG}}{v_n^{motor}} \quad (\sim 0.5) \tag{3.2}$$

$$\mu = \frac{1}{n}\sum r_n \tag{3.3}$$

$$S = \sqrt{\frac{1}{n}\sum (r_n - \mu)^2} \tag{3.4}$$

$$e = \frac{S}{\mu} \tag{3.5}$$

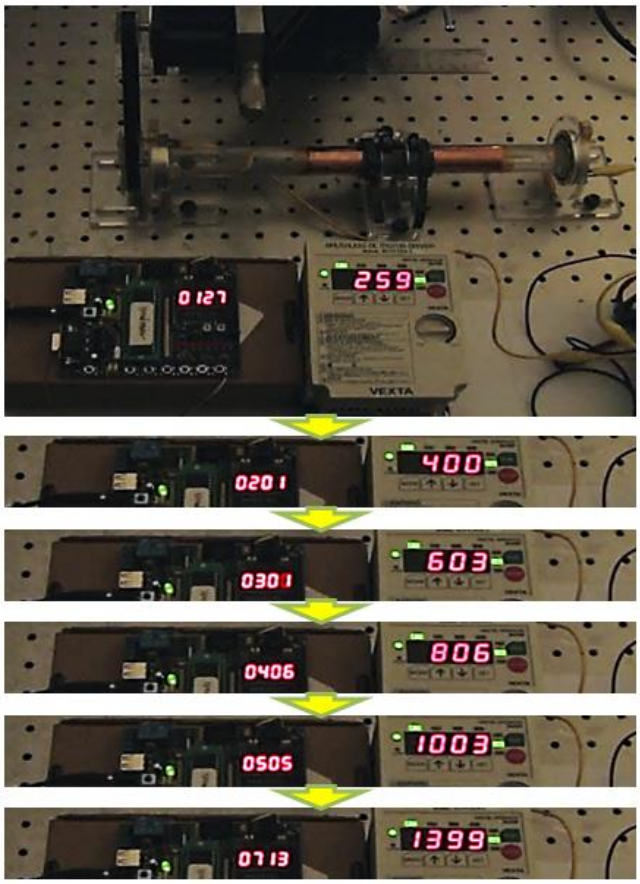

Figure 3. 15 The vsTEG tested for measuring rotary motion under 1:2 speed reduction. The right-side LED displays the motor speed and the left-side depicts the vsTEG speed.

Where v_n^{vsTEG} is the measured velocity by dual-mode velocity sensor and v_n^{motor} is the speed of driving motor. The error e reflects the fluctuation of measured velocity under a fixed driven velocity.

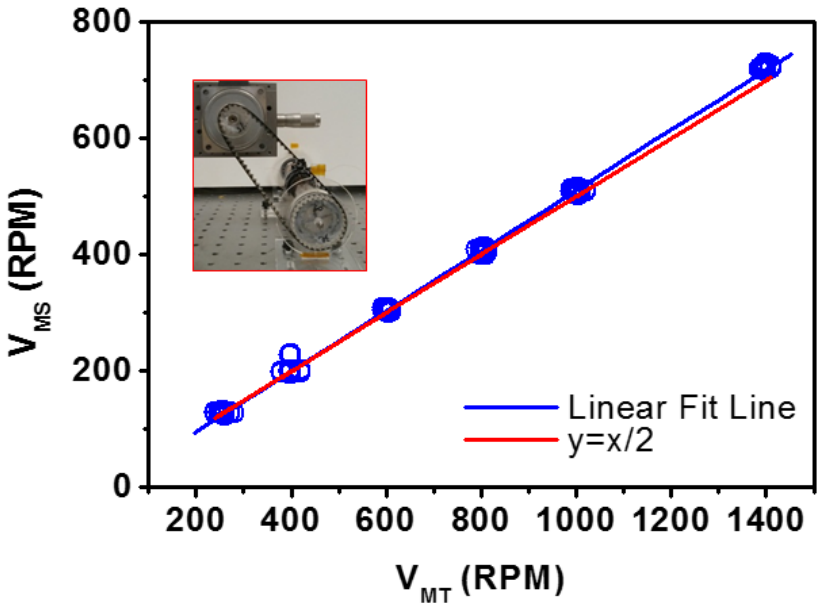

Figure 3. 16 Data collected for varying velocities showed stable and consistent correlations.

As the velocity increases, the reduction ratio exhibits a slightly increasing deviation from the 1:2 mechanical reduction ratio. We have discussed a possibility of the cause of the difference that may be attributed to the fabrication errors in Chapter 3.6.3.

Table 3. 2 Statistical results from rotary motion test.

Motor Speed (RPM)	≈250	≈400	≈600	≈800	≈1000	≈1400
Structural Reduction Ratio	1:2					
Measured Reduction Ration	0.5003	0.5070	0.5047	0.5056	0.5082	0.5157
Standard Error	4.23%	5.14%	0.83%	0.88%	0.86%	0.50%

3.6.2 Linear Velocity Measurements

Next, linear velocities are measured by changing a small bit of the setup. The linear vsTEG is characterized using a programmable reciprocating motor that conducts a linear motion. The outer foam cylinder is clamped in space and one end of the inner cylinder firmly attached to the linear motor to produce a relative linear-reciprocating motion between the 2 coaxial cylinders, see Figure 3.17.

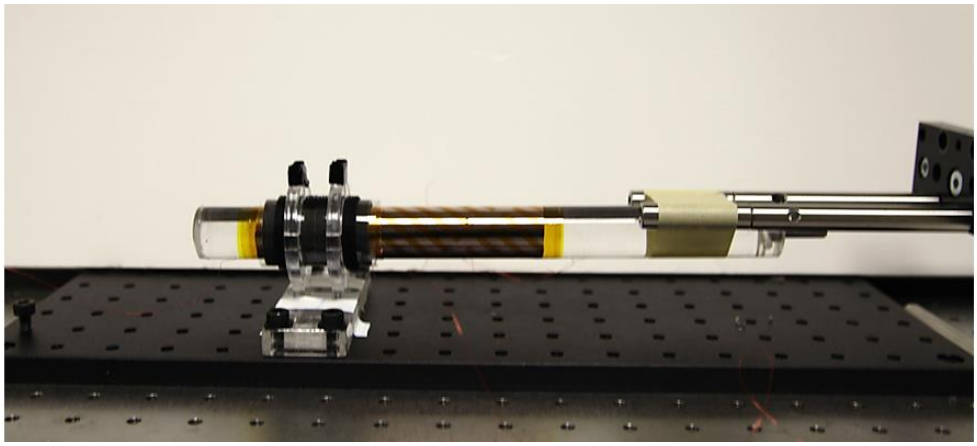

Figure 3. 17 Set up for linear velocity measurement.

The signal performance of the linear vsTEG for a set of reciprocating motion is recorded and shown in Figure 3.18, as well as, the corresponding converted TTL signal. In contrast with the continuous output signals generated by the rotary vsTEG (Figure 3.12), the linear vsTEG showed bands output signals corresponding to the forward and backward linear motions, as well as, intermittent stop motions. To minimize inaccuracies, motion that exhibits acceleration and deceleration are discarded; only the middle part of the converted TTL signals with a uniform cycle that best represents the pre-set velocity of the motor is used. The MCU is therefore, programmed accordingly and optimized for best results.

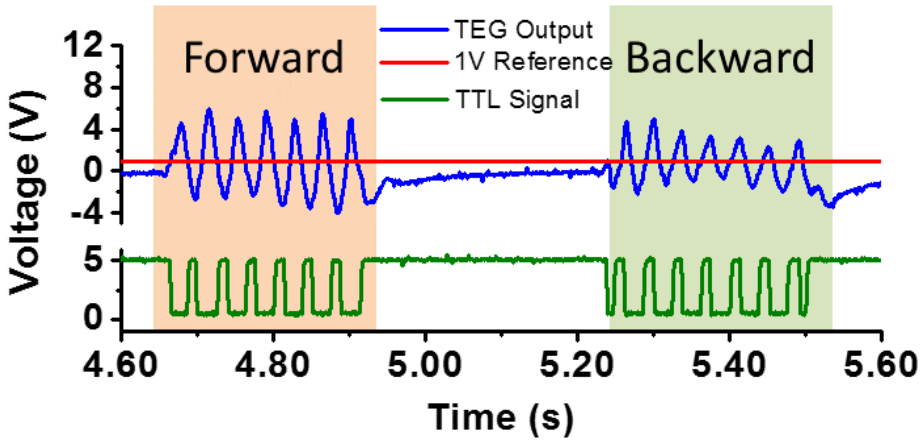

Figure 3. 18 Output signals are differentiated as forward and backward, with intermittent stop. All the fluctuations are caught and converted to TTL signal.

The forward and backward velocities are recorded and studied separately (Figure 3.19) with assistance from a video camera. As shown, the velocities obtained exhibit remarkable stability and accuracy for both forward and backward motions. As the test velocity increases, the linear vsTEG begins to display a slightly increased deviation from the motor velocity (Figure 3.19), which may be caused by the lag in the program. Also, the backward motion seems to possess a larger error than the forward motion, which may be attributed to the asymmetric driving condition of being pulled-pushed at only one end of the inner cylinder. However, for all the tested points, the linear vsTEG exhibited a standard error of less than 0.5%.

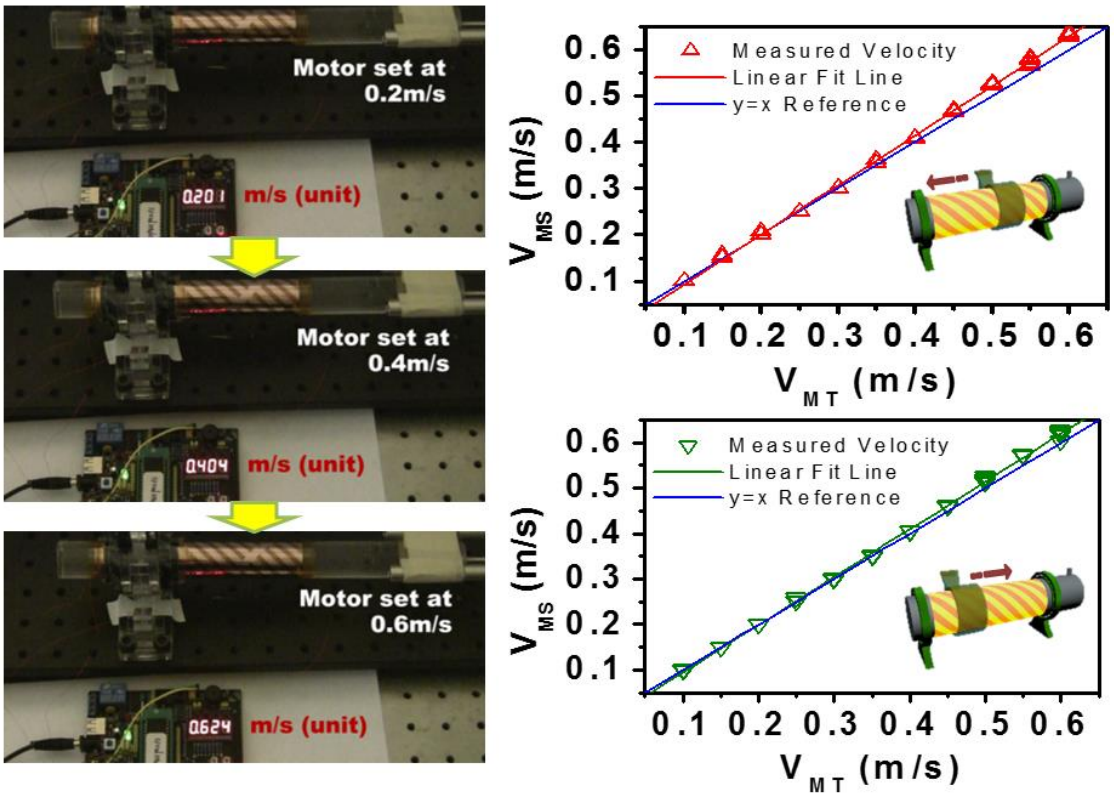

Figure 3. 19 The vsTEG being connected to a linear reciprocating motor and driven at varying linear speed from 0.1–0.6 ms^{-1} was recorded. Both forward and backward motion data collected at varying velocities showed good consistency.

Table 3.3 summarizes the key results that include the errors during either forward or backward test on different velocities. The results are calculated based also on LED-read data, with the help of video camera. In linear mode, errors are simply defined as the average deviation of data collected under each velocity.

Table 3. 3 Statistical results from linear motion test.

	Velocity (m/s)					
Motor	0.10	0.20	0.30	0.40	0.50	0.60
Forward Average	0.100	0.203	0.301	0.408	0.524	0.632
Forward Error	0.000%	0.242%	0.000%	0.030%	0.160%	0.169%
Backward Average	0.100	0.201	0.300	0.404	0.516	0.621
Backward Error	0.038%	0.020%	0.036%	0.058%	0.244%	0.498%

3.6.3 Rotatory Velocity Measurement Affected by Fabrication Errors

As the treatment and wrapping processes of the Kapton were separated, errors occur when aligning the strips during wrapping process, leaving a mismatch gap at the junction (Figure 3.20). When the outer layer for the rotary motion, the signal reverts to its original phase by $(\Delta s/w_{pitch}) \times 2\pi$ (where Δs is the mismatch width and s is the electrodes pitch width indicated Figure 3.20). Hence, the cycle length is affected and a modification of the calculated cycle length is required.

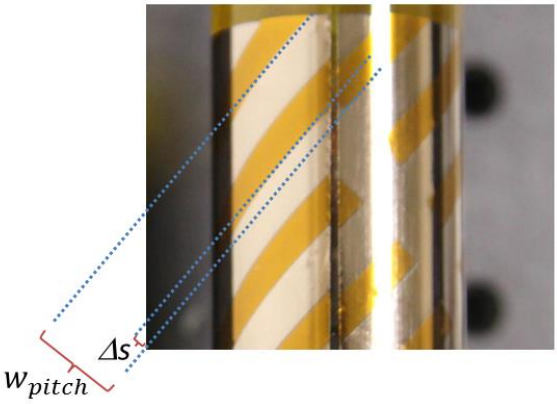

Figure 3. 20 Photograph showing the gap due to fabrication errors. Mismatching gap is marked as Δ*s*.

Assuming the output signal is sinusoidal, we choose as the first round for reference,

$$U_1 = A \cdot \sin(\frac{\theta \cdot R}{w_{pitch}/\cos 45^\circ} \times 2\pi) \tag{3.6}$$

where θ is rotating angle and R is the radius of the cylinder. If there is a phase shift, we get

$$U_2 = A \cdot \sin(\frac{\theta \cdot R}{w_{pitch}/\cos 45^\circ} \times 2\pi + \frac{\Delta s}{w_{pitch}} \times 2\pi) \tag{3.7}$$

Considering the rotating process from the beginning of the first loop to the beginning of the second loop as consisting of a linear decrement component U_1 and a linear increment component U_2, the output can be estimated as,

$$U = \left(1 - \frac{\theta}{2\pi}\right) \cdot U_1 + \frac{\theta}{2\pi} \cdot U_2 \tag{3.8}$$

Or,

$$U = \left(1 - \frac{\theta}{2\pi}\right) \cdot A \cdot \sin\left(\frac{2\pi \cdot \theta \cdot R}{w_{pitch}/\cos 45^\circ}\right) + \frac{\theta}{2\pi} \cdot A \cdot \sin(\frac{2\pi \cdot \theta \cdot R}{w_{pitch}/\cos 45^\circ} + \frac{2\pi \cdot \Delta s}{w_{pitch}}) \tag{3.9}$$

The influence is graphically shown in Figure 3.21. A superposition of the final signal with an error "$\Delta s/w_{pitch}$" equals to 0.2 and 0.4 are presented. The first and second line of each graph are signal of first loop and second loop described by Equation 3.6 and 3.7, respectively. The back ground triangle shows the proportion of the signal that is counted to form signals in the third line, which is the approximate actual signal in an error existing device. The arrow indicates a 7th zero crossing in superposition curve compared to the 1st Loop. Greater errors shorten the superposition curve cycle more significantly, and influence the amplitude of the curve as well. For one hand, the error may result in a fault cycle length that needs to be corrected by programming. For the other hand, the amplitude change may bring trouble in recognizing signal in the comparing process conducted by comparator. Usually the cycle shift can be fixed when $\Delta s/w_{pitch}$ is given, and the error could be eliminated by inserting a correction factor in processing program. The value may significantly increase if the w_{pitch} is relatively small. Thus, the width of the pitch need to be controlled.

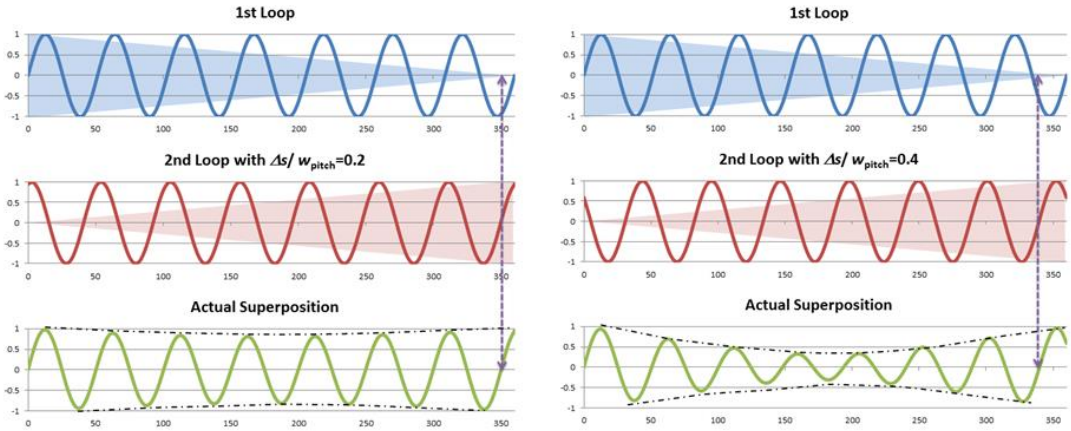

Figure 3. 21 Cycle length influenced by alignment error under "$\Delta s/ w_{pitch}$" value equals to 0.2 and 0.4. With x-axis indicating the rotating angle, blue curves show the output of 1st loop, red loops show the 2nd loop while green curve shows a weighted superposition of 1st and 2nd loop under condition described by Equation 3.9.

3.7 Factors Influence the Triboelectric Velocity Sensors Performance

Generally speaking, there are 3 factors that determine the vsTEG measuring range: the output signal amplitude, sliding spatial cycle (affected by θ) and program-allowed minimum timing interval. As the velocity decreases, the signal amplitude reduces (Figure 3.9) and as it approaches the reference voltage, the comparator will exhibit a propensity for instability that will result in a distorted conversion. Thus, this factor only restricts the minimum velocity that the vsTEG can measure. Observe that the spatial cycle factor $w_{pitch}/\cos(45° - \theta)$ in Equation 3.1 impacts the sliding velocity in a cyclic min-max curve. Suppose the spatial cycle increases (by either w_{pitch} or θ), the range will be shifted to a higher value at both min-max curve. The processing time at the minimal sampling point determines the maximum detectable velocity. Taking into account the necessary considerations that include the interrupt response, interference judgment, etc., the minimal processing time in our system is around 5 ms to yield a maximum velocity of 1730 rpm and 2.3 ms^{-1} in the rotary and linear motion, respectively. Further, the response sensitivity can be determined by computing the gradient $\mathrm{d}T/\mathrm{d}v_{sliding}$ from Equation 3.1,

$$\frac{\mathrm{d}T}{\mathrm{d}v_{sliding}} = -\frac{w_{pitch}}{\cos(45°-\theta)} \times \frac{1}{v_{sliding}^2} \qquad (3.10)$$

Observe that the sensitivity is highly impacted by the magnitude of the sliding velocity; a small change in the velocity can generate an order of magnitude change in the sensitivity.

3.8 Chapter Summary

In summary, invoking the two principles of triboelectrification and electrostatic induction, we demonstrated the working performance of a self-powered, dual-function velocity sensor that can detect rotary and linear velocities with high stability and accuracy. The

sensor is fabricated using two axially-aligned cylindrical structures coated with alternating Kapton and copper strips helical at a 45° angle with the cylinder axis. Our device is capable of measuring linear velocities of 0.1-0.6 ms^{-1} with an error < 0.5 % and rotation velocities of 300-700 rpm with an error < 0.9 %. The typical output voltages for a 3 MΩ external load of the vsTEG vary from several volts to 30 V, which is distinguishable in the signal conversion method for a logic circuit connection. A comparator, MCU and LED digital display are applied in the circuit for signal processing and result displaying. The work reveals the possibility of utilizing a TEG as an active signal source directly connected to a logic circuit. The resulting active signal analysis enables us to develop velocity and acceleration sensors, etc. for many industrial applications.

CHAPTER 4

SELF-POWERED THIN-FILM MOTION VECTOR SENSOR FOR DIRECTION SENSING

The dual-mode triboelectric sensor described in Chapter 3 depicts a device employed as an active velocity sensor. It is capable of measuring velocities of rotary and linear motions. In this chapter, we describe the device for determining the motion direction and the position information.

4.1 Current Attempts in Direction Sensing Based on Triboelectric Techniques

Directional velocity and displacement sensing as required by industry needs to be fast, continuous, robust with good accuracies and simple connections. Researchers have come up with several smart designs based on triboelectric effect,[54,93-96] however, none fulfilled all the requirement. A direction sensor based on an individual single-electrode TENG that has 4 grating branches with different length was developed and successfully applied in identifying direction and measuring velocity and acceleration (Figure 4.1).[93] Sliding from different directions over the TENG will generating a different pattern of the output, providing a determination on direction. The solution is smart and procedure is effective, however its application is weakened in several aspects. The direction sensing is very much localized and constitute a one-time measurement, which cannot be used for long range or long duration sensing. Moreover, the device needs to wait until the mover slides all over the function area to generate a result, which reduces its application for instantaneous response situations. Finally, the determination is made according to the magnitude of the signal. TENG signal magnitude, especially current magnitude, may be

significantly affected by moving speed and thus, the reliability of measuring accelerated velocity and direction simultaneously might be poor.

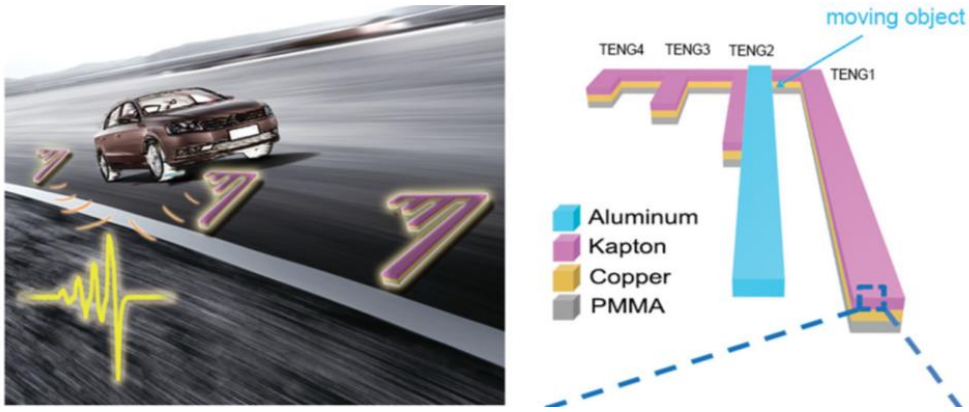

Figure 4. 1 A direction sensor based on an individual single-electrode TENG that has 4 grating branches with different length. (From Ref. 93)

Another attempt of triboelectric direction sensor is based on a serial of single-electrode base TENG that is located one after another in a line (Figure 4.2).[54] Once the mover slides over the individual TENG, the output generated by this TENG indicates the current position of the mover. Direction sensing function in this system is inherent because it already has the position recorded at all times. However, the system is not suitable for large scale and high resolution direction sensing. To sensing a single direction with 4 unit length, the system requires 4 terminals for signal reading already. These 4 individual signals cannot be joined into one terminal, as required for identifying which TENG is responding to the motion. Increasing the measuring range or increasing the resolution by shrinking the TENG surface will create an unacceptably large amount of terminal demands, especially for 2-D measurements.

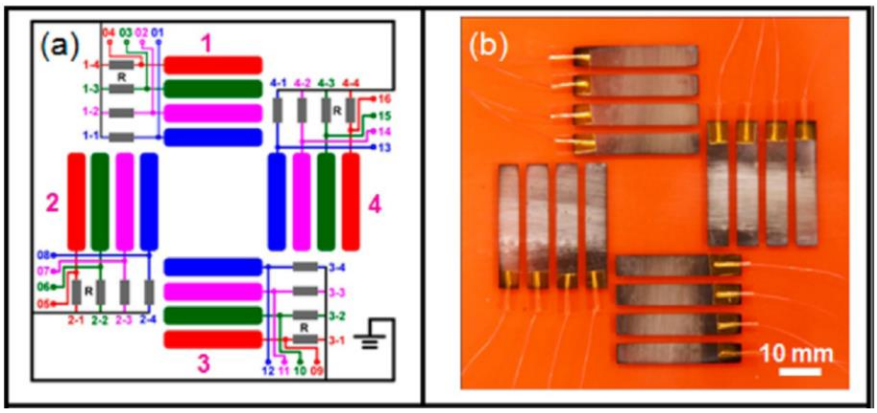

Figure 4. 2 Direction sensor based on a serial of single-electrode TENG. (From Ref. 54)

Both solution mentioned above adopted the signal-electrode TENG as their device mode, which is considered less efficient as with other double electrodes TENG modes.[97]

4.2 Design and Fabrication of the Thin-Film Motion Vector Sensor

In our work, a self-powered thin-film kinematic vector sensor for measuring displacement, velocity, acceleration and their directions is presented. By embedding 2-column arrays of copper electrodes into the polytetrafluoroethylene (PTFE) film of the mover and polyimide (Kapton®) film of the stator, triboelectric signals are generated during the relative reciprocation of the mover to the stator. To sense its moving direction, two sets of electrodes containing a small phase difference are used as markers and built into a direction-sensing TENG (dsTENG) unit for the 1-D and 2-D motion measurements.

4.2.1 Structural Design of the Thin-Film Motion Vector Sensor

The dsTENG (Figure 4.3a) consists of a mover (Figure 4.3b) and a stator (Figure 4.3c) that are fabricated from several layers of highly pliable thin films. The mover consists of a PTFE thin film deposited with two columns of 500 micron-wide copper electrodes with a

linear pitch of 1 mm (Figure 4.4a) on the surface that contacts with the stator. The electrodes of one column are placed at a quarter pitch offset with respect to the other column (Figure 4.3b). The stator consists of a Kapton film with both surfaces deposited with two fully aligned columns of copper electrodes (Figures 4.3c, 4.4b). The electrodes are placed on the top and bottom sides of the Kapton film at a linear shift of half of a pitch, which results in an alternating electrode pattern with one another (Figure 4.3c). All the copper electrodes are identical in dimension and when a relative movement occurs between the mover and stator, the electrode arrangement between the 2 contacting surfaces generates an alternating pattern of the electrodes coming into repeated alignments and misalignments.

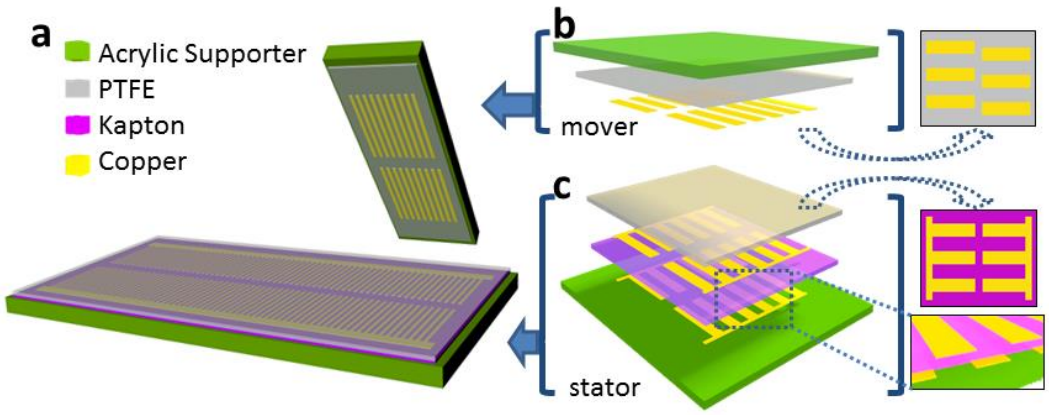

Figure 4. 3 Schematic structure of a dsTENG. (a) Schematic structure of a dsTENG. (b) Detailed composition layers for the mover part. (c) Detailed composition layers for the stator part.

A thin PTFE film covers the as-fabricated Kapton layer not only as a protector of the electrode channels but more importantly, as a high-performance electrification material for generating the triboelectric charges during the relative sliding motion.

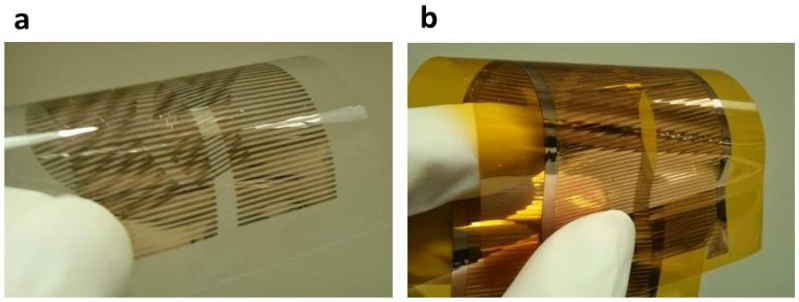

Figure 4. 4 Photo of the as-fabricated films. (a) Experimental fabrication of the PTFE film for the mover. (b) Experimental fabrication of the Kapton film for the stator.

All the films are thin and highly pliable, and thus, can be easily bent to fit a curved surface (Figure 4.4a, b). For our demonstration, the as-fabricated films are attached to a flat rigid acrylic holder (Figure 4.5a). To mitigate frictional effects during relative mover-stator motions, a Teflon nanoparticle spread is applied to the PTFE film (Figure 4.5b) to act as a lubricant and our previous testing in Chapter 2 showed that the nanoparticles do not appear to adversely affect the triboelectrification process.

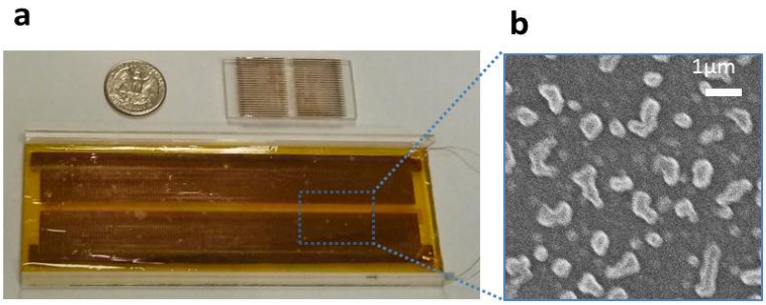

Figure 4. 5 Experimental structure of a dsTENG. (a) Assembled experimental demo. (b) Teflon nanoparticles spread on PTFE film.

4.2.2 Fabrication Process of the Thin-Film Motion Vector Sensor

The dsTENG consist of a mover and a stator, each of which are fabricated from the following steps.

Mover (1) Cut two columns of hollow strips with 500 μm strip width, 2.5 cm strip length and 1 mm pitch over a piece of 1.5 mm thick rectangular acrylic sheet (6 cm wide and 20 cm long) using a laser cutter. The two columns are separated with a 5 mm width and are shifted by a 1/4 pitch mismatch between each other. (2) Put the as-cut mask over a 6 cm width, 20 cm long and 150 μm thick PTFE film and then deposit a layer of copper (~200 nm) using the physical vapor deposition (PVD) method. (3) Remove the mask. As-fabricated film surface is shown in Figure 4.6. (4) Cut the film along its long side to form a 6 cm × 4 cm piece. (5) Mount the film using the back surface.

Stator (1) Cut the mask using the same parameters as in the Mover but without the 1/4 pitch mismatch between 2-column strips. (2) Put the as-cut mask over a 6 cm width, 20 cm long and 75 μm thick Kapton film and then deposit a layer of copper (~100 nm) using PVD method. (3) Do the same on the back surface of the Kapton film. This time, shift the mask by a 1/2 pitch toward the pattern on the front. (4) Remove the mask. As-fabricated film surface is shown in Figure 4.6. (5) Deposit 4 bus electrodes to individually connect each column strips using mask and PVD. (6) Remove the masks. (7) Cover a 6 cm width, 20 cm long and 75 μm thick PTFE film over the front surface of the as-fabricated Kapton. (8) Mount from the back surface of the Kapton.

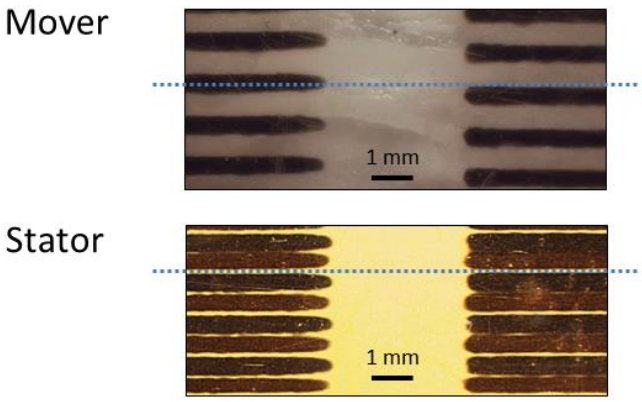

Figure 4. 6 Microscopy view of the electrodes on thin films from mover and stator. Electrodes on the mover has a one-fourth pitch shift; Electrodes on the stator are fully aligned.

4.2.3 Electric Connection of the Electrodes

To tap the resulting triboelectrification energy, the electrodes from one column of the Kapton film are connected via bus electrodes to form a top electrode (*TE*) on the upper surface of the Kapton film, and a bottom electrode (*BE*) for the ones on the bottom surface of the Kapton film. Together, the *TE* and *BE* form an electrode pair marked as a base channel (*BC*) with the other pair assigned as a reference channel (*RC*). The *TE* and *BE* from one channel are electrically connected through an external load for signal measurements (Figure 4.7).

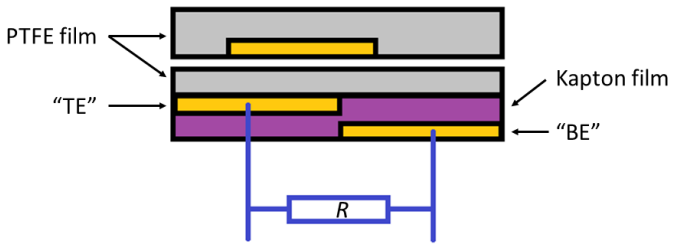

Figure 4. 7 Electric connection between top electrode (*TE*) and bottom electrode (*BE*). An external load R is connected between the TE and the BE.

4.3 Mechanism Study with FEM Simulation and Analytical Derivation

4.3.1 Mechanism

The mechanism for generating the triboelectric potential of a single channel is illustrated in Figure 4.8. Due to the coupling of the triboelectrification and electrostatic effects when the PTFE and copper are brought into relative motion (Figure 4.8a), electrons will be periodically driven to flow forward and backward between the *TE* and *BE* through an external circuit. Figures 4.8a-e depict the charge response in a single channel. As the mover slides over the stator, electrons from copper strips are injected into the PTFE film

by the triboelectrification.[29,30] Due to the differential contact areas and to maintain a zero total charge balance, the local charge density in the copper is higher than that in the PTFE.

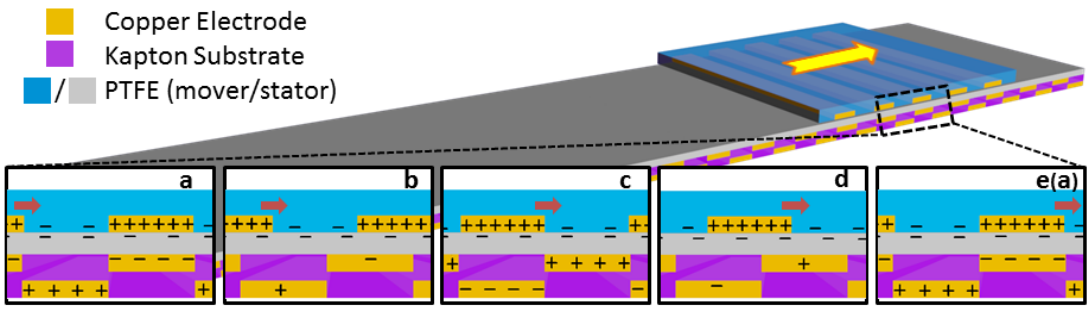

Figure 4. 8 Charge transfer mechanism of the dsTENG.

When motion occurs, charges in the strip pattern generates a corresponding electric potential distribution in the surrounding space that periodically attracts or excludes electrons from the neighborhood electrodes, resulting in an AC output. Hence, the dsTENG begins producing kinematic-sensing signals as soon as relative motion occurs between the contact interfaces of the mover and stator. For the dsTENG to sense direction vectors we employed an assaying technique to keep track of the signal cycles against the phase difference between the *BC* and *RC*.

4.3.2 FEM Simulation

The following electrostatic simulation can be used to better understand the process. When copper strips on the mover are aligned with the *TE* strips (Figure 4.9a), the *TE* is associated with the positive potential, which implies that the *BE* is negative. As they become aligned with the *BE*, the potential reverses sign (Figure 4.9b) and the open-circuit

voltage (V_{OC}) between the two electrodes can be computed from the following equation using Gauss theory. Details are presented in Chapter 4.3.3.

$$V_{oc} = \frac{2\sigma}{\varepsilon_0}\left[\frac{x \cdot d_1}{(l-x)\varepsilon_{r1}} - \frac{(l-x)\cdot d_1}{x\varepsilon_{r1}} - \frac{(l-x)\cdot d_2}{x\varepsilon_{r2}}\right] \tag{4.1}$$

where σ is the triboelectric charge density on PTFE; ε_0 is the permittivity constant in vacuum; d_1, ε_{r1}, d_2, ε_{r2} are the thickness and relative permittivity of the PTFE film and Kapton film on the stator respectively; l is the width of the electrode and x is the relative displacement between the mover and the stator.

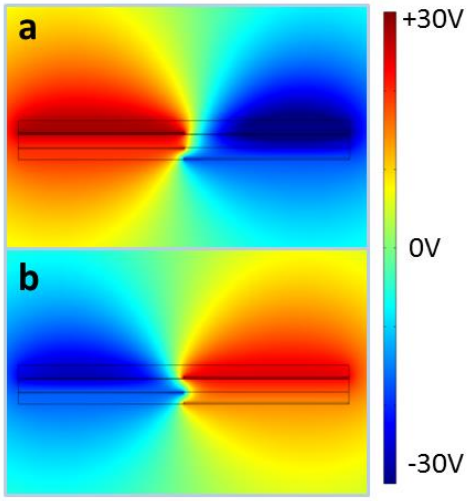

Figure 4. 9 Simulation results. (a) Potential simulation when copper strips on the mover are aligned with the TE strips. (b) Potential simulation when copper strips on the mover are aligned with the BE strips.

Figure 4.10 shows a plot of V_{OC} against position. Due to the non-symmetry of the structure, the output is also non-symmetric; however, the difference is relatively small that this will not affect the sinusoidal output sketched in the inset of Figure 4.10.

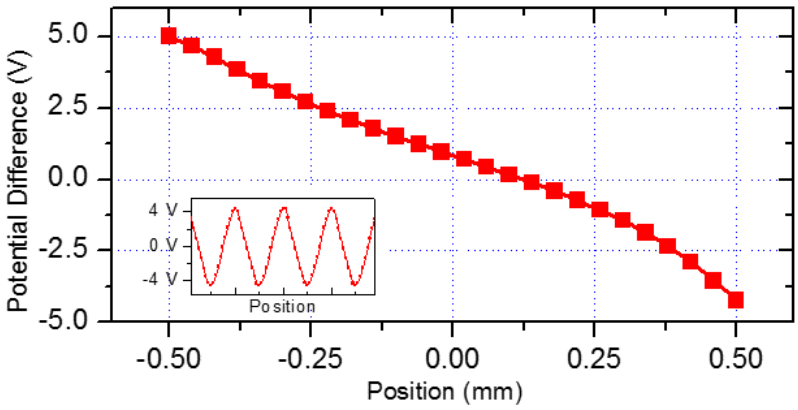

Figure 4. 10 Output voltage over positions between the two situation shown in Figure 4.9 a and b. (Inset: simulation result on multiple cycles)

4.3.3 Analytical Explanation on Charge Behavior

The output can be theoretically derived by utilizing electrostatic theories. Figure 4.11 shows an instant status of one unit (with length marked as $2l$) of the intersection of the dsTENG with charge distribution. The copper electrode in the mover is assigned with mark A, while the two electrodes for output in the stator are marked as B and C. The relative permittivity of PTFE (pink) and Kapton (gray) were set as ε_{r1} and ε_{r2}. A pre-applied charge density on the surface of PTFE between mover and stator is given as $-\sigma$. Relatively, considering the local contact area distribution between copper and PTFE is approximately 1:3, the copper electrode A should carry a total charge amount of $3 \times l \times \sigma$ in order to balance the negative charge on PTFE. Under open circuit condition, as electrode A has an *x* mismatch from electrode B, charges redistribute as shown in Figure 4.11.

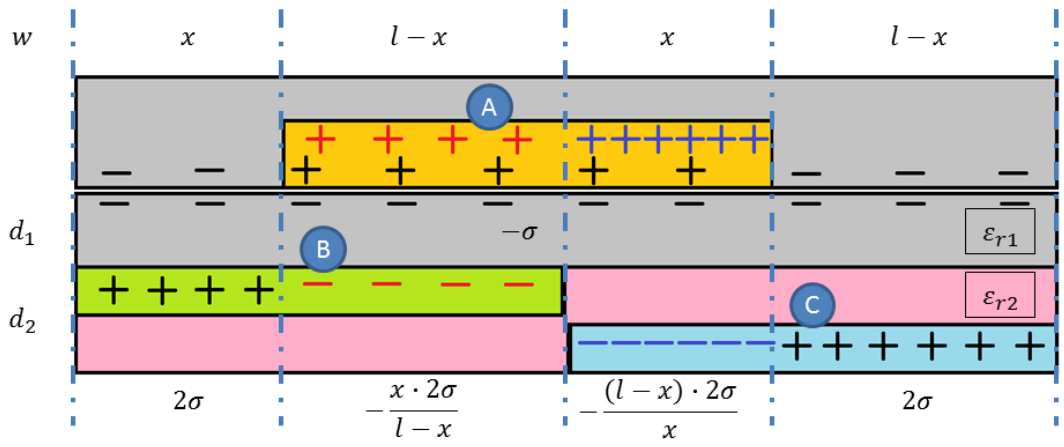

Figure 4. 11 Schematic diagram for theoretical derivation of output signal differential equations.

The voltage between metal A and B, as well as A and C can be described as following,

$$U_A - U_B = \frac{x \cdot 2\sigma \cdot d_1}{(l-x)\varepsilon_0 \varepsilon_{r1}} \tag{4.2}$$

$$U_A - U_C = \frac{(l-x) \cdot 2\sigma \cdot d_1}{x\varepsilon_0 \varepsilon_{r1}} + \frac{(l-x) \cdot 2\sigma \cdot d_2}{x\varepsilon_0 \varepsilon_{r2}} \tag{4.3}$$

where d_1, d_2 are thickness of PTFE film and Kapton film in stator. ε_0 is the permittivity in vacuum. The open circuit voltage output therefore can be calculated as,

$$U_{BC}^0 = U_C - U_B = \frac{x \cdot 2\sigma \cdot d_1}{(l-x)\varepsilon_0 \varepsilon_{r1}} - \frac{(l-x) \cdot 2\sigma \cdot d_1}{x\varepsilon_0 \varepsilon_{r1}} - \frac{(l-x) \cdot 2\sigma \cdot d_2}{x\varepsilon_0 \varepsilon_{r2}} \tag{4.4}$$

Or,

$$U_{BC}^0 = \frac{2\sigma}{\varepsilon_0}\left[\frac{x \cdot d_1}{(l-x)\varepsilon_{r1}} - \frac{(l-x) \cdot d_1}{x\varepsilon_{r1}} - \frac{(l-x) \cdot d_2}{x\varepsilon_{r2}}\right] \tag{4.5}$$

As there is an electronic load between metal B and C, a general voltage description V^{BC} using capacitor C_{BC} and charge Q^{BC} can be formulated using the following equations,

$$V^{BC} = -\frac{1}{C_{BC}} \times Q^{BC} + U_{BC}^{0} \tag{4.6}$$

$$V^{BC} = -\frac{1}{\varepsilon_0 w}\left[\frac{d_1}{(l-x)\varepsilon_{r1}} + \frac{d_1}{x\varepsilon_{r1}} + \frac{d_2}{x\varepsilon_{r2}}\right] \times Q^{BC} + \frac{2\sigma}{\varepsilon_0}\left[\frac{x \cdot d_1}{(l-x)\varepsilon_{r1}} - \frac{(l-x)\cdot d_1}{x\varepsilon_{r1}} - \frac{(l-x)\cdot d_2}{x\varepsilon_{r2}}\right] \tag{4.7}$$

Under open-circuit condition, charge transfer is zero,

$$V_{oc} = \frac{2\sigma}{\varepsilon_0}\left[\frac{x \cdot d_1}{(l-x)\varepsilon_{r1}} - \frac{(l-x)\cdot d_1}{x\varepsilon_{r1}} - \frac{(l-x)\cdot d_2}{x\varepsilon_{r2}}\right] \tag{4.8}$$

Since

$$C_{BC} = \frac{1}{\frac{1}{C_{BA}} + \frac{1}{C_{CA}}} \tag{4.9}$$

$$C_{BA} = \frac{\varepsilon_0 \varepsilon_{r1}(l-x)w}{d_1} \tag{4.10}$$

$$C_{CA} = \frac{1}{\frac{d_1}{\varepsilon_0 \varepsilon_{r1} x w} + \frac{d_2}{\varepsilon_0 \varepsilon_{r2} x w}} \tag{4.11}$$

$$C_{BC} = \frac{1}{\frac{d_1}{\varepsilon_0 \varepsilon_{r1}(l-x)w} + \frac{d_1}{\varepsilon_0 \varepsilon_{r1} x w} + \frac{d_2}{\varepsilon_0 \varepsilon_{r2} x w}} \tag{4.12}$$

Combining the results with Ohm's law we get:

$$V^{BC} = I \cdot R \tag{4.13}$$

From the current, the output must satisfy the following equations,

$$x = vt \tag{4.14}$$

$$I = \frac{\mathrm{d}Q^{BC}}{\mathrm{d}t} \tag{4.15}$$

$$V^{BC} = \frac{\mathrm{d}Q^{BC}}{\mathrm{d}t} \cdot R \tag{4.16}$$

$$R \cdot \frac{\mathrm{d}Q^{BC}}{\mathrm{d}t} = -\frac{1}{\varepsilon_0 w}\left[\frac{d_1}{(l-vt)\varepsilon_{r1}} + \frac{d_1}{vt\varepsilon_{r1}} + \frac{d_2}{vt\varepsilon_{r2}}\right] \times Q^{BC} + \frac{2\sigma}{\varepsilon_0}\left[\frac{vt \cdot d_1}{(l-vt)\varepsilon_{r1}} - \frac{(l-vt)\cdot d_1}{vt\varepsilon_{r1}} - \frac{(l-vt)\cdot d_2}{vt\varepsilon_{r2}}\right] \quad (4.17)$$

As an analytical result, when the *TE* and *BE* are connected by an external load R, electrons begin to flow between these two electrodes. The response is governed by the pair of differential equations given by Equations 4.16 and 4.17.

4.3.4 Distinctive Structure and Mechanism from That of the Linear/Rotary Velocity Sensor

The structure as well as the working mechanism in dsTENG is distinctive from that in dual-mode velocity sensor mentioned in Chapter 3. In this work, the electrodes that produce signal are all on stator, while the mover itself is freestanding from the stator. The mover only plays the roles of electrification and inducing the electrons to flow. Electrons are only transferred from and to the electrodes on the stator. No electron exchange happens between the metal parts of the mover and the stator. No wire is need for the mover, which means the mover is able to endure long range, high speed and repeated test without considering the wire connection problem.

The function is fulfilled by two channels of signal, which are produced by two sets of grating-structured TENG. Former TENG designers focus on using more than one sets of TENG to enhance their electrical output.[56,87] To achieve higher output, all sets of TENG need to work simultaneously under external excitation. Outputs that are not synchronized may neutralize each other. The dsTENG consists of a built-up of two sets of TENGs so that their outputs, which inherently possess a phase difference can be used to determine the motion directions.

4.4 Design Optimization

The output signal is affected by factors such as the thickness of PTFE and Kapton films, the width of the copper strips, external load and sliding velocities. To understand their relationships, we numerically simulate both V_{OC} and the total transferred charges (Q_{SC}) using Equation 4.1 and Equation 4.17 by varying the structural dimensions of the films and copper strips (Figures 4.12a, b, c).

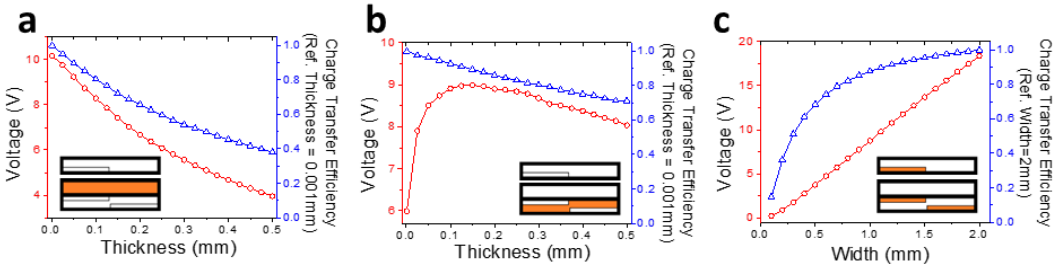

Figure 4. 12 Theoretical simulation results about the (a) effect of the thickness of PTFE film on stator; (b) effect of the thickness of Kapton film and (c) effect of the width of the copper electrode. Insets in (a)-(c) indicates the variable reflected on the structure.

As the thickness of the PTFE film (in stator) increases from 0.001 mm to 0.5 mm (Figure 4.12 a), the V_{OC} decreases from about 10 V to approximately 4 V, and the charge transfer efficiency (which is defined as the transferred charge in current given situation compared to reference situation) is approximately 40% at 0.5 mm compared to the reference as at 0.001 mm. This is because a thicker PTFE behaves like a dielectric layer by reducing the penetration of the electric field in the mover. When the thickness of the Kapton film is increased from 0.001 mm to 0.5 mm (Figure 4.12 b), the V_{OC} first increases dramatically to a peak value at about 0.1 mm and then, decreases but not by much. However, the charge transfer efficiency maintains an almost a linear decrease with increasing thickness. As the width of the copper strip increases from 100 μm to 2 mm, the

edge effect exhibits a reduction and thus, both V_{OC} and charge transfer effectively increase correspondingly.

4.5 Output Characterization

Based on the simulation results obtained from figure 4.12, we fabricated a dsTENG sensor with the following structural dimensions: 25 µm PTFE film, 75 µm Kapton film and 500 µm wide copper strips. Noting that a higher voltage output is obtained at either larger loads or higher velocities (Figure 4.13a), the output performance is measured at varying external loadings and velocities (Figures 4.13a, b, c). When the load becomes sufficiently large, the voltage output converges to V_{OC}. The results indicating the select of external loads should be large enough. Further, the maximum output power for varying velocities occurs at varying external loads (Figure 4.13b) with a higher power occurring at a higher velocity. Although the output power does not have much influence in signal recognizing in the next step, higher output power may guarantee a reliable driving capability. As a result, the external load could be chosen as several mega ohm.

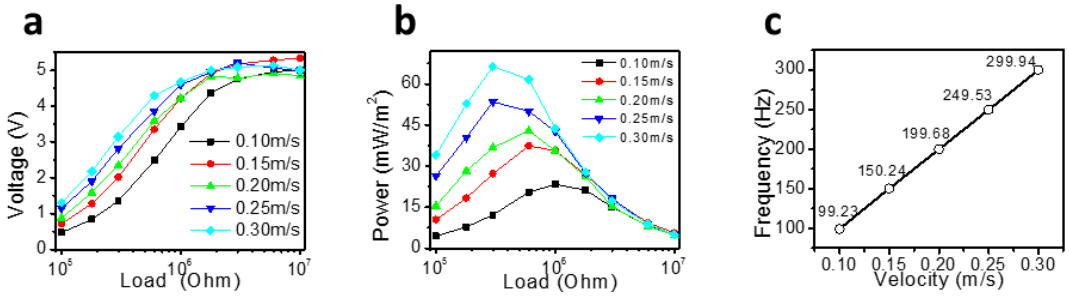

Figure 4. 13 Experimental measured results for a fabricated dsTENG: (d) Output voltage over different external resistance; (e) Output power over different external resistance; and (f) Dominant output frequency over different moving velocities.

Most important, the signal contains the information of the moving speed. The signal frequency is conducted using the fast Fourier transform (Figure 4.14) and the result exhibits a strong linear relationship with velocity (Figure 4.13c), which is desirable as it indicates that the device will be a reliable velocity sensor.

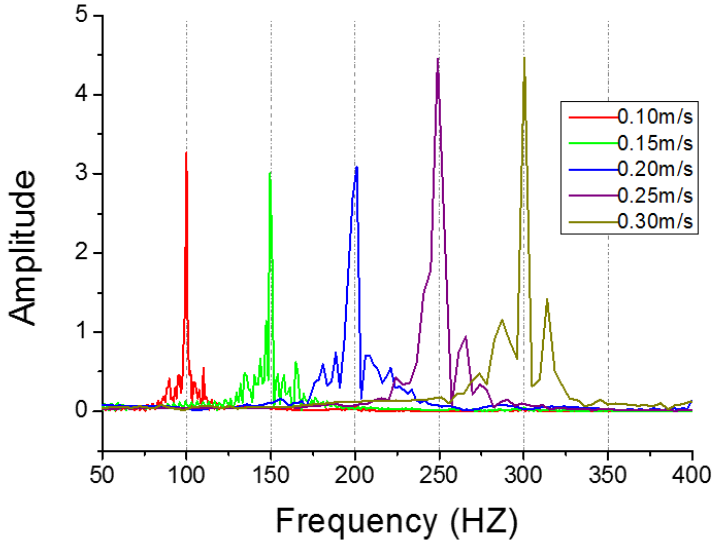

Figure 4. 14 Fast Fourier transform toward outputs over varies velocities. The amplitude on y-axis is defined as the spectrum compared with the mean value. Dominant frequencies of these outputs show a great linear relationship with driven velocity.

4.6 Signal Conversion, Recognition and the Velocity Measurement Test

4.6.1 Electric Circuit Diagram

A schematic circuit diagram connecting the dsTENG and comparator is shown in Figure 4.15. The output signal generated by dsTENG is detected over the external load R and conducted to a comparator. Each of base and reference channels have to be connected to an individual comparator. The converted signal is then sent to signal acquisition card for computer processing.

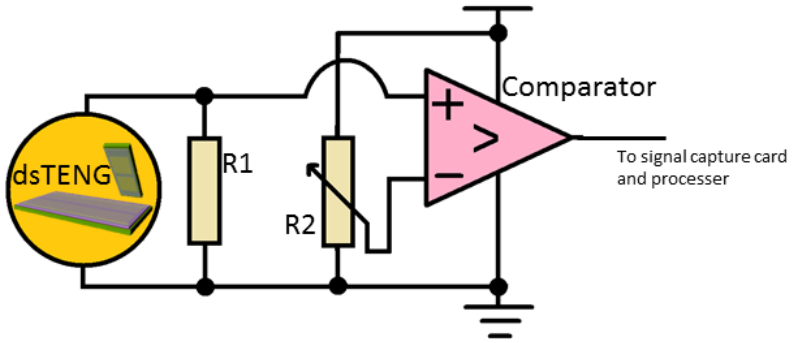

Figure 4. 15 Circuit connection between dsTENG channels and comparator for each channel of signal.

4.6.2 Signal Conversion

To sense motion directions, the device requires both *BC* and *RC* to be working simultaneously. The dual channel signal measurement unit (Figure 4.16a) records output signals from both channels as the mover performs reciprocating motion over the stator. Due to the quarter pitch difference between the two channels, the reference signal occurs either after (Figure 4.16b) or before (Figure 4.16c) the base signal depending on the motion direction. The signal can be processed by a comparator (Figure 3.11), which is an analog to transistor-transistor logic (TTL) signal converter based on a given reference voltage, into computer readable signal serials (Figures 4.16d, 4.16e). Within one cycle, the motion direction can be uniquely determined by comparing a half-cycle length and the time difference between the “falling edges” of the *BC* and the follow-up *RC* outputs.

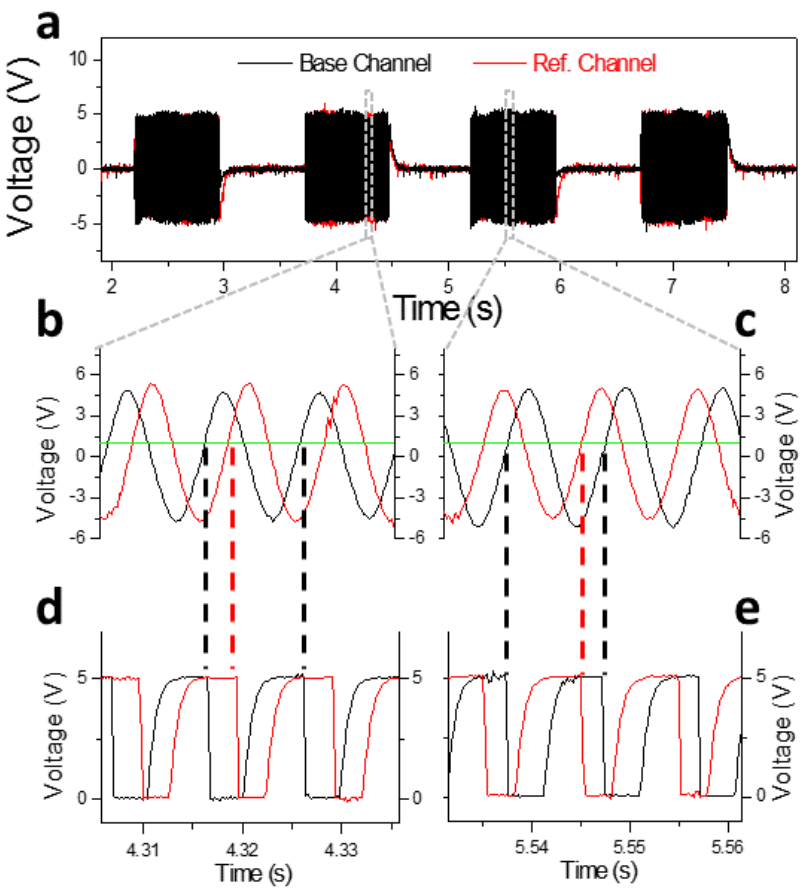

Figure 4. 16 Direction sensing mechanism. (a) 2 Channel signal measuring from base channel (BC) and reference channel (RC). (b) Local signal form when the mover is moving "forward". (c) Local signal form when the mover is moving "backward". (d) Local transformed TTL signal when the mover is moving "forward". (e) Local transformed TTL signal when the mover is moving "backward".

4.6.3 Signal Processing and Directional Velocity Calculations

The cycles and intervals are automatically timed and processed by the Labview® program for simultaneous magnitude and direction displays of the velocity with instant velocities computed from the *BC* pitch width divided by the instant full-cycle time length. The data flow chart for complete signal processing is displayed in Figure 4.17. The signal is proceeded in a consequent approach.

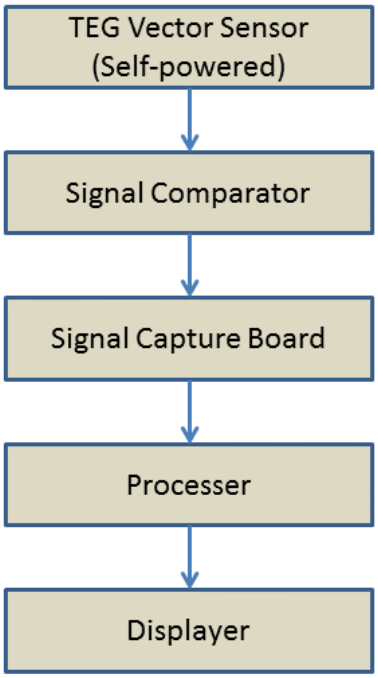

Figure 4. 17 Data flow chart for whole signal processing.

The mover is then connected to a programmable linear motor capable of generating varying types of reciprocation that includes uniform velocity motion, uniform acceleration to a constant velocity motion, uniform acceleration to a uniform deceleration motion, etc. The corresponding measured result by our sensor is displayed in Figure 4.18a, b and c, respectively. The results show a consistently successful tracking of the motion. With the velocity vector fully determined, it is easy to compute the remaining 2 kinematic parameters of position and acceleration.

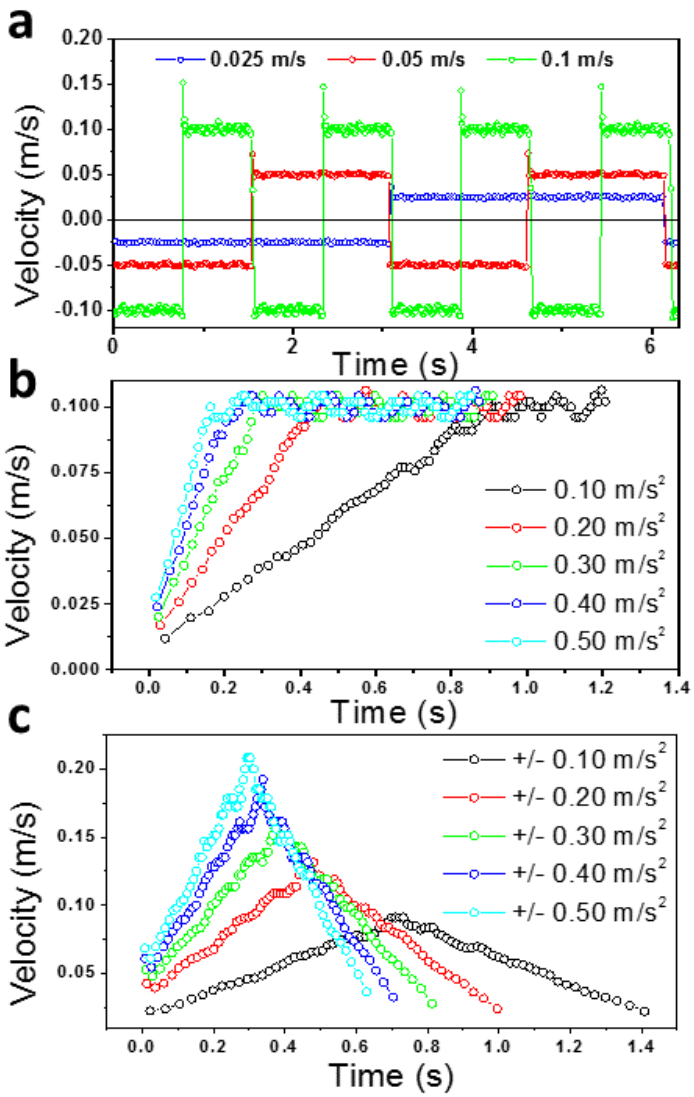

Figure 4. 18 Kinematic measured results. (a) Velocity measuring on uniform velocity reciprocating motion. (b) Velocity measurement on uniform acceleration motion. (c) Velocity measurement on uniform acceleration and deceleration motion.

The stability of measuring constant velocity is also studied during multiple measurement. Error diagram on repeating measurement of constant velocity is shown in Figure 4.19. The velocities are measured under several different driven speed. Error bar shows the standard deviation in different tests.

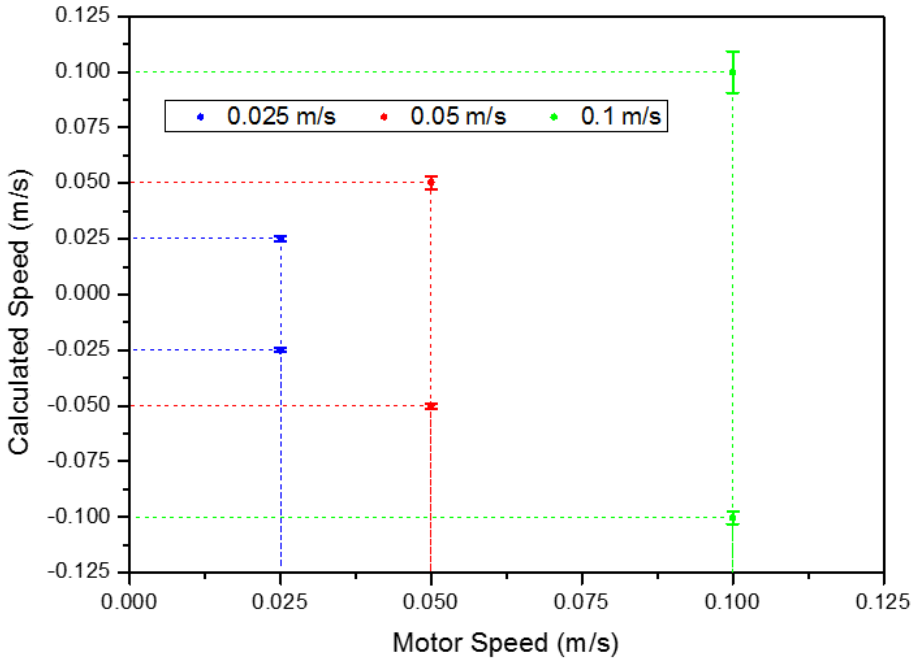

Figure 4. 19 Error diagram on repeating measurement of constant velocity.

4.7 Durability Test

All our test results showed that the technique we have developed for direction sensing is highly reliable and highly repeatable (Figure 4.19). Further, with the electrodes for output measurements placed only in the stator, which is protected by the PTFE polymer film, frictional and other abrasive effects are minimized and this ensures a highly reliable and repeatable functioning of the device. We carried out durability test with over 86,000 sliding motions under an open-circuit condition without observing measurable output deteriorations (Figure 4.20). The first 43000 slides were under 40 slides/min and the following 43000 slides were under 72 slides/min compositing a total length of 28 hours. Even after enduring with more sliding cycles that the sensor calls for maintenance, the only component that requires replacement is the copper electrodes in the mover when they are worn-out.

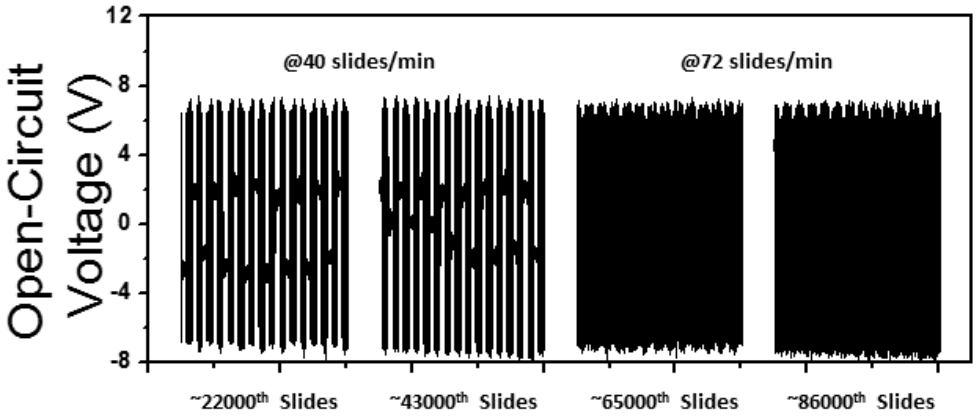

Figure 4. 20 Durability test of the device in continuously reciprocating motion and with open-circuit voltage monitored.

4.8 The Vector Sensors in Measuring 1-D and 2-D Directional Displacement

4.8.1 The 1-D and 2-D Kinematic Sensing Experimental Setup

The sensor is then set up to tests its performance in 1-D/2-D displacement sensing.

1- D Motion (1) Mount the mover and stator films onto the acrylic sheets. (2) Connect each bus electrode with copper wires. Two wires from base electrode or reference electrode are first connected over resistance, respectively. (3) Put the mover over the stator and make sure the strips are all paralleled. (4) Measure the output voltage over the resistance. (5) Connect output wires to the comparator LM393 (Texas Instrument® comparator) on the non-inverting input pin and common ground of the circuit with the inverting input pin set as +1 V. (6) Handle the output signal from the LM393 with a data acquisition platform and Labview® for display on the screen. (7) Program the direction reading method (if necessary, reverse the role of the BC and RC). (8) The mover can be either mount to a driving device such as a linear motor (4.21a) or driven by hand (Figure 4.21b).

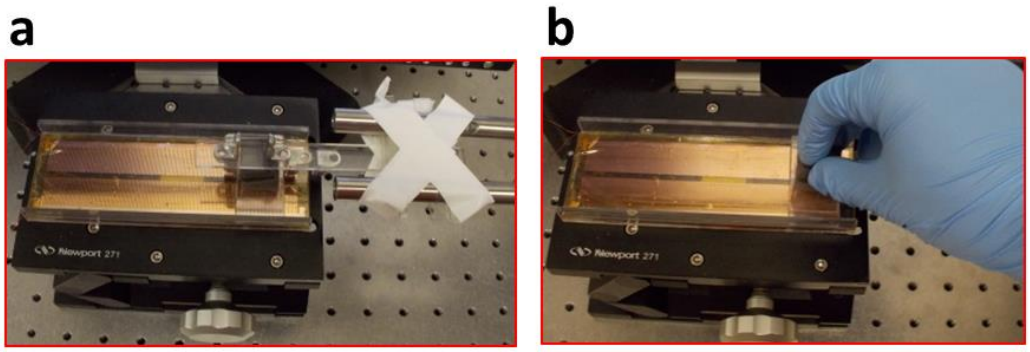

Figure 4. 21 Setup for 1D vector sensing. (a) dsTENG was mounted to a linear motor. (b) dsTENG was driven by hand.

2-D Motion Using two 1-D setup and mount them perpendicular to each other (Figure 4.22 a, b).

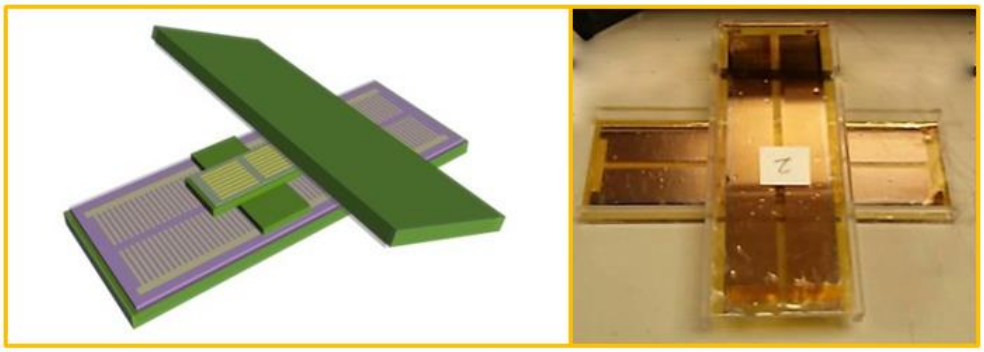

Figure 4. 22 Schematic diagram and experimental setup for 2D sensor.

4.8.2 The 1-D and 2-D Kinematic Sensing Demonstration

To demonstrate a working model in real-time, we built a 1-D position sensing system onto the dsTENG. The sensing system is able to record the mover's position vector (displacement) as driven by a linear motor (Figure 4.23) or a random force driven by

human (Figure 4.24). In Figure 4.23, the bottom curve is the programmed motion curve that the linear motor will follow, while the top curve, which is calculated from vector sensor's output signal, loyally records the motion. This depicts an accurate consistency between the monitored displacement-time curve and the programed curve of the linear motor. Meanwhile, the random movement driven by human hand is also successfully recorded in another test.

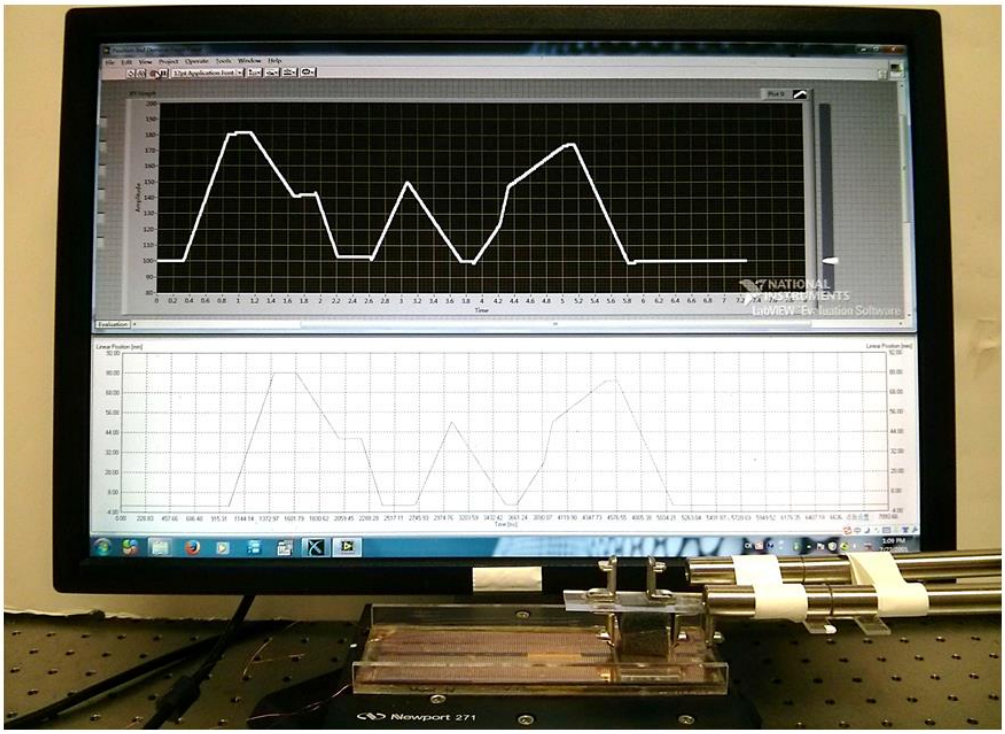

Figure 4. 23 dsTENG in recording motion from programed linear motor. Bottom window shows the working curve of the programmable linear motor. Top window shows the real-time measured displacement curve. (Both charts have y-axis as displacement and x-axis as time)

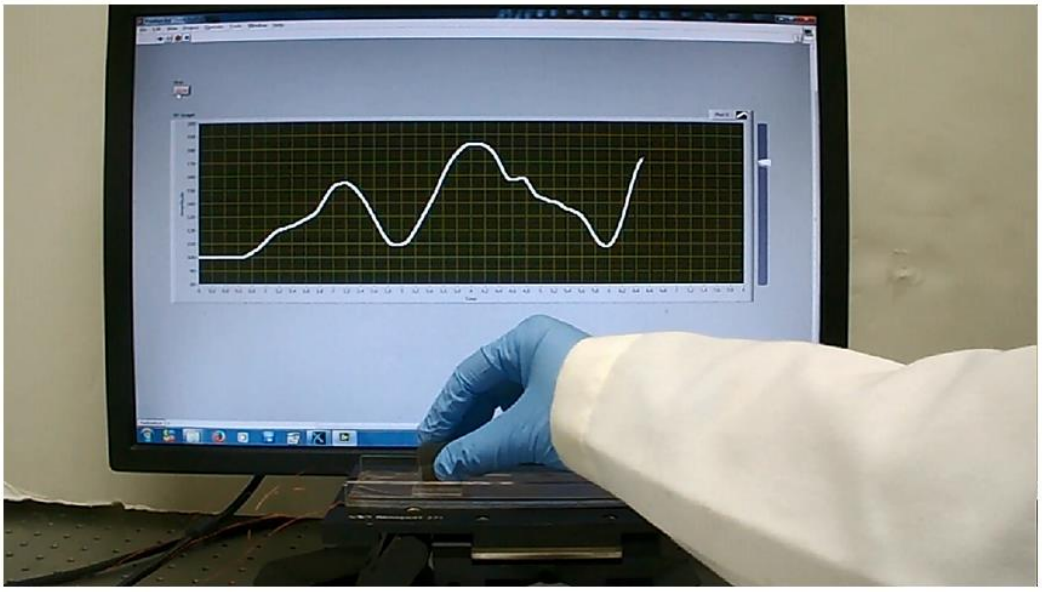

Figure 4. 24 dsTENG in recording motion from random driven. Window shows the real-time measured displacement curve. (Chart has y-axis as displacement and x-axis as time)

By integrating two as-fabricated sensors in a vertical connection (Figures 4.22), we fabricated a 2-D vector sensor that can act as an input terminal for a tracing system. In the demo (Figure 4.25a, b), the human is allowed to manipulate the indicator either freely (Figure 4.25a) or moving toward and catching the target (Figure 4.25b) using the 2-D sensor. The hardware resolution is approximately 50 dots per inch, which can be further improved via a hardware (i.e. structural) redesign or a software approach.

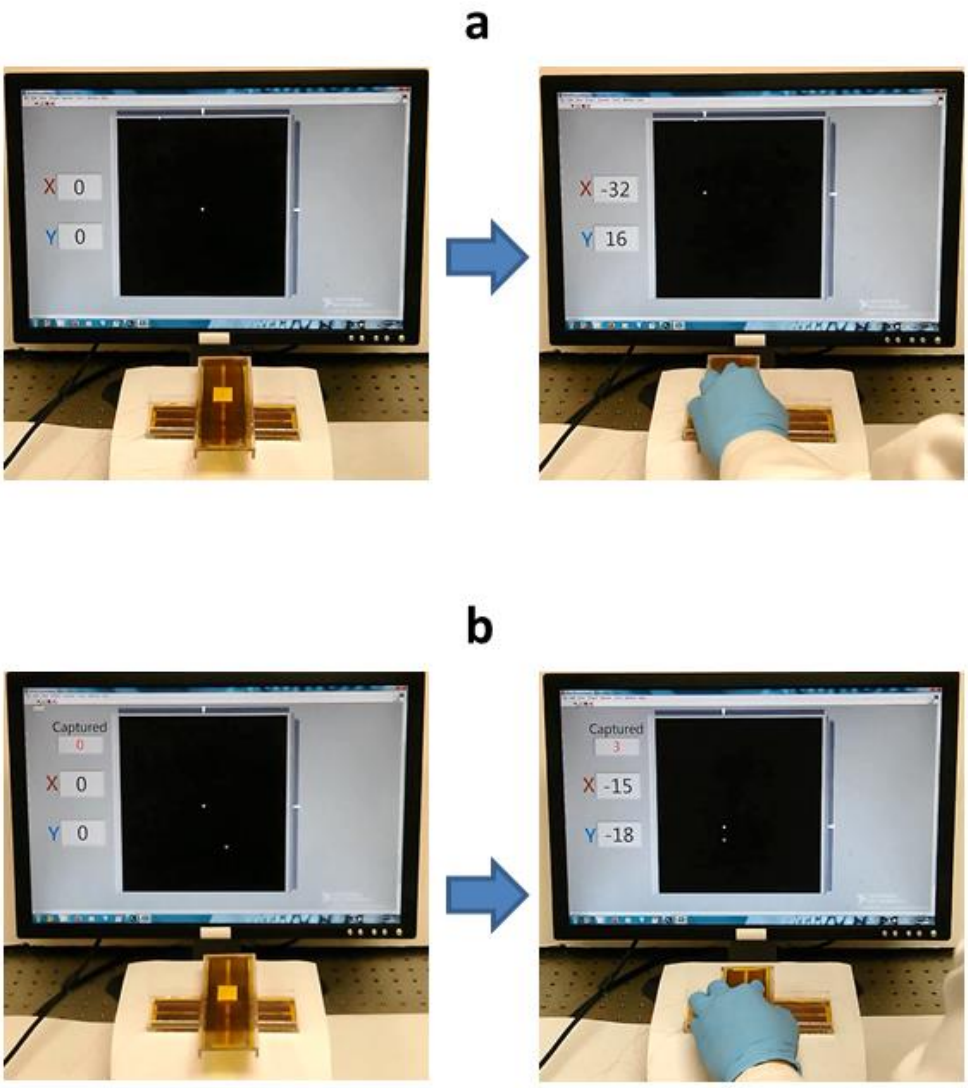

Figure 4. 25 User-interface for 2D sensor. (a) Move freely. (b) A moving and capturing game.

4.9 A Vector Sensor Applied to a Curved Surface

In addition to flat surface applications, the dsTENG by virtue of being fully pliable, can be easily bent to attach to all kinds of surfaces and/or extended in any direction, such as along the axis of a cylinder (Figure 4.26a) or its circumference (Figure 4.26b). Therefore, it can act as a vector sensor applied to a curved surface.

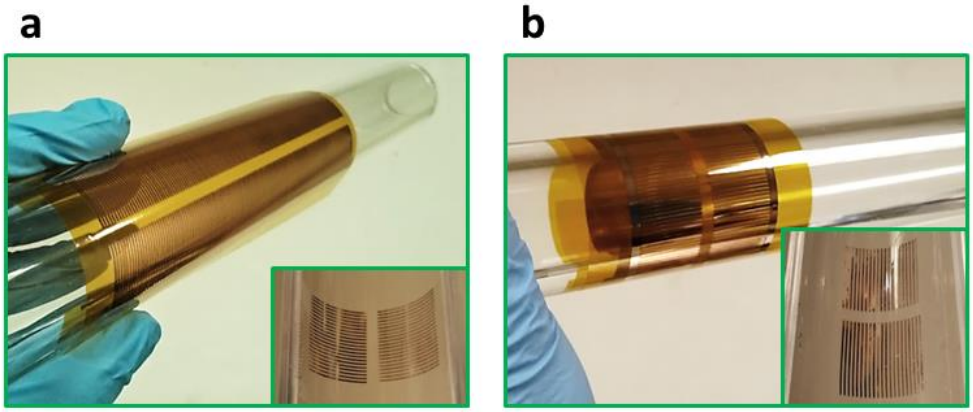

Figure 4. 26 dsTENG potentially applied on curved surface (a) dsTENG can be mounted along the axial of a cylinder. (b) dsTENG can be mounted to surround a cylinder.

4.10 Chapter Summary

Starting from the basic principle of triboelectric nanogenerator, we have developed a fast-response demonstration of a self-powered kinematic vector sensor for magnitude and direction tracking and measurements for 1-D and 2-D motions that can be applied in continuous and long range motions. Our device is fabricated on highly pliable thin films that can be easily bent to adapt and fit any curved or irregular surfaces. The hardware resolution in the dsTENG is approximately 50 dots per inch and can be further improved via a systematic optimization of the structural dimensions of the thin film and copper electrodes. The sensor possesses excellent stability with good repeatability and produces a strong signal durability. We showed that it is technologically feasible to sustainably harness triboelectric energy on a macro scale to self-power sensors and small devices for reliable and robust operations.

CHAPTER 5

A SELF-POWERED ANGULAR MEASUREMENT SENSOR

The dual-mode velocity sensor and directional kinematic sensor mentioned above are all patterned with strips. Design of this kind is capable of detecting kinematic physics such as acceleration, velocity and relative displacement. However, when it comes to absolute position detection, the uniform strip design could do little to help identify the current position because it does not contain the necessary information in the signal. In this chapter, we will discuss an approach of fabricating the triboelectric nanogenerator with encoded pattern, which provides a solution for an absolute angular position sensing.

5.1 Current Methods in Angular Measurement

Angular measurement is a common and essential technology in industrial and manufacturing systems. Over the past decade, major advances have occurred in angular measurement based on optoelectrical transformation,[98,99] electrical effects,[100] electromagnetic induction,[101,102] and MEMS/fiber-optic gyroscope techniques.[103,104] However, widespread usage of these techniques is likely to be shadowed by possible limitations, such as structural complexity, requirement of sophisticated materials, and a dependency on an external power source.

The open-circuit voltage has been a key parameter in characterizing the generating ability of TENG. It has also been widely used as an important reference in TENG based sensors. Even though the equipment requirement of measuring open-circuit voltages is strict to avoid unnecessary circuit interference brought about by the use of the equipment. The open-circuit voltage has the advantages of keeping its output level for a

certain period of time even though the sensor or device is not in motion, which makes the device suitable for measuring quasi-static physical parameters, such as the displacement.

Here, for the first time, we introduce a new principle in angular measurements by fabricating a quasi-static triboelectric sensor (QS-TES).[105] The as-fabricated self-powered sensor is based on a periodic contact and separation between the foam with copper material and a fluorinated ethylene propylene (FEP) film. The absolute angular position of rotating object can be read and remembered regardless being continuously monitored with the self-powered sensor.

5.2 Design and Fabrication of the Angular Measurement Sensor

5.2.1 Structural Design of the Angular Measurement Sensor

The self-powered angular sensor has a multi-layered structure that consists of two parts, a rotator and a stator, as sketched in Figure. 5.1. The TENG consists of 4 channels (L1-L4) that work simultaneously during angular sensing. The channel are located concentrically with unique patterns on the electrification surface. Each channel works under the principle of individual sectored structured single electrode TENG. The rotator is driven coaxially with stator.

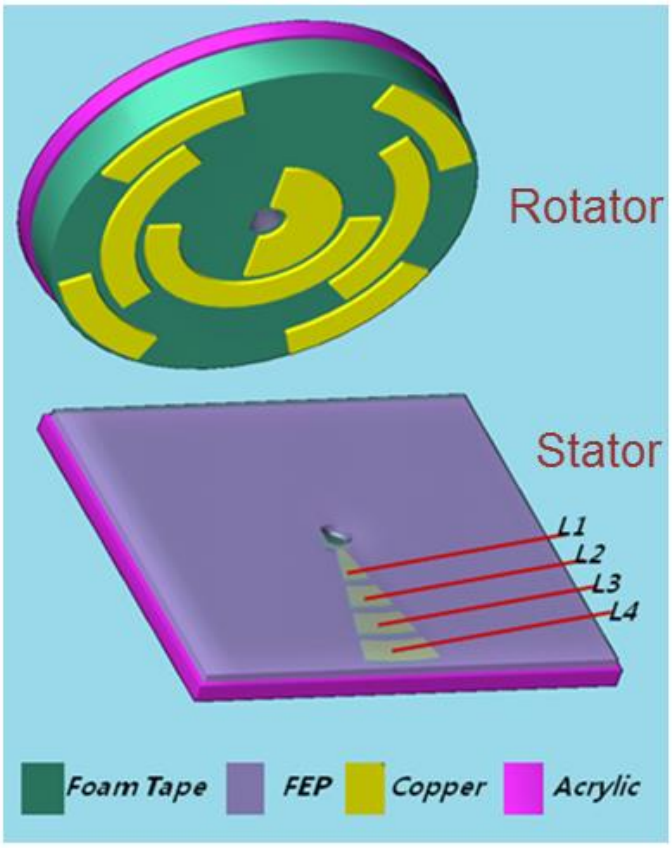

Figure 5. 1 Schematic illustrations of the self-powered angel monitor, which is composited with a rotator and a stator.

The rotator is composed of three layers: a rigid substrate layer made of acrylic, a soft supporting layer made of a pattern-carved foam followed by a deposit layer of copper forming foil sectors as an electrification layer (Figure 5.2a). The rotator is a collection of radially-arrayed sectors separated at equal-degree intervals as shown. A layer of copper thin film was deposited on the foam to form a coded copper foil sector. A Scanning Electron Microscope (SEM) image of the copper film is shown in Figure. 5.2b, in which the inset depicts the SEM image at a higher magnification.

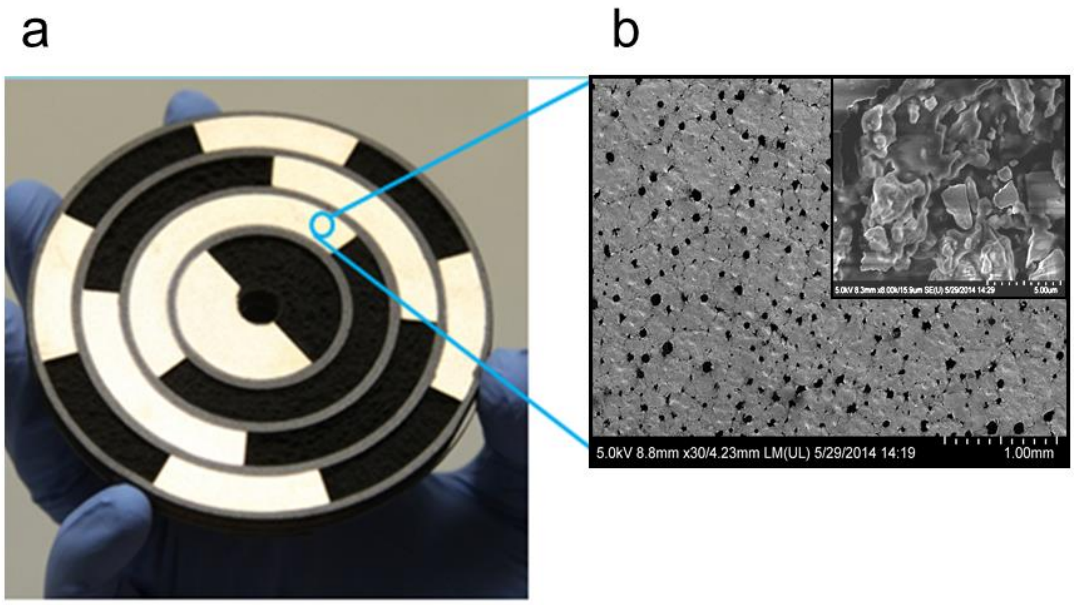

Figure 5. 2 Structure of the rotator. (a) Photograph of a rotator. (b) SEM picture reveals the copper foil coated on the foam. The inset is the enlarged SEM image.

The stator has a vertical-stacked structure consisting of three layers (Figure 5.3a). First, a layer of copper was deposited onto the acrylic substrate, and then, a layer of FEP was spread out on the copper surface, working as an electrification layer. Here, the FEP and copper were selected as contact materials for generating the triboelectric charges due to their large difference in electron affinity. As shown in an SEM image in Figure 5.3b, spherical polytetrafluoroethylene (PTFE) nanoparticles were utilized as lubricant to mitigate friction and to further improve energy conversion efficiency.

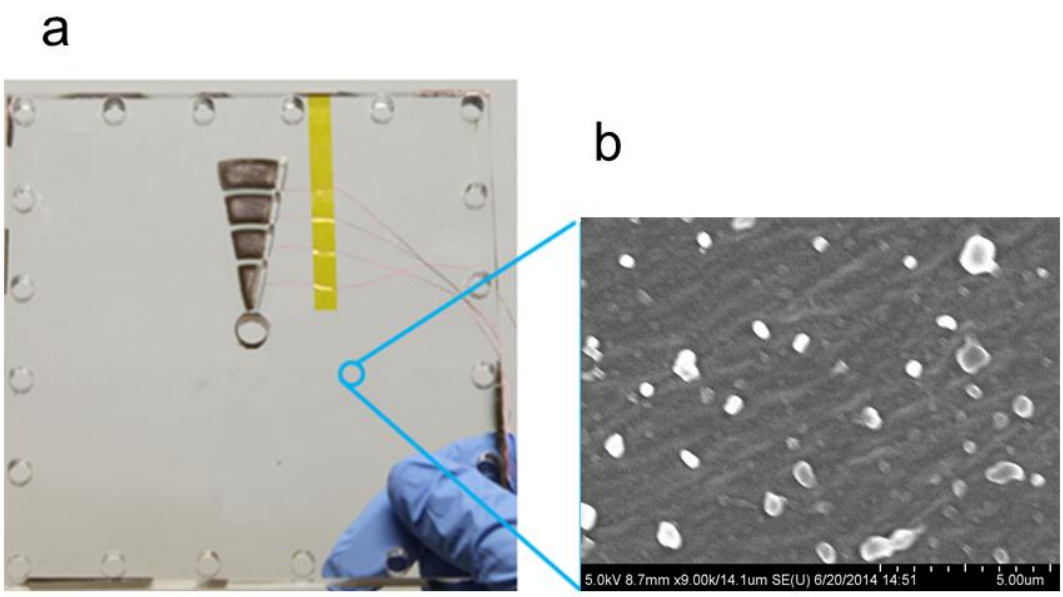

Figure 5. 3 Structure of the stator. (a) Photograph of a stator, wires are connected to the edges of each electrode and then conducted through the narrow holes to the back side of the supporter. (b) SEM image shows PTFE particles spread on the surface of FEP.

To operate the sensor, the stator is anchored while the rotator rotates relative to it for the angular measurements. When the monitored object rotates, the rotator slides over the FEP film, where the alternating flows of electrons are induced between the copper bottom electrodes and the ground (detailed in Chapter 5.3.1). The analysis of output voltage generates a series of code provided by copper foil sectors on the rotator, which corresponds to the angular difference. The angel can be obtained by reference to the output voltage signal.

5.2.2 Fabrication Method of the Angular Measurement Sensor

The QS-TES consists of a stator and rotator. These 2 components are fabricated as follows.

Stator (1) Cut a disc-shaped polyimide substrate (25 mm) with a lead wire hole as a substrate using a laser cutter; (2) Use photolithography (negative photoresist) to create exposed windows that define electrodes on the substrate; (3) Deposit metal layer by an e-beam evaporation, followed by a lift-off process to generate the electrode pattern on the substrate; (4) Connect four lead wires respectively to the electrodes; (5) a 0.5 g sample of commercial PTFE dispersion which contains the PTFE nanoparticles dissolved in isopropyl alcohol was sprayed on the surface of FEP thin films and dried in air. Adhere the thin layer of FEP (25 mm) on top of the electrode as an electrification layer. (6) Metal wires were connected to electrode located under the FEP film via lead wire hole from the bottom of the polyimide substrate, as outer electrode.

Rotator (1) Cut a disc-shaped polyimide substrate (25 mm) as a substrate with through-patterns that consist of radial arrayed sectors using a laser cutter; (2) Drill a through-hole that has a D-profile at the center of the rotator; (3) Use Ar/O_2 plasma (100 W) to do surface treatment on the substrate for 1 min; (4) Deposit a layer of Ti (10 nm) and then a layer of Cu(200 nm) on the rotator in sequence using a DC sputter.

5.3 Simulation and Analytical Results on Mechanism Study

5.3.1 Working Mechanism

The operation of the TENG sensor relies on relative rotation between the rotator and the stator, in which the coupling between triboelectrification and electrostatic induction gives rise to an alternating flow of electrons between the electrodes. The electricity-generating process is schematized through the basic unit shown in Figure 5.4. We define the initial state (Figure 5.4a-I) and the final state (Figure 5.4a-III) as the states when the rotator is aligned with bottom electrode and completely mismatched with the bottom electrode,

respectively. The intermediate state (Figure 5.4a-II) represents the transitional process in which the rotator spins from the initial position relative to the final position.

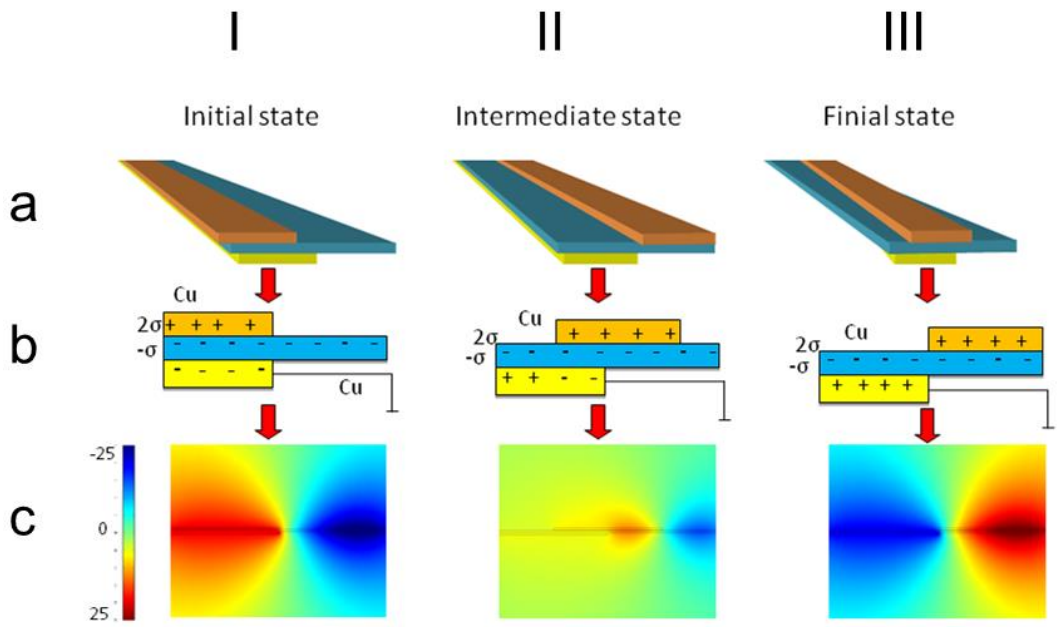

Figure 5. 4 Schematics of operating mechanism of sensor. 9 sub-figures are included and indicated with the combination of a, b, c and I, II, III (a) Three-dimensional schematic for operating status. (b)Charge distribution in short-circuit condition. (c) FEM simulation of electric potential distribution in open-circuit condition. (I) Initial state in which the rotator is fully aligned with the bottom electrode (II) Intermediate state in which the rotator is spinning away from the initial position at an angle. (III) Final state in which the rotator is fully mismatched from the bottom electrode.

Since the rotator and the stator are in direct contact, triboelectrification creates a charge transfer on the contacting surfaces, with negative charges generated on the FEP and positive ones on the metal[59] as illustrated in the cross-sectional view defined by an arbitrary intersection in Figure 5.4b I-III. Due to the law of charge conservation, the density of positive charges on the rotator is twice as much as that of negative ones on the stator because of unequal contact surface area of the two objects. As shown in Figure 5.2,

copper is patterned on the disk to form the radially-arrayed metal and non-metal sectors, which result in the disk-shaped components with four channel circle. For each channel, after a few times of sliding until the charge density reaches a saturate status, FEP attracts electrons from the patterned electrode on the foam, leaving net negative charges on the FEP surface and an equal amount of positive charges on the foam. The generated negative triboelectric charges distribute evenly on the FEP film and remain for an extended period of time. As long as the copper sector is not approaching, these negative triboelectric charges on the FEP film induce positive charges on the copper bottom electrode from the ground as induced charges. Once the copper metal sector approaches the copper bottom electrode, the positive triboelectric charges on the metal sectors will drive electrons to flow from the ground to the copper electrode, screening the electric field from the charged electrodes. When the metal sector is aligned with the electrode, the negative charges were maximized on the copper electrode, as sketched in Figure 5.4b-I. As the rotator copper foil sector starts to move away from the copper bottom electrode, the induced electrons will flow back to the ground, leaving fewer negative charges on the copper electrode, as shown in Figure 5.4b-II. When the rotator come to its final state in Figure 5.4b-III as the copper foil sector is just separated from the bottom electrode, leaving fewer positive charges on the copper electrode.

5.3.2 Local Simulation on Voltage and Charge Transfer

To derive a more quantitative understanding of the proposed signal-generating process of the QS-TES, the electric potential distribution and charge transfer process for the device are investigated via numerical calculations using COMSOL. The quantity of the triboelectric charges on the surfaces of the stator and FEP film was assigned to be -20 $\mu C/m^2$ as an equivalent result of triboelectrification.[29] Both a local intersection and the

integrate channel 3 was chosen as the simulation model and was conducted with voltage and charge calculation.

Figure 5.4c I-III show results of special potential distribution under open-circuit condition reflected on a local intersection of the device, in accordance with Figure 5.4a and b. Figure 5.5a illustrates the status of the electric potential distribution from channel 3 when the rotator counter clockwise rotates one cycle. Two metal sectors are on this channel. The calculated electric potential as a function of the rotation angle is plotted in Figure. 5.5b, exhibiting the simulation results of the open circuit voltage in the QS-TES when rotator with metal sectors slides in and off from the bottom electrode. When the copper foil sector on the rotator is fully aligned with the bottom electrode, the electric potential on the FEP film area is ultimately positive, as shown in Figure 5.5a II and IV. Accordingly, the open circuit voltage curve reaches the positive maximum as shown in Figure 5.5b II and IV. The open circuit voltage is found to decrease dramatically as the distance between the rotator copper foil sector and the bottom electrode gets larger. When the carved sector on the rotator fully aligns with the bottom electrode, the electric potential on the FEP film is negative as shown in Figure. 5.5a I and III. Therefore, the open circuit voltage reaches the negative maximum as shown in Figure 5.5b I and III.

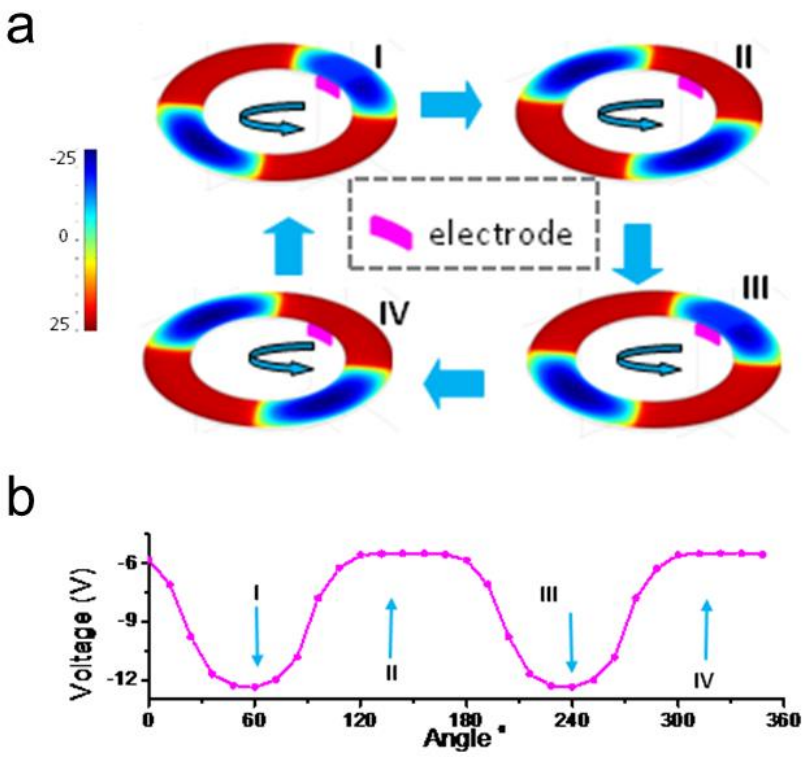

Figure 5. 5 Simulated open-circuit voltage. (a) Electric potential distribution of one channel in a complete counter clockwise rotating cycle (b) Finite-element simulation of the output voltage of one channel corresponding to the state change shown in (b).

5.3.3 Analytical Results

In the open-circuit condition, electrons cannot transfer between electrodes and the open-circuit voltage is then defined as the electric potential difference between the electrode and ground, namely, $V_{OC} = U_e$. The initial state corresponds to the minimum V_{OC}. Such a voltage increases as the rotator starts to spin. Once the copper foil sector on the rotator arrive at the area of the bottom electrode, V_{OC} with the opposite polarity starts to build up and get the maximum value until the metal sector aligned with the bottom electrode completely. After that, the output voltage decreases with further rotation until it reaches

the final state. A continuous rotation beyond the final state changes in a reversed way because of the periodic structure. On the basis of the assumption that the thickness of the dielectric layer is far smaller than its width dimension, an analytical model can be established, in which any overlapped region between the rotator and the electrode can be treated as a capacitor without consideration of the edge effect [28, 29]. Then the V_{OC} can be analytically expressed by the following equations using Gauss Theorem [8].

Initial state: $$V_{\mathrm{oc}} = \frac{\sigma \cdot \mathrm{d}}{\varepsilon_0 \varepsilon_{\mathrm{r}}} \quad (5.1)$$

Final state: $$V_{oc} = -\frac{\sigma \cdot d}{\varepsilon_0 \varepsilon_r} \quad (5.2)$$

where d is the thickness of the FEP layer, ε_0 is the dielectric constant of vacuum, ε_r is the relative dielectric constant of FEP. Equation 5.1 and 5.2 can only be used to estimate the positive and negative transferring trend of the V_{oc} from initial state to final state.

5.3.4 Define the Resolution

Consequently, as the rotator passes through the stator, an alternating flow of electrons occurs between the bottom electrode and the ground, which generates the output signal that varies with high and low electrical levels. Combining the copper foil sector position with the output signal from the multiple channels, the coded information of the sensor indicating the motion angle of a rotating object can be revived. The whole processes composite the working principles of the QS-TES angular sensor. According to the working principles of angular measurement, the resolution of the sensor is $1/2^n$ of 360° which can be improved by increasing the channel number *n*.

5.4 Signal Performance

To characterize the performance of the QS-TES for angular measurement, the electric output from four electrodes was simultaneously measured. To control the rotation rate for quantitative measurement, a programmable rotary motor was connected to the rotator that was in coaxial alignment with the stator. With the help of Labview ® programmable virtual signal processing software, the open-circuit voltage of four channels can be monitored at the same time. As shown in Figure 5.6a, the open-circuit voltage of four channels exhibits peaks in alternating contact between copper foil sector and bottom electrodes. An enlarged view in Figure 5.6 b displays an entire cycle of the voltage and corresponding positions among the four channels. The copper foil sector sliding towards the bottom electrode generates an increasing voltage peak, while sliding away causes a negative one, as sketched in Figure 5.5. The interval between neighboring negative peak and positive peak of 1st channel (L1) corresponds to one rotating cycle of the rotator. The negative peaks and positive peaks of 2nd channel (L2), 3rd channel (L3) and 4th channel (L4) will display 1, 2 and 4 times respectively within one cycle, which is corresponding to the copper foil sector patterned on the foam rotator. The open-circuit voltage switches between zero and the maximum value of 60 V as the pattern on the rotator repeatedly passes through the electrodes on the stator. The experimental results are fully consistent with the above theoretical analysis and numerical simulations.

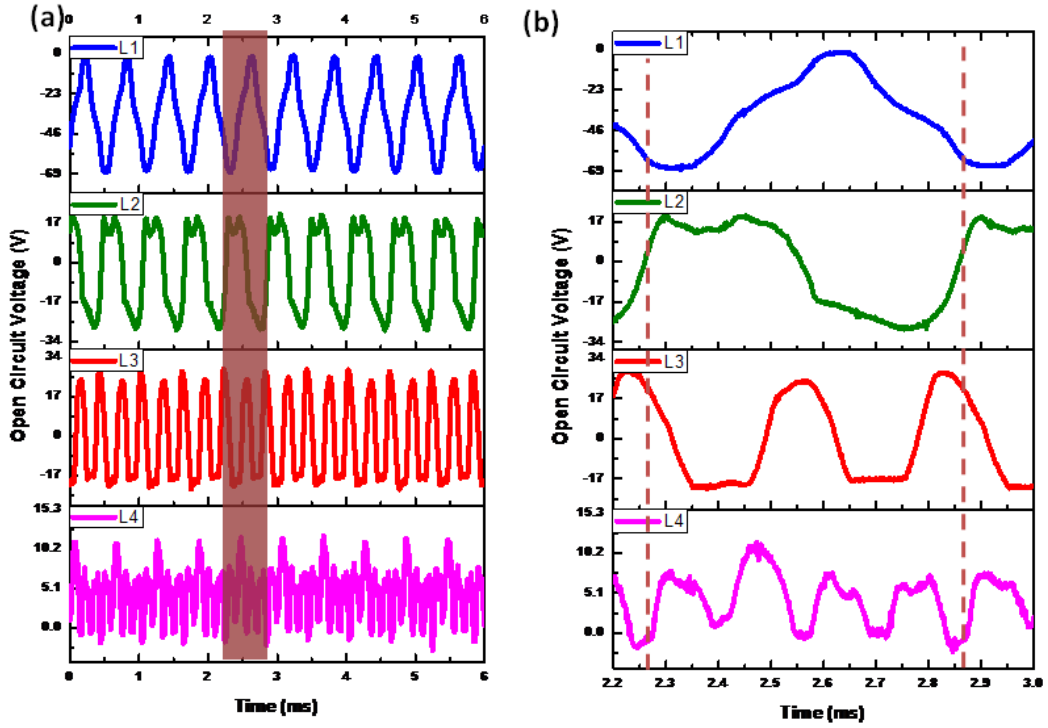

Figure 5. 6 Results of electric measurements. (a) Open-circuit voltage from 4 channels at a rotation rate of 100 r·min^{-1}(b) enlarged view of a cycle highlighted in (a).

The encoding of the four signals and its relationship with the angle is shown in Figure 5.7, in which Figure 5.7b shows an enlarged view of the dashed box in mixed 4 channel signal curves from Figure 5.7a. Each time point corresponds to a location of the rotator by reading out all the 4 voltage at the same time. When the output circuit voltage of each channel reaches a positive maximum the copper foil sector is aligned with the bottom electrode. Conversely, when the open-circuit voltage of each channel reaches negative maximum the carved sector is aligned with the bottom electrode. Combining all the output voltage signal of the four channels, the position of the rotator can be localized and the angular motion of the rotator can be determined. For example, when we define the angle status in Figure 5.7b-I as the initial angle, the output levels from L1 L3 and L4

are near negative peaks when L2 is on positive. Consequently, when the stator is rotated by 90° to Figure 5.7b-II, the signal reflects a different code with L1 L2 and L3 at their positive, while L4 is still negative.

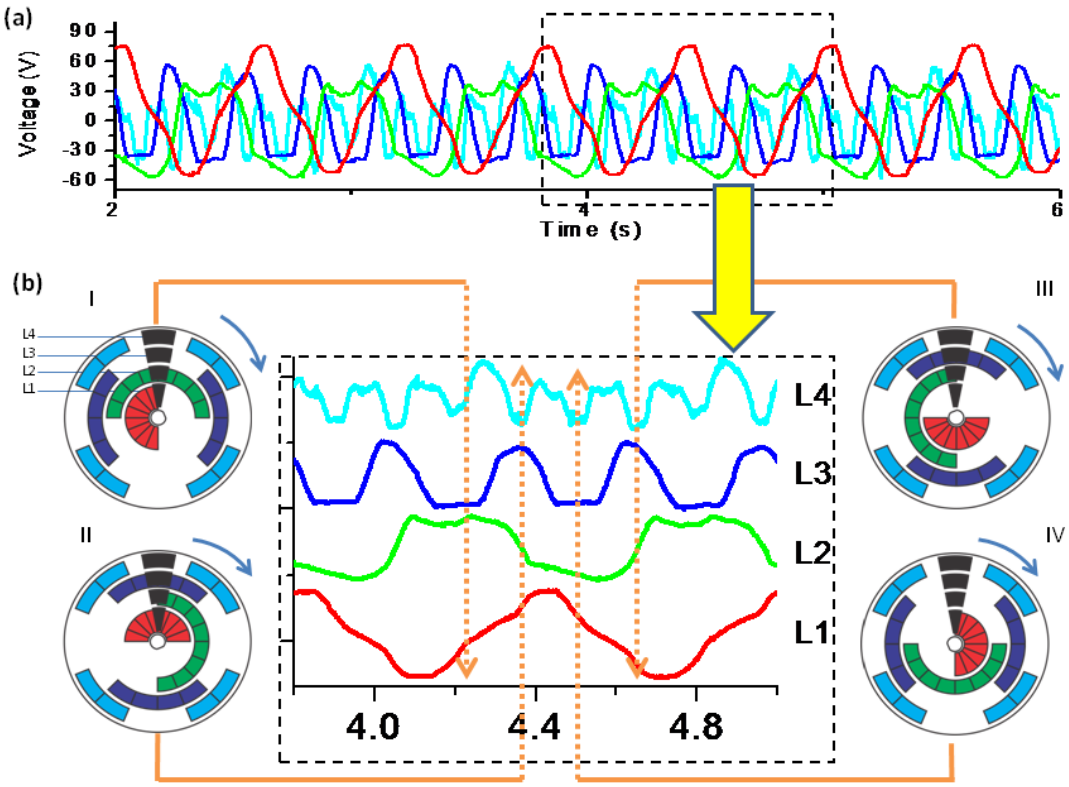

Figure 5. 7 Angular positons corresponding to signal status. (a) Simultaneous measurement results of output voltage from four channels (L1, L2, L3, L4). (b) Enlarged dash box area in (a).describing the processing results of output voltage from four channels (L1, L2, L3, L4) . The output voltages indicate the location of the rotator, corresponding to the decoded copper foil sector of the sensor. I-IV shows the rotator taking 90° rotation successively.

5.5 Acquire Angular Position by Signal Decoding

To demonstrate applications of the QS-TES for self-powered angular measurement, we mounted the sensor with the steering wheel together for monitoring and mapping the angle

of the steering wheel in real time. Figure 5.8a shows the self-powered angular measurement system. An external LED is connected between each channel electrode and the ground. When the steering wheel rotated, the external LED can be lighten and indicating the current position of each channel, as shown in Figure 5.8a II-V.

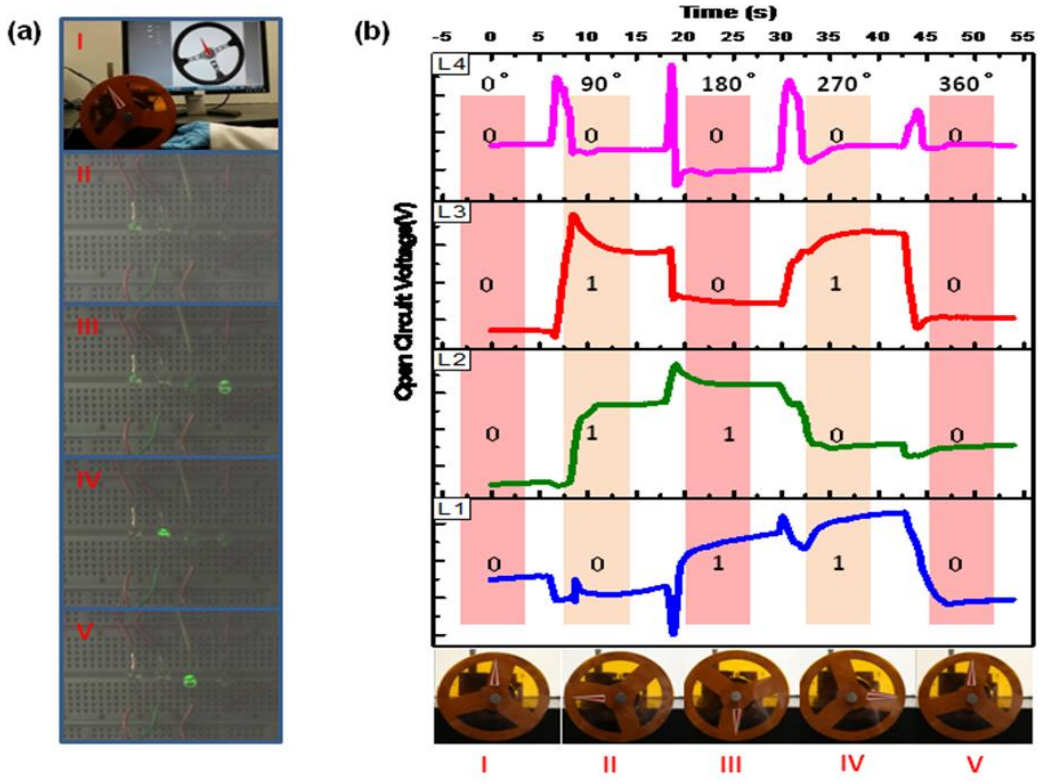

Figure 5. 8 Self-powered QS-TES-based angular monitoring system of steering wheel. (a) Optical image of the fabricated QS-TES angular monitoring system and the LED lighten by the self-powered angular monitoring system. (b) Measured output voltage and real-time location mapping when the steering wheel counter clockwise rotates to the (I)0°, (II)90°, (III) 180°(IV) 270 °and (V) 360°, the corresponding codes of output signal are '0000', '0110', '1100', '1010 ' and '0000', respectively.

In Figure. 5.8b, the open circuit voltage from the four channels were recorded when the steering wheel counter clockwise rotates for one cycle. One each 90° of rotation, the rotator rests for a while, leaving the signal a flat curve at current position. The output signal can be considered as high electrical level ('1') when the open-circuit voltage is larger than

the average voltage of each channel, and as low electrical level(‘0’) when the open-circuit voltage is smaller than the average voltage of each channel, respectively. The steering wheel rotates from the original position that corresponding to the carved sector, the output voltage of each channel is near to zero, which corresponds to the code ‘0000’ and shown in Figure 5.8b-I. when the steering wheel rotates counter clockwise to the nine clock direction, the corresponding alternating voltage of four channels were measured at the same time, which indicates a value of the 90 degree and code ‘0110’.The processing signal triggered the rotating of the steering wheel model, indicating the rotating angle of the steering wheel on the monitor. Figure 5.8b II-V shows the voltage signals and the digital mapping results when the steering wheel rotates to the six, three and twelve clock direction, which corresponding to the 180, 270 and 360 degree, respectively, and codes ‘1100’, ‘1010’ and ‘0000’, respectively. A full angle-signal decoding chart is displayed in Table 5.1. Therefore, the angular position of the steering wheel can be immediately exhibited and directly perceived from the coded information.

Table 5. 1 Angle-signal digital decoding chart.

FOUR DIGITAL	ANGLE（°）
0000	0 (360)
0001	22.5
0011	45
0010	67.5
0110	90
0111	112.5
0101	135
0100	157.5
1100	180
1101	202.5
1111	225
1110	247.5
1010	270
1011	292.5
1001	315
1000	337.5

5.6 Angular Velocity Sensing and Acceleration Sensing

5.6.1 Angular Velocity Measurement

Furthermore, the as-fabricated QS-TES can also be harnessed for angular speed measurement. Given a relationship between the voltage output and the rotating speed of QS-TES, the rotating speed can be calculated from the output voltage signal of one channel. Different rotating speed will lead to different periodical signal, thus, different frequency of the output voltage signal as shown in Equation 3.

$$\omega = 2\pi f \tag{3}$$

Figure 5.9 demonstrates the QS-TES acting as a self-powered sensor for rotating speed measurement. The open circuit voltages at different rotating speed are shown in Figure 5.9a-e. Experimental results show that the frequency of the open circuit voltage is a monotonically increasing function of the rotating speed as shown in Figure 5.9f.

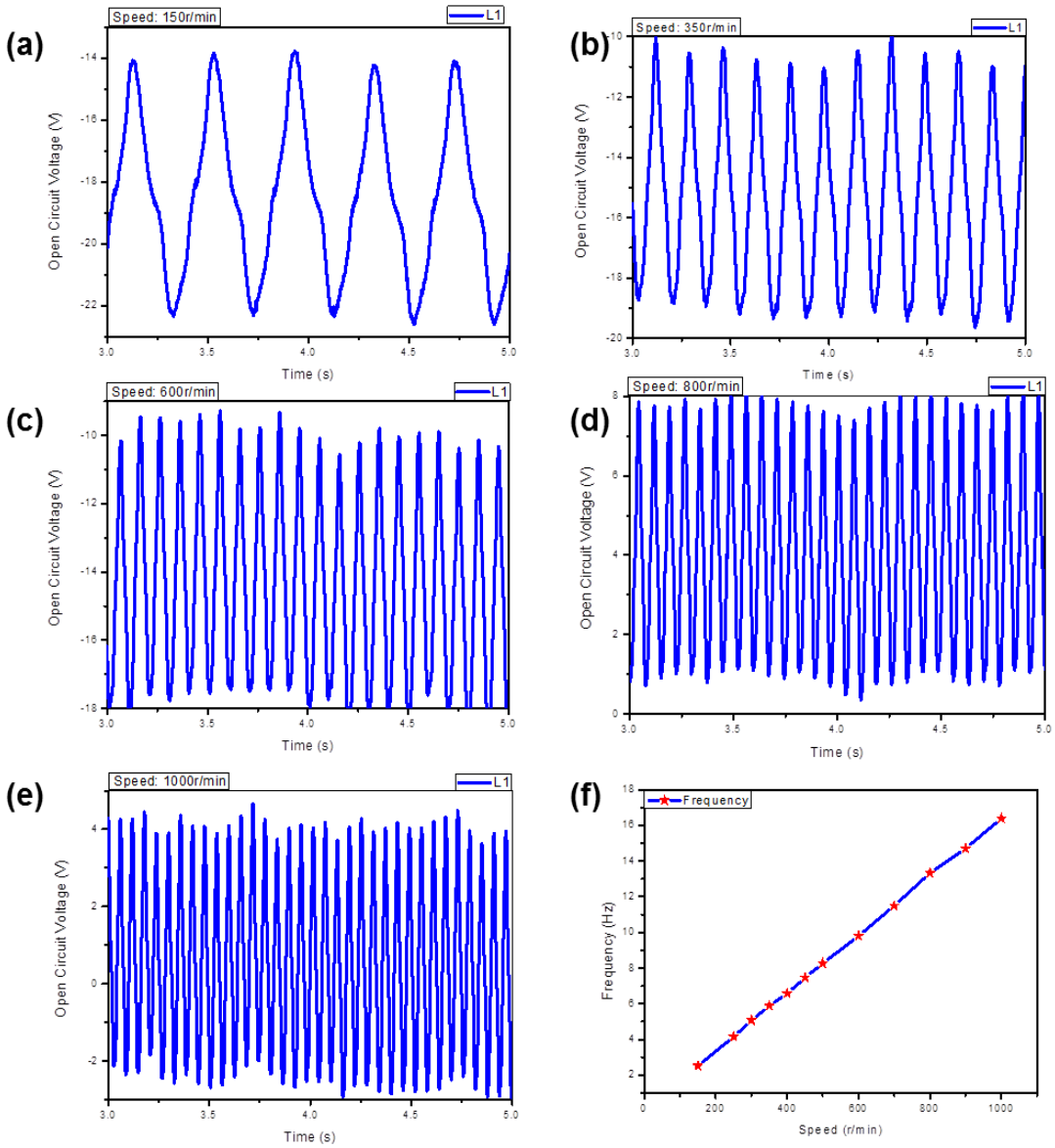

Figure 5. 9 Demonstration of the QS-TES acting as a self-powered sensor for speed measurement. Curve of open circuit voltage of one channel at speed of (a) 150 r·min^{-1}, (b) 350 r·min^{-1}, (c) 600 r·min^{-1}, (d) 800 r·min^{-1} and (e) 1000 r·min^{-1} are shown respectively. (f) Relationship between frequency and the speed. The rotating speed will influence the frequency of output voltage signal.

5.6.2 Angular Acceleration Measurement

Additionally, the as-fabricated QS-TES can be harnessed for angular acceleration measurement. The rotator of QS-TES can be divided into N sectors. The angular difference of neighbouring sectors is $\theta = 2\pi/\mathrm{N}$, if the time are ΔT_i and ΔT_{i+1} for the rotator rotating from *i*th sector to *(i*+1*)*th sector and from *(i*+1*)*th sector to *(i*+2*)*th sector, respectively, then the angular speeds are $\omega_1 = \theta/\Delta T_i$ and $\omega_2 = \theta/\Delta T_{i+1}$ for ΔT_i and ΔT_{i+1}, respectively. Thus, the angular acceleration from ΔT_i to ΔT_{i+1}, can be expressed as

$$\gamma_1 = \frac{2(\omega_2-\omega_1)}{(\Delta T_i+\Delta T_{i+1})} = \frac{2\theta(\Delta T_i-\Delta T_{i+1})}{\Delta T_i \Delta T_{i+1}(\Delta T_i+\Delta T_{i+1})} \tag{5.4}$$

Likewise, the angular acceleration from ΔT_{i+1} to ΔT_{i+2} is

$$\gamma_2 = \frac{2(\omega_3-\omega_2)}{(\Delta T_{i+1}+\Delta T_{i+2})} = \frac{2\theta(\Delta T_{i+2}-\Delta T_{i+1})}{\Delta T_{i+1} \Delta T_{i+2}(\Delta T_{i+1}+\Delta T_{i+2})} \tag{5.5}$$

and so on. The angular acceleration for one period from ΔT_{n-1} to ΔT_n can be expressed as:

$$\gamma_n = \frac{2(\omega_n-\omega_{n-1})}{(\Delta T_{n-1}+\Delta T_n)} = \frac{2\theta(\Delta T_n-\Delta T_{n-1})}{\Delta T_{n-1} \Delta T_n(\Delta T_{n-1}+\Delta T_n)} \tag{5.6}$$

where the ΔT_n can be acquired with the timing function in Labview program.

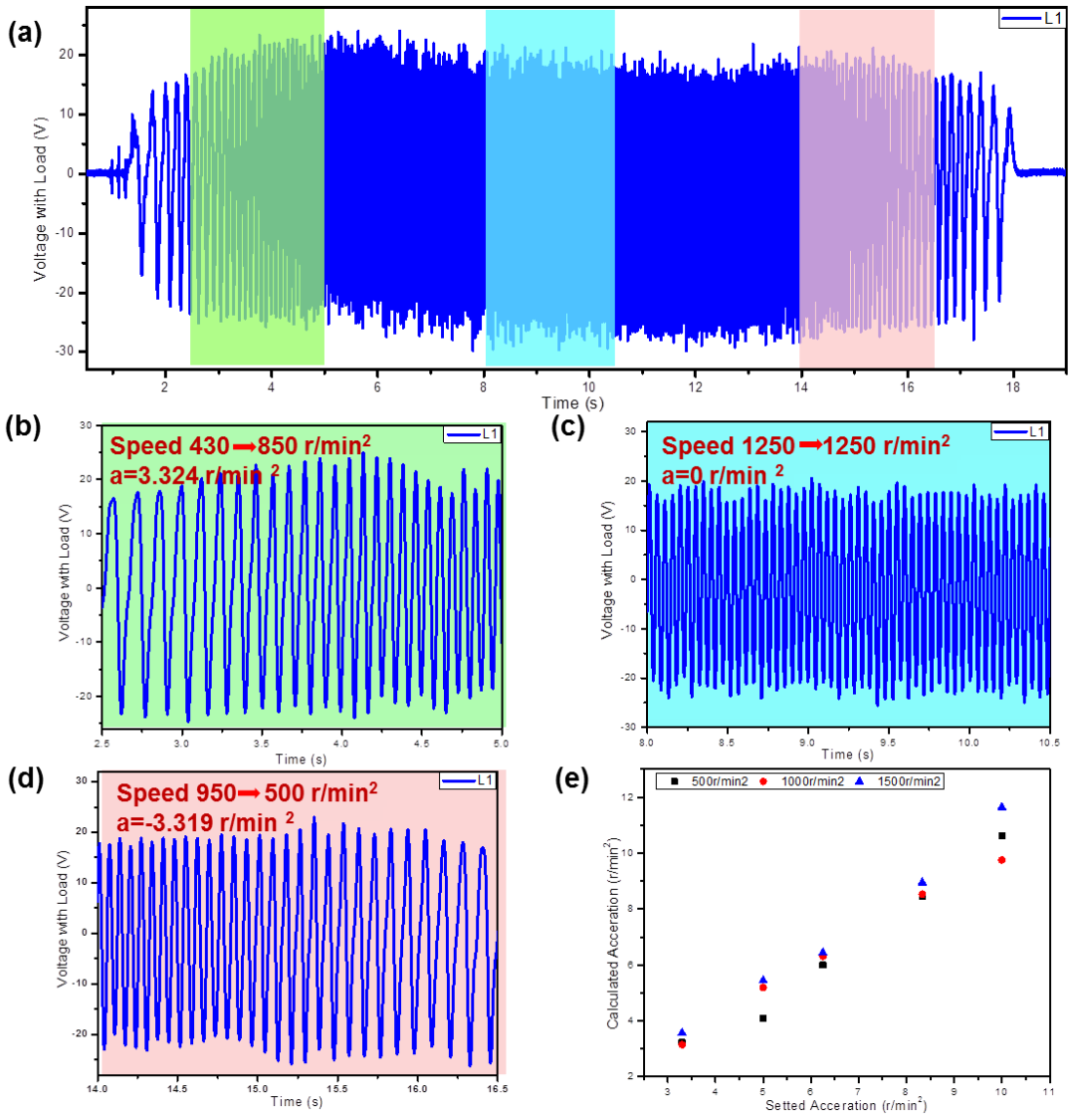

Figure 5. 10 Demonstration of the QS-TES acting as a self-powered sensor for acceleration measurement. Output voltage from one channel when the speed increase from 0 r·min^{-1} to 1250 r·min^{-1} with acceleration of 3.33 r·min^{-2} and speed decrease from 1250 r·min^{-1} to 0 r·min^{-1} with deceleration of -3.33 r·min^{-2}. Enlarged views of the cycles were shown in (b)-(d), corresponding to the three speed change phrases of the rotator, which is acceleration phrase (b), constant speed phrase (c) and deceleration phrase (d). (f) Relationship between set acceleration and calculated acceleration at different rotating speed.

The performance of QS-TES acting as a self-powered sensor for acceleration measurement is demonstrated in Figure 5.10. By increasing and decreasing the rotating

speed of the QS-TES with fixed rate from one speed to another, the output voltage measured by connecting an external resistance from one channel can be measured continuously as shown in Figure 7a. Enlarged views of the cycles from each phases are shown in Figure 5.10b-d, corresponding to the three speed change phases of the rotator, which is acceleration phrase, constant speed phrase and deceleration phrase. According to Equation 5.3 and 5.6, the speed and acceleration of the corresponding phrase can be calculated. The rotating speeds of the rotator were set as 500 $r \cdot min^{-1}$, 1000 $r \cdot min^{-1}$, 1500 $r \cdot min^{-1}$ respectively and the acceleration were set as 3.33 $r \cdot min^{-2}$, 5 $r \cdot min^{-2}$, 6.25 $r \cdot min^{-2}$, 8.33 $r \cdot min^{-2}$ and 10 $r \cdot min^{-2}$ by changing the running parameters of the motor mounted with the QS-TES. The curves indicating the relationship between the calculated acceleration and set acceleration can be acquired based on the measured output voltage, which is shown in Figure 5.10e.

5.7 Chapter Summary

In this work, we demonstrated a self-powered sensor for angular measurement using triboelectric effect. The sliding of a rotator along a stator leads to charge transfer between the copper bottom electrode and the ground, generating AC current peaks in the external circuit. By converting the mechanical rotation into electrical output signal, the sensor delivers an open-circuit voltage up to 60 V. An axial array of copper foil sectors of rotator enables the detection of angle. The angle can be monitored in real time by simultaneously reading the output voltage from different channels. Increasing the number of channels could refine the resolution for angular measurements. At the same time, the sensor can be used as a self-powered angular speed and angular acceleration sensor. This work reveals a great potential of sensing applications based on patterned triboelectric nanogenerator.

CHAPTER 6

DISCUSSIONS AND CONCLUSIONS

The increasing demand of electrical energy nowadays is encouraging researchers to develop a clean and sustainable approach by converting self-sustaining environmental energies into electricity. The rapid advent and popularity of small mobile devices (SMDs) such a cell phones, health monitors, sensors of all types, etc. provides a huge market and drive for the development of micro-meso environmental energy harvesters. In this dissertation, we describe one such harvester that harnesses environmental energy from the combined triboelectric and electrostatic effects and we have aptly named our device the triboelectric generator, To harvest the environmental energy, two materials with maximal difference in the triboelectric potentials are brought cyclically into and out-of-contacts. Triboelectric generators can be classified in accordance to their modes of energy generation; vertical-contact mode and lateral-sliding mode.

In addition to using the triboelectric generator as a harvester of environmental energy, we showed that it can also be used as a kinematic sensor. It can be reliably and sustainably employed for motion sensing, velocity sensing, acceleration sensing, etc. Other reported work has shown that it can also be sued for vibration sensing and chemical sensing.[72,82,83,106]

To significantly improve on the efficiency of our triboelectric generator, we introduced patterns into the design and we showed that the patterns also resulted in an additional functionality, which is to allow the triboelectric generator to act as a self-powered kinematic sensor. A good part of the dissertation was focused on generating pattern designs for an efficient energy harvester and for a speedy and accurate kinematic sensor.

We fabricated grating electrodes with an case-encapsulated design triboelectric generator (cTENG) for harvesting environmental energy from reciprocating motions. To mitigate the frictional effects, we introduced polytetrafluoroethylene (PTFE) nanoparticles to act as a lubricant. The cTENG produced an average effective output power of 12.2 mW over 140 kΩ external load at a sliding speed of 1 m/s, which corresponds to a power density of 1.36 W/m^2. We also demonstrated the use of cTENG to effectively harvest energy from human motions and oscillating water waves.

In our work, we also fabricated a dual-mode, self-powered velocity sensor for sensing linear and rotary motions. The pattern design adopted for this device is to employ alternating Kapton-copper strips arranged in a spiral configuration wrapped on the inner and outer surfaces of two concentric cylinders. This design allows voltage assays for linear and rotary motions to be measured and the triboelectric output signals when integrated with a digital circuit and a microcontroller unit can be directly processed into remarkably stable velocity information. Linear speeds of 0.1 ─ 0.6 ms^{-1} with an error < 0.5% and rotary speeds of 300 ─ 700 rpm with an error < 0.9%. We also discussed the measurement sensitivities and limitations of our device.

To sense directions, we employed a simultaneous monitoring of the dual channel signals from a double grating patterned triboelectric generator that is given a small phase difference. The kinematic vector sensor is fabricated using highly-pliable organic films to provide for a robust and self-powered sensing of positions, velocities, accelerations and their directions. The working principle is to source the environmental energy from a close-proximity triboelectrification of two surfaces, a mover and a stator in relative reciprocation. The mover consists of a thin polytetrafluoroethylene film coated with a 2-column array of copper electrodes placed at a quarter pitch offset to each other. The stator consists of a thin polyimide film with the top and bottom surfaces coated with a 2-column aligned array

of copper electrodes arranged such that the top and bottom arrays are shifted by half of a pitch to yield an alternating pattern. As the mover traverses over the stator, the electrodes in the mover actively generate electric signals of ±5 V to attain a peak power density of ≥ 65 mW/m^2 at a speed of 0.3 ms^{-1}. During our 86,000 sliding motion tests of kinematic measurements, the sensor showed excellent stability, repeatability and strong signal durability. The highly pliable sensor can be easily bent to spread over curved and uneven surfaces.

Adding an extra channel to the device allowed us to sense angles and in this work, we developed a 4 channel sliding triboelectric generator with an encoding pattern on the electrification surface. The planar structure consists of a rotator coated with a 4-channel coded copper foil and a stator with a fluorinated ethylenepropylene (FEP) film. Due to the interaction of the triboelectrification with the electrostatic induction, the sensor generates output signals in response to mechanical rotating motion of an object mounted with the sensor. The sensor is capable of reading and storing absolute angular kinematic quantities of positions, velocities and accelerations in real time. Under a rotational speed of 100 rad min^{-1}, the output voltage of the sensor attained a high of 60 V. Also, due to the relatively low threshold voltage of ±0.5 V for data processing, the robustness of the device is assured. The resolution of the sensor is 22.5° and can be further improved by increasing the number of channels.

The various triboelectric devices fabricated in this dissertation still face a lot of challenges and further research is being carried out to address them. Some of the toughest challenges are listed below.

1. The conflicting dilemma of increasing the sensing resolution and the consequent reduction of output decrement. The sensing resolution can be

improved by refining the grating structure; however, this results in a smaller output as the grating electrodes become thinner.

2. The sliding motion will invariably bring about wear and tear, which will affect the wearability of the sensor. Although PTFE nanoparticles were used as a lubricant in our work, we have not investigated the life-span of the nanoparticles with respect to the wearability of the sensor. Further, we applied the nanoparticles only in our reciprocating but not the rotary motions.
3. New materials with excellent surface properties need to be studied and introduced to the triboelectric generator, such as graphene, *etc*.
4. We have not fully addressed if the technologies developed in this dissertation can be used by the industry as issues such as reliability, cost, etc.
5. Expand the kinematic sensing to more complicated situations such as curved motions.

Despite these challenges, our pioneering demonstration of the applied triboelectric technologies will have a huge impact in the industrial commercialization of self-powered devices and sensors.

REFERENCES

1 St-Onge, M., Mignault, D., Allison, D. B. & Rabasa-Lhoret, R. Evaluation of a portable device to measure daily energy expenditure in free-living adults. *Am J Clin Nutr* **85**, 742-749 (2007).

2 Klingeberg, T. & Schilling, M. Mobile wearable device for long term monitoring of vital signs. *Comput Meth Prog Bio* **106**, 89-96 (2012).

3 Bar, A., Pillar, G., Dvir, I., Sheffy, J., Schnall, R. P. & Lavie, P. Evaluation of a portable device based on peripheral arterial tone for unattended home sleep studies. *Chest* **123**, 695-703 (2003).

4 Truman, T. E., Pering, T., Doering, R. & Brodersen, R. W. The InfoPad multimedia terminal: A portable device for wireless information access. *Ieee T Comput* **47**, 1073-1087 (1998).

5 Sack, S., Kahlert, P., Bilodeau, L., Pierard, L. A., Lancellotti, P., Legrand, V., Bartunek, J., Vanderheyden, M., Hoffmann, R., Schauerte, P., Shiota, T., Marks, D. S., Erbel, R. & Ellis, S. G. Percutaneous Transvenous Mitral Annuloplasty Initial Human Experience With a Novel Coronary Sinus Implant Device. *Circ-Cardiovasc Inte* **2**, 277-284 (2009).

6 Roessler, G., Laube, T., Brockmann, C., Kirschkamp, T., Mazinani, B., Goertz, M., Koch, C., Krisch, I., Sellhaus, B., Trieu, H. K., Weis, J., Bornfeld, N., Rothgen, H., Messner, A., Mokwa, W. & Walter, P. Implantation and Explantation of a Wireless Epiretinal Retina Implant Device: Observations during the EPIRET3 Prospective Clinical Trial. *Invest Ophth Vis Sci* **50**, 3003-3008 (2009).

7 Hill, J., Szewczyk, R., Woo, A., Hollar, S., Culler, D. & Pister, K. System architecture directions for networked sensors. *Acm Sigplan Notices* **35**, 93-104 (2000).

8 Pottie, G. J. & Kaiser, W. J. Wireless integrated network sensors. *Commun Acm* **43**, 51-58 (2000).

9 Bartle, A. Hydropower potential and development activities. *Energ Policy* **30**, 1231-1239 (2002).

10 Yazhou, L. Studies on wind farm integration into power system [J]. *Automation of Electric Power Systems* **8**, 017 (2003).

11 Datta, R. & Ranganathan, V. T. Variable-speed wind power generation using doubly fed wound rotor induction machine - A comparison with alternative schemes. *Ieee T Energy Conver* **17**, 414-421 (2002).

12 Barros, M. T. L., Tsai, F. T. C., Yang, S. L., Lopes, J. E. G. & Yeh, W. W. G. Optimization of large-scale hydropower system operations. *J Water Res Pl-Asce* **129**, 178-188 (2003).

13 Hennessey, J. P. Some Aspects of Wind Power Statistics. *J Appl Meteorol* **16**, 119-128 (1977).

14 Yang, W. Q., Chen, J., Zhu, G., Wen, X. N., Bai, P., Su, Y. J., Lin, Y. & Wang, Z. L. Harvesting vibration energy by a triple-cantilever based triboelectric nanogenerator. *Nano Res* **6**, 880-886 (2013).

15 Hu, Y. F., Zhang, Y., Xu, C., Lin, L., Snyder, R. L. & Wang, Z. L. Self-Powered System with Wireless Data Transmission. *Nano Letters* **11**, 2572-2577 (2011).

16 Xu, S., Hansen, B. J. & Wang, Z. L. Piezoelectric-nanowire-enabled power source for driving wireless microelectronics. *Nature Communications* **1** (2010).

17 Hu, Y. F., Zhang, Y., Xu, C., Zhu, G. A. & Wang, Z. L. High-Output Nanogenerator by Rational Unipolar Assembly of Conical Nanowires and Its Application for Driving a Small Liquid Crystal Display. *Nano Letters* **10**, 5025-5031 (2010).

18 Park, K. I., Xu, S., Liu, Y., Hwang, G. T., Kang, S. J. L., Wang, Z. L. & Lee, K. J. Piezoelectric BaTiO3 Thin Film Nanogenerator on Plastic Substrates. *Nano Letters* **10**, 4939-4943 (2010).

19 Lu, M. P., Song, J., Lu, M. Y., Chen, M. T., Gao, Y., Chen, L. J. & Wang, Z. L. Piezoelectric Nanogenerator Using p-Type ZnO Nanowire Arrays. *Nano Letters* **9**, 1223-1227 (2009).

20 Wang, Z. L. & Song, J. H. Piezoelectric nanogenerators based on zinc oxide nanowire arrays. *Science* **312**, 242-246 (2006).

21 Gao, P. X., Song, J. H., Liu, J. & Wang, Z. L. Nanowire piezoelectric nanogenerators on plastic substrates as flexible power sources for nanodevices. *Advanced Materials* **19**, 67-+ (2007).

22 Chen, X., Xu, S. Y., Yao, N. & Shi, Y. 1.6 V Nanogenerator for Mechanical Energy Harvesting Using PZT Nanofibers. *Nano Letters* **10**, 2133-2137 (2010).

23 Qin, Y., Wang, X. D. & Wang, Z. L. Microfibre-nanowire hybrid structure for energy scavenging. *Nature* **451**, 809-U805 (2008).

24 Lin, L., Xie, Y. N., Wang, S. H., Wu, W. Z., Niu, S. M., Wen, X. N. & Wang, Z. L. Triboelectric Active Sensor Array for Self-Powered Static and Dynamic Pressure Detection and Tactile Imaging. *Acs Nano* **7**, 8266-8274 (2013).

25 Lee, S., Bae, S. H., Lin, L., Yang, Y., Park, C., Kim, S. W., Cha, S. N., Kim, H., Park, Y. J. & Wang, Z. L. Super-Flexible Nanogenerator for Energy Harvesting from Gentle Wind and as an Active Deformation Sensor. *Advanced Functional Materials* **23**, 2445-2449 (2013).

26 Fan, F. R., Tian, Z. Q. & Wang, Z. L. Flexible triboelectric generator! *Nano Energy* **1**, 328-334 (2012).

27 Fan, F. R., Lin, L., Zhu, G., Wu, W. Z., Zhang, R. & Wang, Z. L. Transparent Triboelectric Nanogenerators and Self-Powered Pressure Sensors Based on Micropatterned Plastic Films. *Nano Letters* **12**, 3109-3114 (2012).

28 Wang, S. H., Lin, L. & Wang, Z. L. Nanoscale Triboelectric-Effect-Enabled Energy Conversion for Sustainably Powering Portable Electronics. *Nano Letters* **12**, 6339-6346 (2012).

29 Zhu, G., Pan, C. F., Guo, W. X., Chen, C. Y., Zhou, Y. S., Yu, R. M. & Wang, Z. L. Triboelectric-Generator-Driven Pulse Electrodeposition for Micropatterning. *Nano Letters* **12**, 4960-4965 (2012).

30 Wang, Z. L. Triboelectric Nanogenerators as New Energy Technology for Self-Powered Systems and as Active Mechanical and Chemical Sensors. *Acs Nano* **7**, 9533-9557 (2013).

31 Wang, Z. L., Zhu, G., Yang, Y., Wang, S. H. & Pan, C. F. Progress in nanogenerators for portable electronics. *Mater Today* **15**, 532-543 (2012).

32 Lee, M., Chen, C. Y., Wang, S., Cha, S. N., Park, Y. J., Kim, J. M., Chou, L. J. & Wang, Z. L. A Hybrid Piezoelectric Structure for Wearable Nanogenerators. *Advanced Materials* **24**, 1759-1764 (2012).

33 Yang, Y., Lin, L., Zhang, Y., Jing, Q. S., Hou, T. C. & Wang, Z. L. Self-Powered Magnetic Sensor Based on a Triboelectric Nanogenerator. *Acs Nano* **6**, 10378-10383 (2012).

34 Zhang, R., Lin, L., Jing, Q. S., Wu, W. Z., Zhang, Y., Jiao, Z. X., Yan, L., Han, R. P. S. & Wang, Z. L. Nanogenerator as an active sensor for vortex capture and ambient wind-velocity detection. *Energ Environ Sci* **5**, 8528-8533 (2012).

35 Yang, Y., Zhu, G., Zhang, H. L., Chen, J., Zhong, X. D., Lin, Z. H., Su, Y. J., Bai, P., Wen, X. N. & Wang, Z. L. Triboelectric Nanogenerator for Harvesting Wind Energy and as Self-Powered Wind Vector Sensor System. *Acs Nano* **7**, 9461-9468 (2013).

36 Ulaby, F. T. Fundamentals of applied electromagnetics. *2001 media edn, (Prentice Hall, 2001)*.

37 Beeby, S. P., Torah, R. N., Tudor, M. J., Glynne-Jones, P., O'Donnell, T., Saha, C. R. & Roy, S. A micro electromagnetic generator for vibration energy harvesting. *J Micromech Microeng* **17**, 1257-1265 (2007).

38 Williams, C. B., Shearwood, C., Harradine, M. A., Mellor, P. H., Birch, T. S. & Yates, R. B. Development of an electromagnetic micro-generator. *Iee P-Circ Dev Syst* **148**, 337-342 (2001).

39 Arnold, D. P. Review of microscale magnetic power generation. *Ieee T Magn* **43**, 3940-3951 (2007).

40 El-hami, M., Glynne-Jones, P., White, N. M., Hill, M., Beeby, S., James, E., Brown, A. D. & Ross, J. N. Design and fabrication of a new vibration-based electromechanical power generator. *Sensor Actuat a-Phys* **92**, 335-342 (2001).

41 Glynne-Jones, P., Tudor, M. J., Beeby, S. P. & White, N. M. An electromagnetic, vibration-powered generator for intelligent sensor systems. *Sensor Actuat a-Phys* **110**, 344-349 (2004).

42 Kulkarni, S., Koukharenko, E., Torah, R., Tudor, J., Beeby, S., O'Donnell, T. & Roy, S. Design, fabrication and test of integrated micro-scale vibration-based electromagnetic generator. *Sensor Actuat a-Phys* **145**, 336-342 (2008).

43 Keawboonchuay, C. & Engel, T. G. Electrical power generation characteristics of piezoelectric generator under quasi-static and dynamic stress conditions. *Ieee T Ultrason Ferr* **50**, 1377-1382 (2003).

44 Xu, S., Wei, Y. G., Liu, J., Yang, R. & Wang, Z. L. Integrated Multilayer Nanogenerator Fabricated Using Paired Nanotip-to-Nanowire Brushes. *Nano Letters* **8**, 4027-4032 (2008).

45 Yang, R., Qin, Y., Li, C., Zhu, G. & Wang, Z. L. Converting Biomechanical Energy into Electricity by a Muscle-Movement-Driven Nanogenerator. *Nano Letters* **9**, 1201-1205 (2009).

46 Zhu, G. A., Yang, R. S., Wang, S. H. & Wang, Z. L. Flexible High-Output Nanogenerator Based on Lateral ZnO Nanowire Array. *Nano Letters* **10**, 3151-3155 (2010).

47 Zhu, G., Wang, A. C., Liu, Y., Zhou, Y. S. & Wang, Z. L. Functional Electrical Stimulation by Nanogenerator with 58 V Output Voltage. *Nano Letters* **12**, 3086-3090 (2012).

48 Lowell, J. & Roseinnes, A. C. Contact Electrification. *Adv Phys* **29**, 947-1023 (1980).

49 Davies, D. K. Charge Generation on Dielectric Surfaces. *J Phys D Appl Phys* **2**, 1533-& (1969).

50 Zhu, G., Lin, Z. H., Jing, Q. S., Bai, P., Pan, C. F., Yang, Y., Zhou, Y. S. & Wang, Z. L. Toward Large-Scale Energy Harvesting by a Nanoparticle-Enhanced Triboelectric Nanogenerator. *Nano Letters* **13**, 847-853 (2013).

51 Wang, S. H., Lin, L., Xie, Y. N., Jing, Q. S., Niu, S. M. & Wang, Z. L. Sliding-Triboelectric Nanogenerators Based on In-Plane Charge-Separation Mechanism. *Nano Letters* **13**, 2226-2233 (2013).

52 Zhu, G., Chen, J., Liu, Y., Bai, P., Zhou, Y. S., Jing, Q. S., Pan, C. F. & Wang, Z. L. Linear-Grating Triboelectric Generator Based on Sliding Electrification. *Nano Letters* **13**, 2282-2289 (2013).

53 Xie, Y. N., Wang, S. H., Lin, L., Jing, Q. S., Lin, Z. H., Niu, S. M., Wu, Z. Y. & Wang, Z. L. Rotary Triboelectric Nanogenerator Based on a Hybridized Mechanism for Harvesting Wind Energy. *Acs Nano* **7**, 7119-7125 (2013).

54 Yang, Y., Zhang, H. L., Chen, J., Jing, Q. S., Zhou, Y. S., Wen, X. N. & Wang, Z. L. Single-Electrode-Based Sliding Triboelectric Nanogenerator for Self-Powered Displacement Vector Sensor System. *Acs Nano* **7**, 7342-7351 (2013).

55 Wang, S. H., Xie, Y. N., Niu, S. M., Lin, L. & Wang, Z. L. Freestanding Triboelectric-Layer-Based Nanogenerators for Harvesting Energy from a Moving Object or Human Motion in Contact and Non-contact Modes. *Advanced Materials* **26**, 2818-2824 (2014).

56 Bai, P., Zhu, G., Lin, Z. H., Jing, Q. S., Chen, J., Zhang, G., Ma, J. & Wang, Z. L. Integrated Multi layered Triboelectric Nanogenerator for Harvesting Biomechanical Energy from Human Motions. *Acs Nano* **7**, 3713-3719 (2013).

57 Bai, P., Zhu, G., Liu, Y., Chen, J., Jing, Q. S., Yang, W. Q., Ma, J. S., Zhang, G. & Wang, Z. L. Cylindrical Rotating Triboelectric Nanogenerator. *Acs Nano* **7**, 6361-6366 (2013).

58 Lin, L., Wang, S. H., Xie, Y. N., Jing, Q. S., Niu, S. M., Hu, Y. F. & Wang, Z. L. Segmentally Structured Disk Triboelectric Nanogenerator for Harvesting Rotational Mechanical Energy. *Nano Letters* **13**, 2916-2923 (2013).

59 Zhu, G., Chen, J., Zhang, T. J., Jing, Q. S. & Wang, Z. L. Radial-arrayed rotary electrification for high performance triboelectric generator. *Nature Communications* **5** (2014).

60 Li, X. J. & Meijer, G. C. M. A novel low-cost noncontact resistive potentiometric sensor for the measurement of low speeds. *Ieee T Instrum Meas* **47**, 776-781 (1998).

61 Brasseur, G. Robust capacitive angular position sensor. *IEEE Instrumentation and Measurement Technology Conference* **2**, 1081-1086 (1996).

62 Dibbern, U. Sensors Based on the Magnetoresistive Effect. *Sensor Actuator* **4**, 221-227 (1983).

63 Hylton, T. L. Limitations of Magnetoresistive Sensors Based on the Giant Magnetoresistive Effect in Granular Magnetic Composites. *Appl Phys Lett* **62**, 2431-2433 (1993).

64 Zabler, E., Heintz, F., Dietz, R. & Gerlach, G. Mechatronic Sensors in Integrated Vehicle Architecture. *Sensor Actuat a-Phys* **31**, 54-59 (1992).

65 Kadhim, A. H., Babu, T. K. M. & Okelly, D. Measurement of Steady-State and Transient Load-Angle, Angular Velocity, and Acceleration Using an Optical Encoder. *Ieee T Instrum Meas* **41**, 486-489 (1992).

66 Andermo, I., Shimomura, T., Kiriyama, T. & Yamaguchi, Y. An Absolute Linear Encoder Utilizing a Combination of Capacitive and Optical Encoder Technology. *Int J Jpn S Prec Eng* **29**, 14-17 (1995).

67 Engelhardt, K. & Seitz, P. Absolute, high-resolution optical position encoder. *Appl Optics* **35**, 201-208 (1996).

68 Li, X. J., Meijer, G. C. M. & deJong, G. W. A microcontroller-based self-calibration technique for a smart capacitive angular-position sensor. *Ieee T Instrum Meas* **46**, 888-892 (1997).

69 Gasulla, M., Li, X. J., Meijer, G. C. M., van der Ham, L. & Spronck, J. W. A contactless capacitive angular-position sensor. *Ieee Sens J* **3**, 607-614 (2003).

70 Hu, Y. F., Xu, C., Zhang, Y., Lin, L., Snyder, R. L. & Wang, Z. L. A Nanogenerator for Energy Harvesting from a Rotating Tire and its Application as a Self-Powered Pressure/Speed Sensor. *Advanced Materials* **23**, 4068-+ (2011).

71 Lin, L., Hu, Y. F., Xu, C., Zhang, Y., Zhang, R., Wen, X. N. & Wang, Z. L. Transparent flexible nanogenerator as self-powered sensor for transportation monitoring. *Nano Energy* **2**, 75-81 (2013).

72 Chen, J., Zhu, G., Yang, W. Q., Jing, Q. S., Bai, P., Yang, Y., Hou, T. C. & Wang, Z. L. Harmonic-Resonator-Based Triboelectric Nanogenerator as a Sustainable Power Source and a Self-Powered Active Vibration Sensor. *Advanced Materials* **25**, 6094-6099 (2013).

73 Yang, Y., Zhang, H. L., Zhong, X. D., Yi, F., Yu, R. M., Zhang, Y. & Wang, Z. L. Electret Film-Enhanced Triboelectric Nanogenerator Matrix for Self-Powered Instantaneous Tactile Imaging. *Acs Applied Materials & Interfaces* **6**, 3680-3688 (2014).

74 Hu, Y. F., Yang, J., Jing, Q. S., Niu, S. M., Wu, W. Z. & Wang, Z. L. Triboelectric Nanogenerator Built on Suspended 3D Spiral Structure as Vibration and Positioning Sensor and Wave Energy Harvester. *Acs Nano* **7**, 10424-10432 (2013).

75 Niu, S. M., Liu, Y., Wang, S. H., Lin, L., Zhou, Y. S., Hu, Y. F. & Wang, Z. L. Theory of Sliding-Mode Triboelectric Nanogenerators. *Advanced Materials* **25**, 6184-6193 (2013).

76 Yu, A., Song, M., Zhang, Y., Zhang, Y., Chen, L., Zhai, J. & Wang, Z. L. Self-powered acoustic source locator in underwater environment based on organic film triboelectric nanogenerator. *Nano Res*, 1-9 (2014).

77 Yang, J., Chen, J., Liu, Y., Yang, W. Q., Su, Y. J. & Wang, Z. L. Triboelectrification-Based Organic Film Nanogenerator for Acoustic Energy Harvesting and Self-Powered Active Acoustic Sensing. *Acs Nano* **8**, 2649-2657 (2014).

78 Yang, W. Q., Chen, J., Wen, X. N., Jing, Q. S., Yang, J., Su, Y. J., Zhu, G., Wu, W. Z. & Wang, Z. L. Triboelectrification Based Motion Sensor for Human-Machine Interfacing. *Acs Applied Materials & Interfaces* **6**, 7479-7484 (2014).

79 Zhang, H. L., Yang, Y., Su, Y. J., Chen, J., Adams, K., Lee, S., Hu, C. G. & Wang, Z. L. Triboelectric Nanogenerator for Harvesting Vibration Energy in Full Space and as Self- Powered Acceleration Sensor. *Advanced Functional Materials* **24**, 1401-1407 (2014).

80 Zhu, G., Yang, W. Q., Zhang, T. J., Jing, Q. S., Chen, J., Zhou, Y. S., Bai, P. & Wang, Z. L. Self-Powered, Ultrasensitive, Flexible Tactile Sensors Based on Contact Electrification. *Nano Letters* **14**, 3208-3213 (2014).

81 Yang, Y., Zhang, H. L., Lin, Z. H., Zhou, Y. S., Jing, Q. S., Su, Y. J., Yang, J., Chen, J., Hu, C. G. & Wang, Z. L. Human Skin Based Triboelectric Nanogenerators for Harvesting Biomechanical Energy and as Self-Powered Active Tactile Sensor System. *Acs Nano* **7**, 9213-9222 (2013).

82 Lin, Z. H., Xie, Y. N., Yang, Y., Wang, S. H., Zhu, G. & Wang, Z. L. Enhanced Triboelectric Nanogenerators and Triboelectric Nanosensor Using Chemically Modified TiO2 Nanomaterials. *Acs Nano* **7**, 4554-4560 (2013).

83 Lin, Z. H., Zhu, G., Zhou, Y. S., Yang, Y., Bai, P., Chen, J. & Wang, Z. L. A Self-Powered Triboelectric Nanosensor for Mercury Ion Detection. *Angew Chem Int Edit* **52**, 5065-5069 (2013).

84 Leland, E. S. & Wright, P. K. Resonance tuning of piezoelectric vibration energy scavenging generators using compressive axial preload. *Smart Mater Struct* **15**, 1413-1420 (2006).

85 Challa, V. R., Prasad, M. G., Shi, Y. & Fisher, F. T. A vibration energy harvesting device with bidirectional resonance frequency tunability. *Smart Mater Struct* **17** (2008).

86 Du, W. M., Han, X., Lin, L., Chen, M. X., Li, X. Y., Pan, C. F. & Wang, Z. L. A Three Dimensional Multi-Layered Sliding Triboelectric Nanogenerator. *Adv Energy Mater* **4** (2014).

87 Xie, Y. N., Wang, S. H., Niu, S. M., Lin, L., Jing, Q. S., Su, Y. J., Wu, Z. Y. & Wang, Z. L. Multi-layered disk triboelectric nanogenerator for harvesting hydropower. *Nano Energy* **6**, 129-136 (2014).

88 Jing, Q., Zhu, G., Bai, P., Xie, Y., Chen, J., Han, R. P. & Wang, Z. L. Case-encapsulated triboelectric nanogenerator for harvesting energy from reciprocating sliding motion. *ACS nano* **8**, 3836-3842 (2014).

89 Castle, G. S. P. Contact charging between insulators. *J Electrostat* **40-1**, 13-20 (1997).

90 Lungu, M. H. Electrical separation of plastic materials using the triboelectric effect. *Miner Eng* **17**, 69-75 (2004).

91 Persano, L., Dagdeviren, C., Su, Y. W., Zhang, Y. H., Girardo, S., Pisignano, D., Huang, Y. G. & Rogers, J. A. High performance piezoelectric devices based on aligned arrays of nanofibers of poly(vinylidenefluoride-co-trifluoroethylene). *Nature Communications* **4** (2013).

92 Jing, Q., Zhu, G., Wu, W., Bai, P., Xie, Y., Han, R. P. & Wang, Z. L. Self-powered triboelectric velocity sensor for dual-mode sensing of rectified linear and rotary motions. *Nano Energy* **10**, 305-312 (2014).

93 Chen, M. X., Li, X. Y., Lin, L., Du, W. M., Han, X., Zhu, J., Pan, C. F. & Wang, Z. L. Triboelectric Nanogenerators as a Self-Powered Motion Tracking System. *Advanced Functional Materials* **24**, 5059-5066 (2014).

94 Su, Y. J., Zhu, G., Yang, W. Q., Yang, J., Chen, J., Jing, Q. S., Wu, Z. M., Jiang, Y. D. & Wang, Z. L. Triboelectric Sensor for Self-Powered Tracking of Object Motion inside Tubing. *Acs Nano* **8**, 3843-3850 (2014).

95 Yi, F., Lin, L., Niu, S. M., Yang, J., Wu, W. Z., Wang, S. H., Liao, Q. L., Zhang, Y. & Wang, Z. L. Self-Powered Trajectory, Velocity, and Acceleration Tracking of a Moving Object/Body using a Triboelectric Sensor. *Advanced Functional Materials* **24**, 7488-7494 (2014).

96 Han, C. B., Zhang, C., Li, X. H., Zhang, L. M., Zhou, T., Hu, W. G. & Wang, Z. L. Self-powered velocity and trajectory tracking sensor array made of planar triboelectric nanogenerator pixels. *Nano Energy* **9**, 325-333 (2014).

97 Niu, S. M., Liu, Y., Wang, S. H., Lin, L., Zhou, Y. S., Hu, Y. F. & Wang, Z. L. Theoretical Investigation and Structural Optimization of Single-Electrode Triboelectric Nanogenerators. *Advanced Functional Materials* **24**, 3332-3340 (2014).

98 Luan, L., Evans, R. D., Jokerst, N. M. & Fair, R. B. Integrated optical sensor in a digital microfluidic platform. *Ieee Sens J* **8**, 628-635 (2008).

99 Ciminelli, C., Dell'Olio, F., Campanella, C. E. & Armenise, M. N. Photonic technologies for angular velocity sensing. *Adv Opt Photonics* **2**, 370-404 (2010).

100 Zhang, X. D., Kang, L. Y. & F., D. W. The principle of the potentiometer and its applications in the vehicle steering. *2005. IEEE International Conference on Vehicular Electronics and Safety*, 20 - 24 (2005).

101 Hoang, H. V. & Jeon, J. W. An Efficient Approach to Correct the Signals and Generate High-Resolution Quadrature Pulses for Magnetic Encoders. *Ieee T Ind Electron* **58**, 3634-3646 (2011).

102 Zhang, Z. J., Ni, F. L., Dong, Y. Y., Jin, M. H. & Liu, H. A novel absolute angular position sensor based on electromagnetism. *Sensor Actuat a-Phys* **194**, 196-203 (2013).

103 Culshaw, B. & Giles, I. in *Fibre Optics' 83.* 183-195 (International Society for Optics and Photonics).

104 Alper, S. E. & Akin, T. A single-crystal silicon symmetrical and decoupled MEMS gyroscope on an insulating substrate. *Microelectromechanical Systems, Journal of* **14**, 707-717 (2005).

105 Wu, Y., Jing, Q., Chen, J., Bai, P., Bai, J., Zhu, G., Su, Y. & Wang, Z. L. A Self‐Powered Angle Measurement Sensor Based on Triboelectric Nanogenerator. *Advanced Functional Materials* (2015).

106 Zhang, H. L., Yang, Y., Su, Y. J., Chen, J., Hu, C. G., Wu, Z. K., Liu, Y., Wong, C. P., Bando, Y. & Wang, Z. L. Triboelectric nanogenerator as self-powered active sensors for detecting liquid/gaseous water/ethanol. *Nano Energy* **2**, 693-701 (2013).

PERSONAL PUBLISHED WORKS

Below lists my personal published works (PW).

PW 1 ***Jing, Q.***, Zhu, G., Bai, P., Xie, Y., Chen, J., Han, R. P. & Wang, Z. L. Case-encapsulated triboelectric nanogenerator for harvesting energy from reciprocating sliding motion. *ACS nano* **8**, 3836-3842 (2014).

PW 2 ***Jing, Q.***, Zhu, G., Wu, W., Bai, P., Xie, Y., Han, R. P. & Wang, Z. L. Self-powered triboelectric velocity sensor for dual-mode sensing of rectified linear and rotary motions. *Nano Energy* **10**, 305-312 (2014).

PW 3 Wu, Y., ***Jing, Q.*** **(Co-first Author)**, Chen, J., Bai, P., Bai, J., Zhu, G., Su, Y. & Wang, Z. L. A Self-Powered Angle Measurement Sensor Based on Triboelectric Nanogenerator. *Advanced Functional Materials* (2015).

PW 4 Lin, L., ***Jing, Q.***, Zhang, Y., Hu, Y., Wang, S., Bando, Y., Han, R. P. & Wang, Z. L. An elastic-spring-substrated nanogenerator as an active sensor for self-powered balance. *Energ Environ Sci* **6**, 1164-1169 (2013).

PW 5 Ye, S., ***Jing, Q.*** & Han, R. P. A room-temperature non-volatile CNT-based molecular memory cell. *Journal of Applied Physics* **113**, 144302 (2013).

PW 6 Yang, Y., Pradel, K. C., ***Jing, Q.***, Wu, J. M., Zhang, F., Zhou, Y., Zhang, Y. & Wang, Z. L. Thermoelectric nanogenerators based on single Sb-doped ZnO micro/nanobelts. *ACS nano* **6**, 6984-6989 (2012).

PW 7 Zhang, R., Lin, L., ***Jing, Q.***, Wu, W., Zhang, Y., Jiao, Z., Yan, L., Han, R. P. & Wang, Z. L. Nanogenerator as an active sensor for vortex capture and ambient wind-velocity detection. *Energ Environ Sci* **5**, 8528-8533 (2012).

PW 8 Hu, Y., Yang, J., ***Jing, Q.***, Niu, S., Wu, W. & Wang, Z. L. Triboelectric nanogenerator built on suspended 3D spiral structure as vibration and positioning sensor and wave energy harvester. *ACS nano* **7**, 10424-10432 (2013).

PW 9 Zhu, G., Lin, Z.-H., ***Jing, Q.***, Bai, P., Pan, C., Yang, Y., Zhou, Y. & Wang, Z. L. Toward large-scale energy harvesting by a nanoparticle-enhanced triboelectric nanogenerator. *Nano letters* **13**, 847-853 (2013).

PW 10 Bai, P., Zhu, G., ***Jing, Q.***, Yang, J., Chen, J., Su, Y., Ma, J., Zhang, G. & Wang, Z. L. Membrane-Based Self-Powered Triboelectric Sensors for Pressure Change Detection and Its Uses in Security Surveillance and Healthcare Monitoring. *Advanced Functional Materials* **24**, 5807-5813 (2014).

PW 11 Wen, X., Yang, W., ***Jing, Q.*** & Wang, Z. L. Harvesting Broadband Kinetic Impact Energy from Mechanical Triggering/Vibration and Water Waves. *ACS nano* **8**, 7405-7412 (2014).

PW 12 Yang, W., Chen, J., ***Jing, Q.***, Yang, J., Wen, X., Su, Y., Zhu, G., Bai, P. & Wang, Z. L. 3D Stack Integrated Triboelectric Nanogenerator for Harvesting Vibration Energy. *Advanced Functional Materials* **24**, 4090-4096 (2014).

PW 13 Bai, P., Zhu, G., ***Jing, Q.***, Wu, Y., Yang, J., Chen, J., Ma, J., Zhang, G. & Wang, Z. L. Transparent and flexible barcode based on sliding electrification for self-powered identification systems. *Nano Energy* (2015).

PW 14 Yang, Y., Lin, L., Zhang, Y., ***Jing, Q.***, Hou, T.-C. & Wang, Z. L. Self-powered magnetic sensor based on a triboelectric nanogenerator. *ACS nano* **6**, 10378-10383 (2012).

PW 15 Bai, P., Zhu, G., Lin, Z.-H., ***Jing, Q.***, Chen, J., Zhang, G., Ma, J. & Wang, Z. L. Integrated multilayered triboelectric nanogenerator for harvesting biomechanical energy from human motions. *ACS Nano* **7**, 3713-3719 (2013).

PW 16 Bai, P., Zhu, G., Liu, Y., Chen, J., ***Jing, Q.***, Yang, W., Ma, J., Zhang, G. & Wang, Z. L. Cylindrical rotating triboelectric nanogenerator. *ACS nano* **7**, 6361-6366 (2013).

PW 17 Chen, J., Zhu, G., Yang, W., ***Jing, Q.***, Bai, P., Yang, Y., Hou, T. C. & Wang, Z. L. Harmonic-Resonator-Based Triboelectric Nanogenerator as a Sustainable Power Source and a Self-Powered Active Vibration Sensor. *Advanced Materials* **25**, 6094-6099 (2013).

PW 18 Lin, L., Wang, S., Xie, Y., ***Jing, Q.***, Niu, S., Hu, Y. & Wang, Z. L. Segmentally structured disk triboelectric nanogenerator for harvesting rotational mechanical energy. *Nano letters* **13**, 2916-2923 (2013).

PW 19 Wang, S., Lin, L., Xie, Y., ***Jing, Q.***, Niu, S. & Wang, Z. L. Sliding-triboelectric nanogenerators based on in-plane charge-separation mechanism. *Nano letters* **13**, 2226-2233 (2013).

PW 20 Xie, Y., Wang, S., Lin, L., ***Jing, Q.***, Lin, Z.-H., Niu, S., Wu, Z. & Wang, Z. L. Rotary triboelectric nanogenerator based on a hybridized mechanism for harvesting wind energy. *ACS nano* **7**, 7119-7125 (2013).

PW 21 Yang, W., Chen, J., Zhu, G., Yang, J., Bai, P., Su, Y., ***Jing, Q.***, Cao, X. & Wang, Z. L. Harvesting energy from the natural vibration of human walking. *ACS nano* **7**, 11317-11324 (2013).

PW 22 Yang, Y., Zhang, H., Chen, J., ***Jing, Q.***, Zhou, Y. S., Wen, X. & Wang, Z. L. Single-electrode-based sliding triboelectric nanogenerator for self-powered displacement vector sensor system. *ACS nano* **7**, 7342-7351 (2013).

PW 23 Yang, Y., Zhang, H., Lin, Z.-H., Zhou, Y. S., ***Jing, Q.***, Su, Y., Yang, J., Chen, J., Hu, C. & Wang, Z. L. Human skin based triboelectric nanogenerators for harvesting

biomechanical energy and as self-powered active tactile sensor system. *ACS nano* **7**, 9213-9222 (2013).

PW 24 Zhou, Y. S., Liu, Y., Zhu, G., Lin, Z.-H., Pan, C., ***Jing, Q.*** & Wang, Z. L. In situ quantitative study of nanoscale triboelectrification and patterning. *Nano letters* **13**, 2771-2776 (2013).

PW 25 Zhu, G., Chen, J., Liu, Y., Bai, P., Zhou, Y. S., ***Jing, Q.***, Pan, C. & Wang, Z. L. Linear-grating triboelectric generator based on sliding electrification. *Nano letters* **13**, 2282-2289 (2013).

PW 26 Su, Y., Zhu, G., Yang, W., Yang, J., Chen, J., ***Jing, Q.***, Wu, Z., Jiang, Y. & Wang, Z. L. Triboelectric Sensor for Self-Powered Tracking of Object Motion inside Tubing. *ACS nano* **8**, 3843-3850 (2014).

PW 27 Xie, Y., Wang, S., Niu, S., Lin, L., ***Jing, Q.***, Su, Y., Wu, Z. & Wang, Z. L. Multi-layered disk triboelectric nanogenerator for harvesting hydropower. *Nano Energy* **6**, 129-136 (2014).

PW 28 Xie, Y., Wang, S., Niu, S., Lin, L., ***Jing, Q.***, Yang, J., Wu, Z. & Wang, Z. L. Grating-Structured Freestanding Triboelectric-Layer Nanogenerator for Harvesting Mechanical Energy at 85% Total Conversion Efficiency. *Advanced Materials* **26**, 6599-6607 (2014).

PW 29 Yang, W., Chen, J., Wen, X., ***Jing, Q.***, Yang, J., Su, Y., Zhu, G., Wu, W. & Wang, Z. L. Triboelectrification Based Motion Sensor for Human-Machine Interfacing. *ACS applied materials & interfaces* **6**, 7479-7484 (2014).

PW 30 Zhou, Y. S., Zhu, G., Niu, S., Liu, Y., Bai, P., ***Jing, Q.*** & Wang, Z. L. Nanometer Resolution Self-Powered Static and Dynamic Motion Sensor Based on Micro-Grated Triboelectrification. *Advanced Materials* **26**, 1719-1724 (2014).

PW 31 Zhu, G., Chen, J., Zhang, T., ***Jing, Q.*** & Wang, Z. L. Radial-arrayed rotary electrification for high performance triboelectric generator. *Nature communications* **5** (2014).

PW 32 Zhu, G., Peng, B., Chen, J., ***Jing, Q.*** & Wang, Z. L. Triboelectric nanogenerators as a new energy technology: From fundamentals, devices, to applications. *Nano Energy* (2014).

PW 33 Zhu, G., Su, Y., Bai, P., Chen, J., ***Jing, Q.***, Yang, W. & Wang, Z. L. Harvesting Water Wave Energy by Asymmetric Screening of Electrostatic Charges on a Nanostructured Hydrophobic Thin-Film Surface. *ACS nano* **8**, 6031-6037 (2014).

PW 34 Zhu, G., Yang, W. Q., Zhang, T., ***Jing, Q.***, Chen, J., Zhou, Y. S., Bai, P. & Wang, Z. L. Self-Powered, Ultrasensitive, Flexible Tactile Sensors Based on Contact Electrification. *Nano letters* **14**, 3208-3213 (2014).

PW 35 Zhu, G., Zhou, Y. S., Bai, P., Meng, X. S., ***Jing, Q.***, Chen, J. & Wang, Z. L. A Shape-Adaptive Thin-Film-Based Approach for 50% High-Efficiency Energy

Generation Through Micro-Grating Sliding Electrification. *Advanced Materials* **26**, 3788-3796 (2014).

PW 36 Chen, J., Yang, J., Li, Z., Fan, X., Zi, Y., ***Jing, Q.***, Guo, H., Wen, Z., Pradel, K. C. & Niu, S. Networks of Triboelectric Nanogenerators for Harvesting Water Wave Energy: A Potential Approach toward Blue Energy. *ACS nano* (2015).

PW 37 Chen, J., Zhu, G., Yang, J., ***Jing, Q.***, Bai, P., Yang, W., Qi, X., Su, Y. & Wang, Z. L. Personalized Keystroke Dynamics for Self-Powered Human-Machine Interfacing. *ACS nano* (2015).

PW 38 Yang, J., Chen, J., Su, Y., ***Jing, Q.***, Li, Z., Yi, F., Wen, X., Wang, Z. & Wang, Z. L. Eardrum-Inspired Active Sensors for Self-Powered Cardiovascular System Characterization and Throat-Attached Anti-Interference Voice Recognition. *Advanced Materials* (2015).

PW 39 Wang, Z. L., Zhu, G., Yang, Y., Zhang, H., Hu, Y., Yang, J., ***Jing, Q.*** & Bai, P. (Google Patents, 2014).